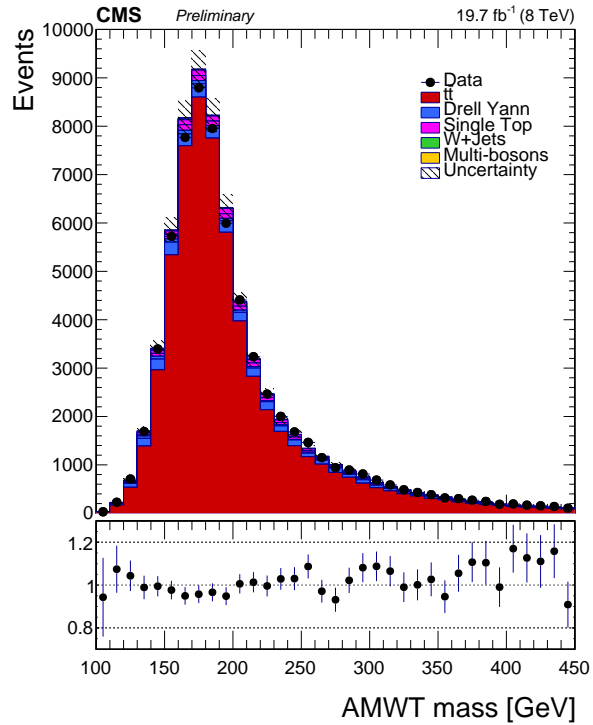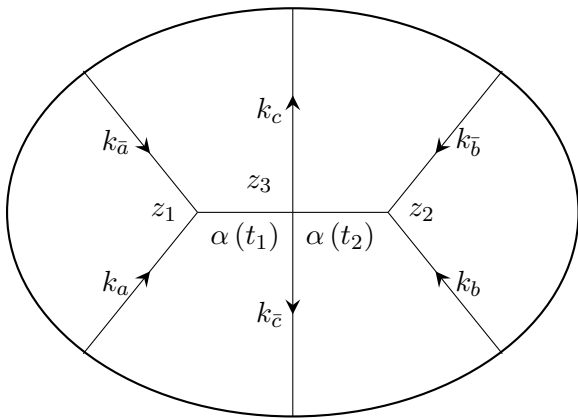# Theoretical and Experimental Studies of High-Energy Processes in QCD

Author:
Richard NALLY

Advisors:
Prof. Chung-I TAN
Prof. Meenakshi NARAIN

April 2015

Contents

Overview

At Brown I have had the pleasure of working for and learning from two outstanding advisors: Profs. Meenakshi Narain and Chung-I Tan. When I arrived at Brown, I knew I wanted to study physics, but had not really thought about what aspect I wanted to specialize in; I had some vague ideas about maybe pursuing string theory, but on the advice of my high school physics teacher went into Brown with an open mind. After I took a course with Prof. Narain the first semester of my freshman year, she generously offered me a chance to work on the LHC, and I took it. After some work studying various b-tagging algorithms and their efficiencies, I began work on the top mass measurement that appears as the first half of this document.

In the three years I've worked on this top mass measurement, I have learned an incredible amount about particle physics and its practice. In the preparation of my publication, I came to understand the design and operation of detectors, Monte Carlo methods, and other important topics in the experimental background. Along the way, I also became interested in some of the theoretical concerns involved in the operation of the LHC, and in particular QCD. This, combined with my previous interest in string theory, led me to pursue an additional research project under Prof. Tan, whose research has recently focused on the application of AdS/CFT to experimentally relevant physics.

Under Prof. Tan, I calculated the inclusive single-particle production cross section in QCD using AdS/CFT methods; the calculation forms the second half of this document. This is an empirically important quantity, and, much to my delight, we found that the AdS/CFT prediction for this cross section agrees with experiment. To me, this represents a beautiful application of some of the most abstract topics in modern physics, such as supergravity and conformal field theories, to experiment, and strikes me as the perfect culmination of my research experience at Brown.

Part I

Measurement of the Top Quark Mass in Fully Leptonic Decays at $\sqrt{s} = 8$ TeV with the Full 2012 CMS Dataset
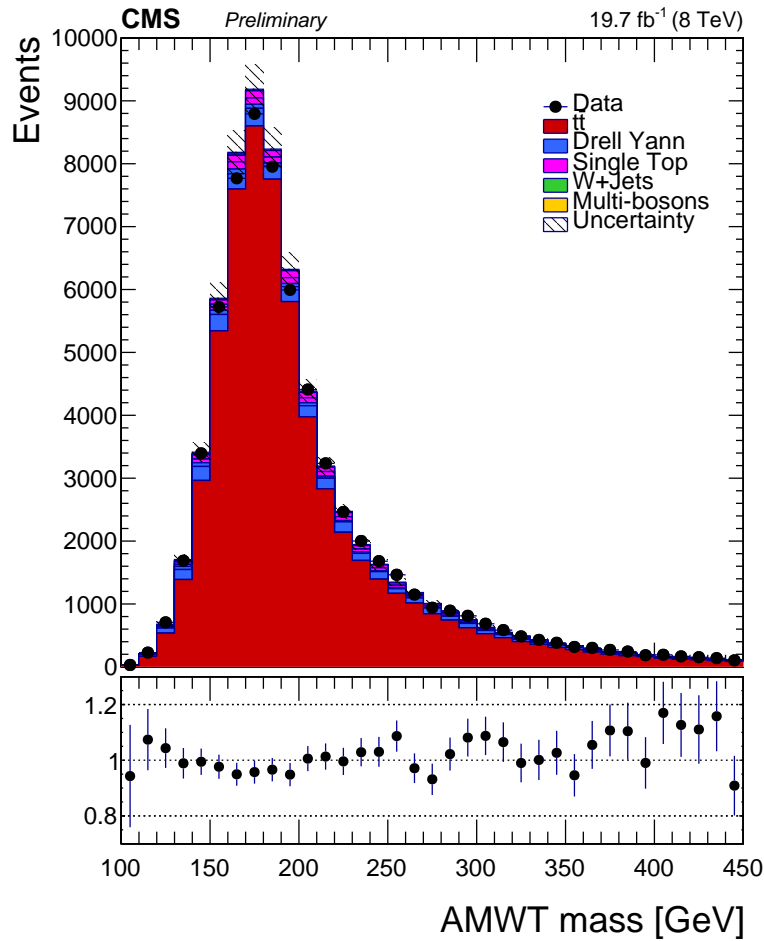
Author:
Richard NALLY

Advisors:
Prof. Meenakshi NARAIN
Prof. Ulrich HEINTZ
Dr. Thomas SPEER

Abstract

We present a measurement of the top quark mass with the full 2012 dataset captured by CMS at a center-of-mass energy of $\sqrt{s} = 8$ TeV, corresponding to an integrated luminosity of 19.7 ± 0.5 fb^{-1}. Our analysis is performed on fully leptonic $t\bar{t}$ decays, where both W bosons decay to $\ell\nu$, and uses the Analytical Matrix Weighting Technique (AMWT). We examine only events with electron and muon states, i.e. events with final lepton states $ee, e\mu$, and $\mu\mu$. The mass of the top quark is measured to be $m_t = 172.82 \pm 0.20$ (stat.) ± 1.22 (syst.) GeV.

I.1 Introduction

The top quark mass is one of the 19 empirical parameters of the Standard Model (SM), and as such its precise measurement is of profound importance. It is one of the major inputs to global electroweak fits, and is linked by radiative corrections to observables such as the Higgs mass. The latest world combination of the top mass, with input from ATLAS, CMS, D0, and CDF, is $m_t = 173.34 \pm 0.27$ (stat) ± 0.71 (syst) GeV/c^2 [1]. In this note we present a measurement of the top quark mass using the full $\sqrt{s} = 8$ TeV 2012 CMS dataset, corresponding to an integrated luminosity of 19.7 ± 0.5 fb^{-1}.

We search for events with $t\bar{t}$ pair production and fully leptonic $t\bar{t}$ decay, in which both the top and antitop decay by the CKM-favored $t \to Wb$ channel and then both W^- and W^+ decay to a lepton-neutrino pair. From this $t\bar{t} \to WbWb \to b\ell\nu b\ell\nu$ decay path we obtain a final state with two charged lepton-neutrino pairs and two b-jets.

The presence of two neutrinos in the dilepton final state prohibits the direct kinematic reconstruction of the parent particle invariant mass, as the kinematic constraints on the neutrino momenta do not uniquely specify them. Instead, we indirectly reconstruct a top mass estimator on an event-by-event basis. For each event, we loop over a large number of top mass hypotheses, and assign to each hypothesis a weight found by solving analytically for all compatible neutrino momenta configurations; this weight can be thought of as quantifying the likelihood of the top mass hypothesis to correspond to the observed event kinematics. We call the top mass hypothesis with the highest weight the reconstructed mass, and measure the physical top mass by comparing distributions of reconstructed masses in data to simulated data generated at a variety of top mass points. A similar measurement, performed in 2011, found $m_t = 172.69 \pm 0.40$ (stat) ± 1.54 (syst) GeV/c^2 [2,3].

In the following, we describe our samples of collider and simulated data, event selection cuts, background estimates, event reconstruction, mass fit, and results.

I.2 Datasets and MC Samples

Here we present the data and Monte Carlo (MC) samples used throughout the analysis. All samples have been processed using the official "B2G" V3 PAT-tuples produced using CMSSW 5.3.8 patch3, and have been analyzed with CMSSW 5.3.16.

The data used in this analysis were collected by the CMS detector in 2012, and comes from p-p collisions at center of mass energy $\sqrt{s} = 8$ TeV. We use the DOUBLEMUON, DOUBLEELECTRON, and MUEG datasets, each of which is associated with specific HLT paths. The latest reconstruction is used (22JANRERECO) with the associated "golden" JSON file [4]; all datasets are filtered to ensure that we only analyze good data.

The list of MC samples used for the analysis is shown in Tables 1, 2, and 3. For all the Monte Carlo samples, a full CMS detector simulation based on GEANT4 is performed with realistic detector conditions. To obtain a PU profile which corresponds to the data analyzed, the reweighing procedure detailed in Ref. [5,6] is used, accounting further for the pixel luminosity corrections and using as total inelastic cross section 69.4 nb.

Table 1: Summary of Monte Carlo datasets used. All MC samples processed in the `Summer12_DR53X` campaign with the PU S10 pile-up scenario (`Summer12_DR53X-PU_S10_START53_V19-v1`).

Dataset Description	Primary Dataset Name	x-section (pb)
t$\bar{\text{t}}$	/TTJets_MSDecays_central_TuneZ2star_8TeV-madgraph-tauola	245.8
$\bar{\text{t}}$W	/Tbar_tW-channel-DR_TuneZ2star_8TeV-powheg-tauola/	11.1
tW	/T_tW-channel-DR_TuneZ2star_8TeV-powheg-tauola/	11.1
W Jets	/WJetsToLNu_TuneZ2Star_8TeV-madgraph/	36703.2
ZZ	/WW_TuneZ2star_8TeV_pythia6_tauola	17
WZ	/WZ_TuneZ2star_8TeV_pythia6_tauola	33.6
WW	/ZZ_TuneZ2star_8TeV_pythia6_tauola	56
Z/γ^*[10-50] $\rightarrow$ ll	/DYJetsToLL_M-10To50filter_8TeV-madgraph	860.5
Z/γ^*[50-inf] $\rightarrow$ ll	/DYJetsToLL_M-50_TuneZ2Star_8TeV-madgraph-tarball	3532.8

The simulation of t$\bar{\text{t}}$ events is performed using the MADGRAPH 5.1.4.8 matrix element generator [7] and MADSPIN [8] for the decay of heavy resonances. The generated partons are processed with PYTHIA 6.426 [9] to provide showering of the generated particles using the $Z2*$ tune [10]. The showers are matched using the k_T-MLM prescription [11]. For the default sample, a top quark mass of $m_t = 172.5\,\text{GeV}/c^2$ is assumed. Six additional samples with masses between $166.5\,\text{GeV}/c^2$ and $178.5\,\text{GeV}/c^2$ are used (c.f. Table 2).

Table 2: t$\bar{\text{t}}$ Monte Carlo samples with different masses of the top quark. All MC samples processed in the `Summer12_DR53X` campaign with the PU S10 pile-up scenario(`Summer12_DR53X-PU_S10_START53_V19-v1`).

Top mass m_t	Primary Dataset Name
166.5	/TTJets_MSDecays_mass166_5_TuneZ2star_8TeV-madgraph-tauola
169.5	/TTJets_MSDecays_mass169_5_TuneZ2star_8TeV-madgraph-tauola
171.5	/TTJets_MSDecays_mass171_5_TuneZ2star_8TeV-madgraph-tauola
173.5	/TTJets_MSDecays_mass173_5_TuneZ2star_8TeV-madgraph-tauola
175.5	/TTJets_MSDecays_mass175_5_TuneZ2star_8TeV-madgraph-tauola
178.5	/TTJets_MSDecays_mass178_5_TuneZ2star_8TeV-madgraph-tauola

The main background processes for this analysis are Drell Yan, single top quarks, W/Z + jets, WW, WZ, and ZZ. Electroweak production of single top quarks is simulated using POWHEG version 1 [12–14]; MADGRAPH is used to simulate W/Z events with up to four jets. Production of WW, WZ, and ZZ is simulated with PYTHIA.

The top quark pair production cross section computed at NNLO, $\sigma_{t\bar{t}} = 245.8 \pm 9.7$ pb, is used [15]. The cross section for associated single top quark production (tW) is taken to be $\sigma_{\text{tW}} = 22.2 \pm 1.5$ pb at NNLO [16]. The inclusive NNLO cross section for the production of W bosons multiplied by their branching fraction to leptons has been determined to be $\sigma_{\text{W}\rightarrow l\nu} = 36.7 \pm 1.3$ nb using FEWZ version 3.1 [17]. Finally, the Drell-Yan (DY) production cross section at NNLO has

6

been calculated using FEWZ as $\sigma_{Z/\gamma^* \to ll}(m_{ll} > 50\,\text{GeV}) = 3530 \pm 120$ pb, where m_{ll} is the invariant mass of the two leptons and the scales were set using the Zboson mass $m_Z = 91.1876\,\text{GeV}$ [18].

Table 3: Additional $t\bar{t}$ Monte Carlo samples used to estimate the systematic uncertainty.

Primary Dataset Name
/TTJets_MSDecays_matchingup_TuneZ2star_8TeV-madgraph-tauola/Summer12_DR53X-PU_S10_START53_V19-v2/AODSIM
/TTJets_MSDecays_matchingdown_TuneZ2star_8TeV-madgraph-tauola/Summer12_DR53X-PU_S10_START53_V19-v1/AODSIM
/TTJets_MSDecays_matchingdown_TuneZ2star_8TeV-madgraph-tauola/Summer12_DR53X-PU_S10_START53_V19-v2/AODSIM
/TTJets_MSDecays_scaleup_TuneZ2star_8TeV-madgraph-tauola/Summer12_DR53X-PU_S10_START53_V19-v1/AODSIM
/TTJets_MSDecays_scaledown_TuneZ2star_8TeV-madgraph-tauola/Summer12_DR53X-PU_S10_START53_V19-v1/AODSIM
/TT_CT10_AUET2_8TeV-powheg-herwig/Summer12_DR53X-PU_S10_START53_V19-v1/AODSIM
/TT_CT10_TuneZ2star_8TeV-powheg-tauola/Summer12_DR53X-PU_S10_START53_V7A-v2/AODSIM
/TTJets_HadronicMGDecays_TuneP11_8TeV-madgraph-tauola/Summer12_DR53X-PU_S10_START53_V19-v1/AODSIM
/TTJets_SemiLeptMGDecays_TuneP11_8TeV-madgraph-tauola/Summer12_DR53X-PU_S10_START53_V19-v1/AODSIM
/TTJets_FullLeptMGDecays_TuneP11_8TeV-madgraph-tauola/Summer12_DR53X-PU_S10_START53_V19-v1/AODSIM
/TTJets_HadronicMGDecays_TuneP11mpiHi_8TeV-madgraph-tauola/Summer12_DR53X-PU_S10_START53_V19-v1/AODSIM
/TTJets_SemiLeptMGDecays_TuneP11mpiHi_8TeV-madgraph-tauola/Summer12_DR53X-PU_S10_START53_V19-v1/AODSIM
/TTJets_FullLeptMGDecays_TuneP11mpiHi_8TeV-madgraph-tauola/Summer12_DR53X-PU_S10_START53_V19-v1/AODSIM
/TTJets_HadronicMGDecays_TuneP11TeV_8TeV-madgraph-tauola/Summer12_DR53X-PU_S10_START53_V19-v1/AODSIM
/TTJets_SemiLeptMGDecays_TuneP11TeV_8TeV-madgraph-tauola/Summer12_DR53X-PU_S10_START53_V19-v1/AODSIM
/TTJets_FullLeptMGDecays_TuneP11TeV_8TeV-madgraph-tauola/Summer12_DR53X-PU_S10_START53_V19-v1/AODSIM
/TTJets_HadronicMGDecays_TuneP11noCR_8TeV-madgraph-tauola/Summer12_DR53X-PU_S10_START53_V19-v1/AODSIM
/TTJets_SemiLeptMGDecays_TuneP11noCR_8TeV-madgraph-tauola/Summer12_DR53X-PU_S10_START53_V19-v1/AODSIM
/TTJets_FullLeptMGDecays_TuneP11noCR_8TeV-madgraph-tauola/Summer12_DR53X-PU_S10_START53_V19-v1/AODSIM

I.3 Event Selection

In events of interest to this analysis, both the W^- and W^+ bosons produced in the decay of the t and $\bar{t}$ quarks, respectively, will decay to leptons. We are thus interested in signal events with two opppositely charged high p_T leptons, two b-jets, and large missing transverse momentum. These give our major selection cuts for both data and MC events: we require two isolated, well constructed, opposite-charge leptons along with two energetic jets and missing transverse energy. We reconstruct physics objets using the Particle-Flow (PF) algorithm [19].

I.3.1 Event Cleaning

The following procedures were employed to "clean" the event:

- No scraping: the event is rejected if the fraction of high purity tracks is $< 25\%$ in events with at least 10 tracks.

- Require at least one good primary vertex (PV); the PV must have more than 4 degrees of freedom and must be less than 24 cm away from the nominal interaction point in z and less than 2 cm away radially.

- HBHE event-level noise filtering.

- CSC Beam Halo Filter.

- HCAL Laser Jets filter.

- ECAL dead cell filter.

- Tracking failure filter.

- Bad EE Super cluster filter.

- HCAL laser event filter

I.3.2 Trigger Selection

Since we choose the two leptons with the highest transverse momentum satisfying all selection criteria (described below), the events are characterized by the flavor of the these leptons, and we can classify our events as ee, $e\mu$, or $\mu\mu$. For each dilepton configuration, only events collected by the relevant primary dataset and the relevant HLT trigger are considered for the analysis. This facilitates the construction mutually exclusive channels and helps confirm that the dilepton candidates have fired the trigger. The triggers used are listed in Table 4. The efficiencies of the listed triggers were measured in [20]; from these measured efficiencies, channel-dependent scale factors (SFs), calculated by comparing efficiencies for CMS and simulated data, were found to be 0.958 ± 0.010 in the $\mu\mu$ channel, 0.996 ± 0.011 in the ee channel, and 0.953 ± 0.010 in the $e\mu$ channel.

$e\mu$	HLT_Mu17_Ele8_CCTT_v4, 5, 6, 7, 8, 9 or HLT_Mu8_Ele17_CCTT_v4, 5, 6, 7, 8, 9
$\mu\mu$	HLT_Mu17_Mu8_v16, 17, 18, 19, 21, 22 or HLT_Mu17_TkMu8_v9, 10, 11, 12, 13, 14
ee	HLT_Ele17_CCTT_Ele8_CCTT_v15, 16, 17, 18, 19

Table 4: List of triggers used in the analysis. CCTT stands for CaloIdT_CaloIsoVL_TrkIdVL_TrkIsoVL.

I.3.3 Lepton Reconstruction and Selection

We require two well identified and isolated leptons. Separate algorithms are used to reconstruct muons and electrons, and are discussed below. Lepton isolation cuts are given in terms of the Relative Lepton Isolation (RLI). Data-to-MC scale factors are applied to reproduce data selection efficiency in the MC events.

We demand that all events have dilepton pair mass $m_{\ell\ell} > 20 \text{ GeV}/c^2$ to reduce contamination from Drell-Yan events and heavy flavor resonances. Additionally, in the ee and $\mu\mu$ channels, we remove events with $76 \text{ GeV}/c^2 < m_{\ell\ell} < 106 \text{ GeV}/c^2$ to limit the influence of events from Z decays.

I.3.3.1 Muon Reconstruction and Selection

The muon reconstruction algorithm, described in [21], reconstructs global muons by linking tracks from the track system with those reconstructed from hits in the muon chambers; final reconstruction comes from combining these categories of tracks. We use the PF muon selection cuts from [22], which corresponds to baseline selection for loose ID muons with loose isolation requirement:

- is either a GlobalMuon or aTrackerMuon

- $p_T > 20$ GeV/c

- $|\eta| < 2.4$,

- $RLI < 0.20$, evaluated in a cone of $R = 0.4$ around the lepton's vector momentum, and using the DeltaBeta correction.

We apply η- and p_T-dependent scale factors to correct selection efficiency in simulation to data levels [23].

I.3.3.2 Electron Reconstruction and Selection

The electron reconstruction algorithm, described in [24], searches for tracker hits compatible with readings from the ECAL superclusters; the effect of bremsstrahlung in the tracker is accounted for in the reconstruction of electron tracks. We use the PF electron selection cuts from [22]:

- $p_T > 20$ GeV/c

- $|\eta| < 2.5$,

- $RLI < 0.15$, evaluated in a cone of $R = 0.3$ around the lepton's vector momentum, using the rho-correction [25]

- transverse impact parameter of the electron gsfTrack with respect to the beam spot < 0.04 cm,

- $\Delta R > 0.1$ ($R = \sqrt{\Delta\eta^2 + \Delta\varphi^2}$) between the electron candidate and any global or tracker muon in the event whose number of hits in the inner tracker is greater than 10;

- Photon conversion rejection

- MVA > 0.5

We apply η- and p_T-dependent scale factors to correct selection efficiency in simulation to data levels [26].

I.3.4 Jet Selection and Missing Transverse Momentum

We reconstruct jets from PF candidates with the anti-k_T algorithm (using $\Delta R = 0.5$). As above, we use the selection cuts from [22], applying the L1FastJet, L2, and L3 corrections to all events; data events also have the L2L3Residual correction. A charged hadron subtraction technique identifies and removes jet constituents originating from charged hadrons associated with pileup vertices. We use a Loose Jet Identification, where the fraction of charged hadronic energy is required to be ≥ 0, the fraction of charged electromagnetic energy ≤ 0.99, the fraction of neutral hadronic energy < 0.99, and the fraction of neutral electromagnetic fraction < 0.99. Kinematical cuts require $p_T > 30$ GeV and $|\eta| < 2.5$ for all jets, both b-tagged and not.

We use the latest Winter14 jet energy corrections [27]. In Monte Carlo, the jet energy is smeared according to the procedure outlined in [28].

The missing transverse momentum ($\not{E}_T$) is directly reconstructed as the vector sum of all PF candidates, projected onto the transverse plane. We use a Type 1 jet energy correction in calculating the $\not{E}_T$. For ee and $\mu\mu$ events, we demand $\not{E}_T > 40$ GeV to further reduce DY event yields.

9

I.3.5 Jet Selection Using b-tagging

We demand that all events have at least two jets tagged as b-jets by the Combined Secondary Vertex algorithm, evaluated at the Loose working point (CSVL). In events with more than two b-tags, we select the two leading-p_T b-tagged jets. To reproduce the performance of the b-tagging algorithm measured in the data in the simulation, data to-Monte Carlo scale factor are applied, using the so-called *EPS13 prescription* [29].

I.4 Estimate of the Background Contamination

As described above, our primary backgrounds are Drell-Yan, single top, and W+Jets production. Of these, DY and single top events contain two real leptons, whereas the W+Jets events that pass cuts have fake leptons; because the lepton fake rate is low, we expect relatively few W+Jets events.

Single top, diboson, and W+Jets backgrounds are normalized directly to luminosity times cross section; no scale factors are applied. For the DY background, however, a data-driven normalization is employed; scale-factors are measured from data on a channel-by-channel basis, for a total of six calculated DY scale factors, one each for three b-tag categories times two lepton channels. For ee and $\mu\mu$ events, the $R_{out/in}$ method, laid out in [2, 30, 31] is used. In this method, the ratio $R_{out/in}$ of simulation events inside and outside the Z peak in the dilepton invariant spectrum is used to estimate the number of data events with dilepton invariant mass outside the Z peak. In the $e\mu$ channel, we apply no scale factor. The measured DY scale factors and their statistical uncertainties are shown in Table 5. We consider an uncertainty of $\pm 30\%$ on the overall Drell-Yan normalization as a systematic uncertainty.

Channel	DY SF: ee	DY SF: $\mu\mu$
0B	0.99 ± 0.30	1.05 ± 0.31
1B	1.17 ± 0.35	1.20 ± 0.36
2B	1.07 ± 0.32	1.22 ± 0.37

Table 5: Rout/in DY scale factors by b-tags and lepton content.

I.5 Event Yields and Data-MC Comparisons

The above selection criteria, applied to data and MC, result in event yields shown in Tables 6, **??** and **??**; although events with 0 b-tags are not used in their analysis, the yields of such events are shown for completeness.

In Figures I.5.1 through I.5.8, we plot data/MC comparisons of event characteristic variables after all event cuts. In these figures, it can be seen that the top quark transverse momentum distributions are softer in data than in simulation; this has been seen in other analyses as well. A top quark momentum reweighting procedure has been developed to counteract this; it is treated here as a systematic uncertainty (Appendix A).

Table 6: Number of events with 0 b-tags after all cuts.

Sample	$\mu\mu$	eμ	ee	Sum
TTbar	980.38	2771.51	827.28	4579.17
WJets	9.46	81.91	22.25	113.63
Diboson	153.09	356.86	128.39	638.33
SingleTop	73.75	229.66	75.73	379.14
DrellYan	2830.74	1134.52	2387.21	6352.47
Total MC	4047.42	4574.47	3440.85	12062.75
Data	4479.69	4546.71	3644.09	12670.50
Data/MC	1.11	0.99	1.06	1.05

Table 7: Number of events with 1 b-tag after all cuts

Sample	$\mu\mu$	eμ	ee	Sum
TTbar	5373.80	15519.38	4585.48	25478.67
WJets	14.81	67.41	10.03	92.25
Diboson	84.71	170.87	65.99	321.57
SingleTop	346.17	952.75	274.60	1573.52
DrellYan	1543.96	539.76	1284.67	3368.39
Total MC	7363.46	17250.17	6220.76	30834.38
Data	7280.71	16238.87	6018.20	29537.77
Data/MC	0.99	0.94	0.97	0.96

Table 8: Number of events with ≥ 2 b-tags after all cuts

Sample	$\mu\mu$	eμ	ee	Sum
TTbar	8159.86	23827.72	6905.88	38893.46
WJets	0.00	18.01	21.00	39.01
Diboson	19.52	35.76	15.78	71.06
SingleTop	261.04	749.83	230.78	1241.65
DrellYan	293.53	119.58	249.57	662.69
Total MC	8733.95	24750.91	7423.01	40907.88
Data	8704.78	24658.39	7499.36	40862.53
Data/MC	1.00	1.00	1.01	1.00

Figure I.5.1: Dilepton invariant mass spectra from data and MC events, using the $m_t = 172.5$ GeV MC sample, for *ee* events (top left), *eμ* events (top right), *μμ* events (bottom left), and for all categories combined (bottom right). All selection cuts are used, along with SFs for trigger, lepton selection, and background estimation; the hatched area corresponds to the SF uncertainties as well as the 2.6 % uncertainty on the overall integrated luminosity.

Figure I.5.2: Leading lepton p_T from data and MC events, using the $m_t = 172.5$ GeV MC sample, for *ee* events (top left), *eμ* events (top right), *μμ* events (bottom left), and for all categories combined (bottom right). All selection cuts are used, along with SFs for trigger, lepton selection, and background estimation; the hatched area corresponds to the SF uncertainties as well as the 2.6 % uncertainty on the overall integrated luminosity.

Figure I.5.3: Second-leading lepton p_T from data and MC events, using the $m_t = 172.5$ GeV MC sample, for ee events (top left), $e\mu$ events (top right), $\mu\mu$ events (bottom left), and for all categories combined (bottom right). All selection cuts are used, along with SFs for trigger, lepton selection, and background estimation; the hatched area corresponds to the SF uncertainties as well as the 2.6 % uncertainty on the overall integrated luminosity.
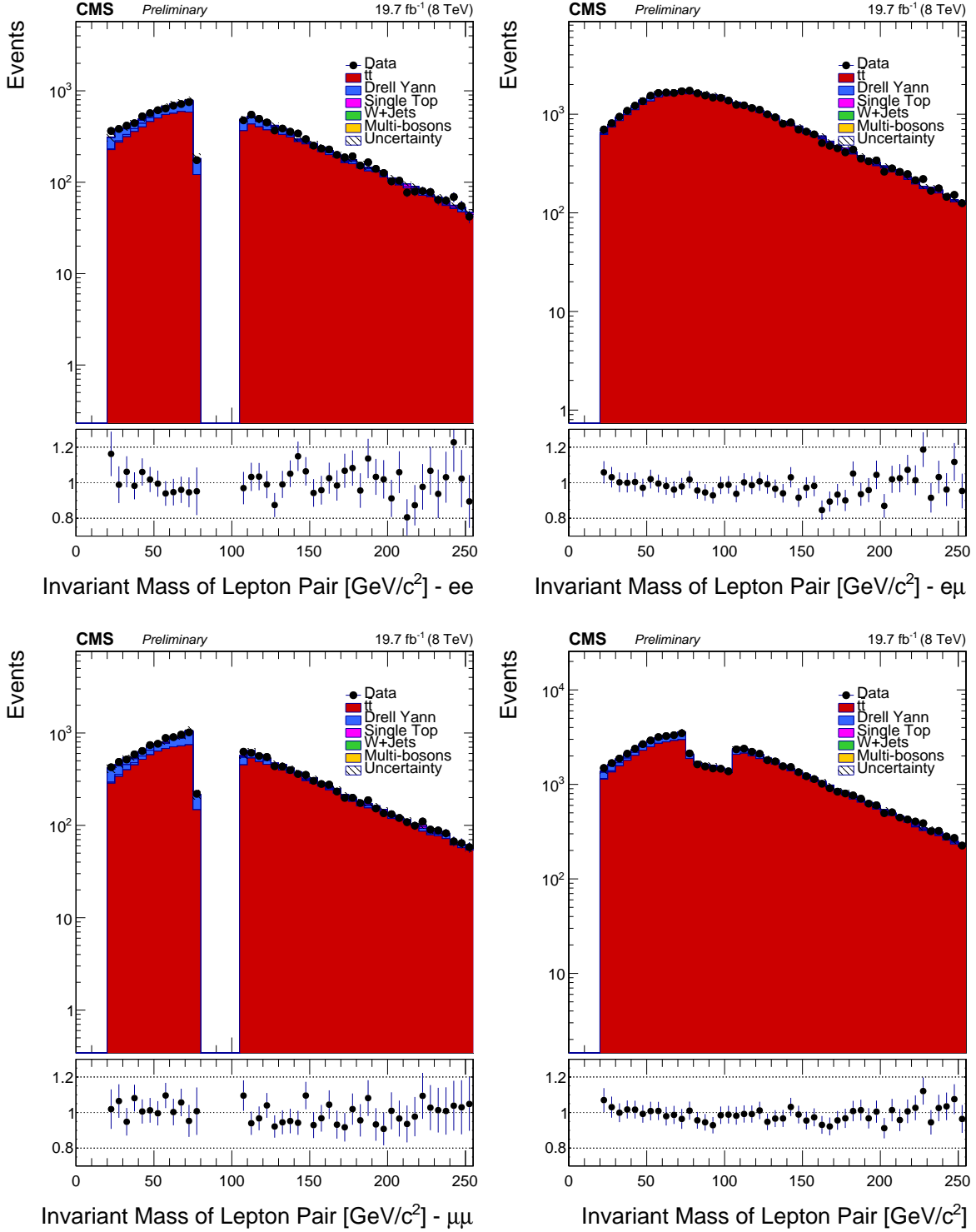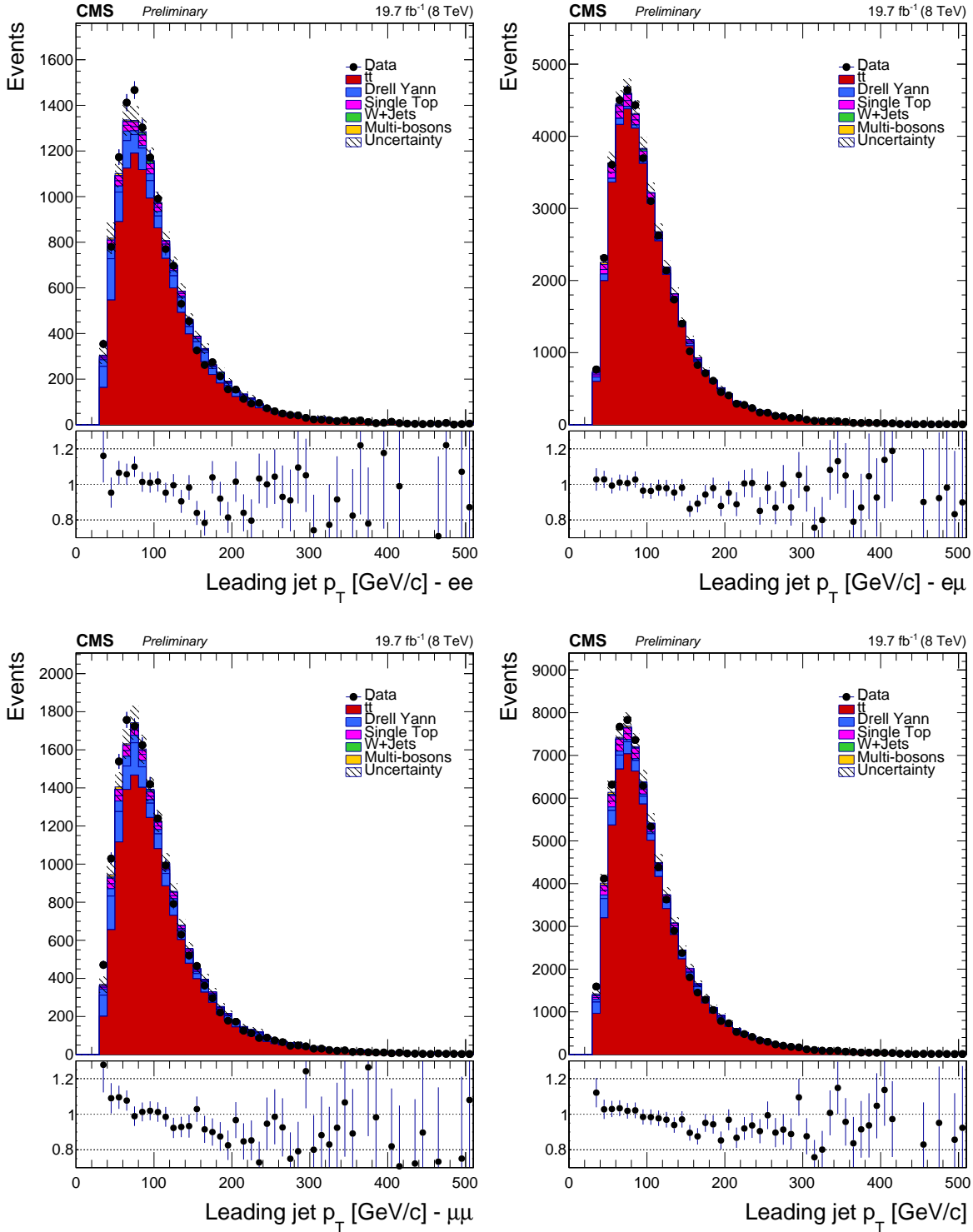
Figure I.5.4: Leading jet p_T from data and MC events, using the $m_t = 172.5$ GeV MC sample, for ee events (top left), $e\mu$ events (top right), $\mu\mu$ events (bottom left), and for all categories combined (bottom right). All selection cuts are used, along with SFs for trigger, lepton selection, and background estimation; the hatched area corresponds to the SF uncertainties as well as the 2.6 % uncertainty on the overall integrated luminosity.
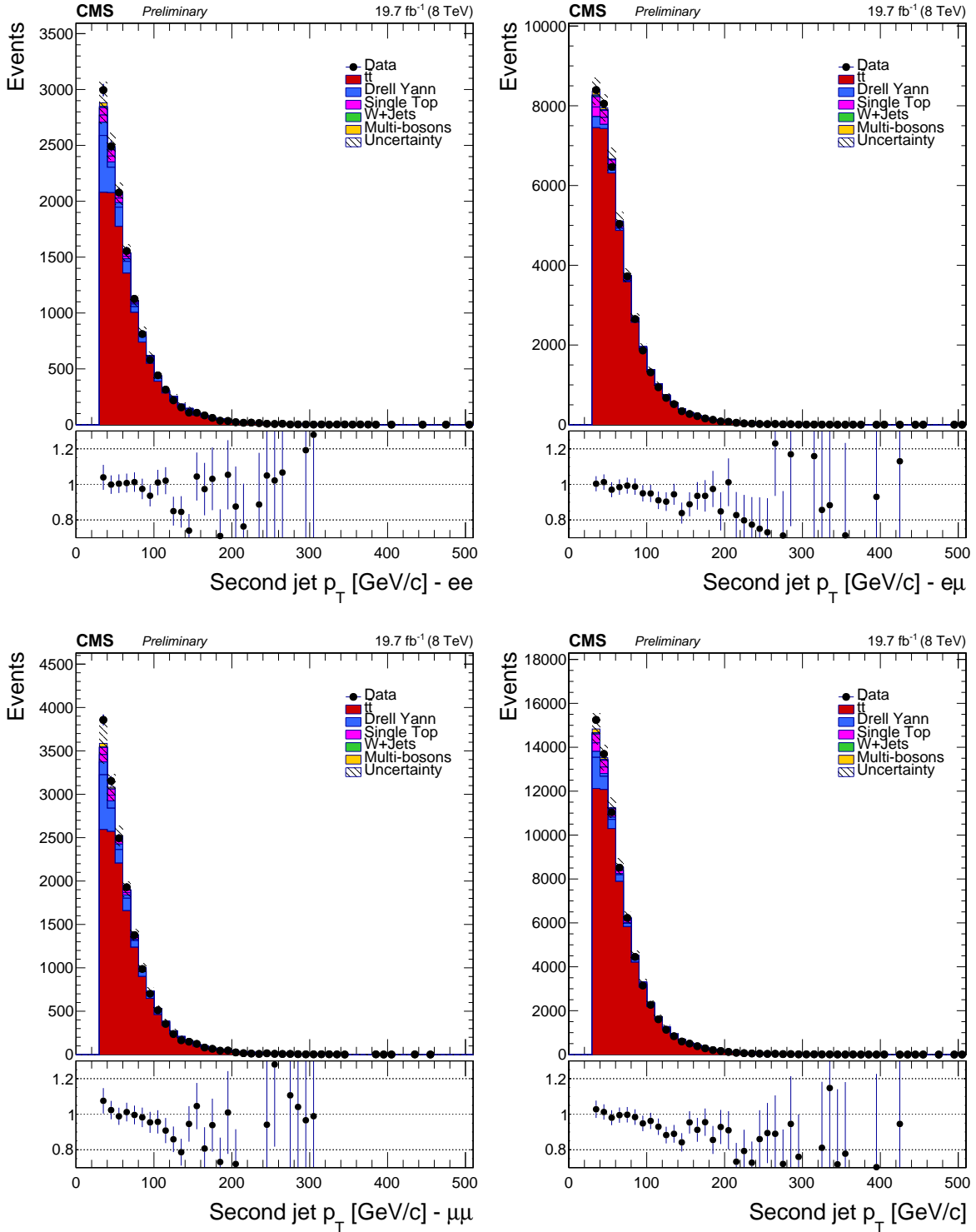
Figure I.5.5: Second-leading jet p_T from data and MC events, using the $m_t = 172.5$ GeV MC sample, for ee events (top left), $e\mu$ events (top right), $\mu\mu$ events (bottom left), and for all categories combined (bottom right). All selection cuts are used, along with SFs for trigger, lepton selection, and background estimation; the hatched area corresponds to the SF uncertainties as well as the 2.6 % uncertainty on the overall integrated luminosity.
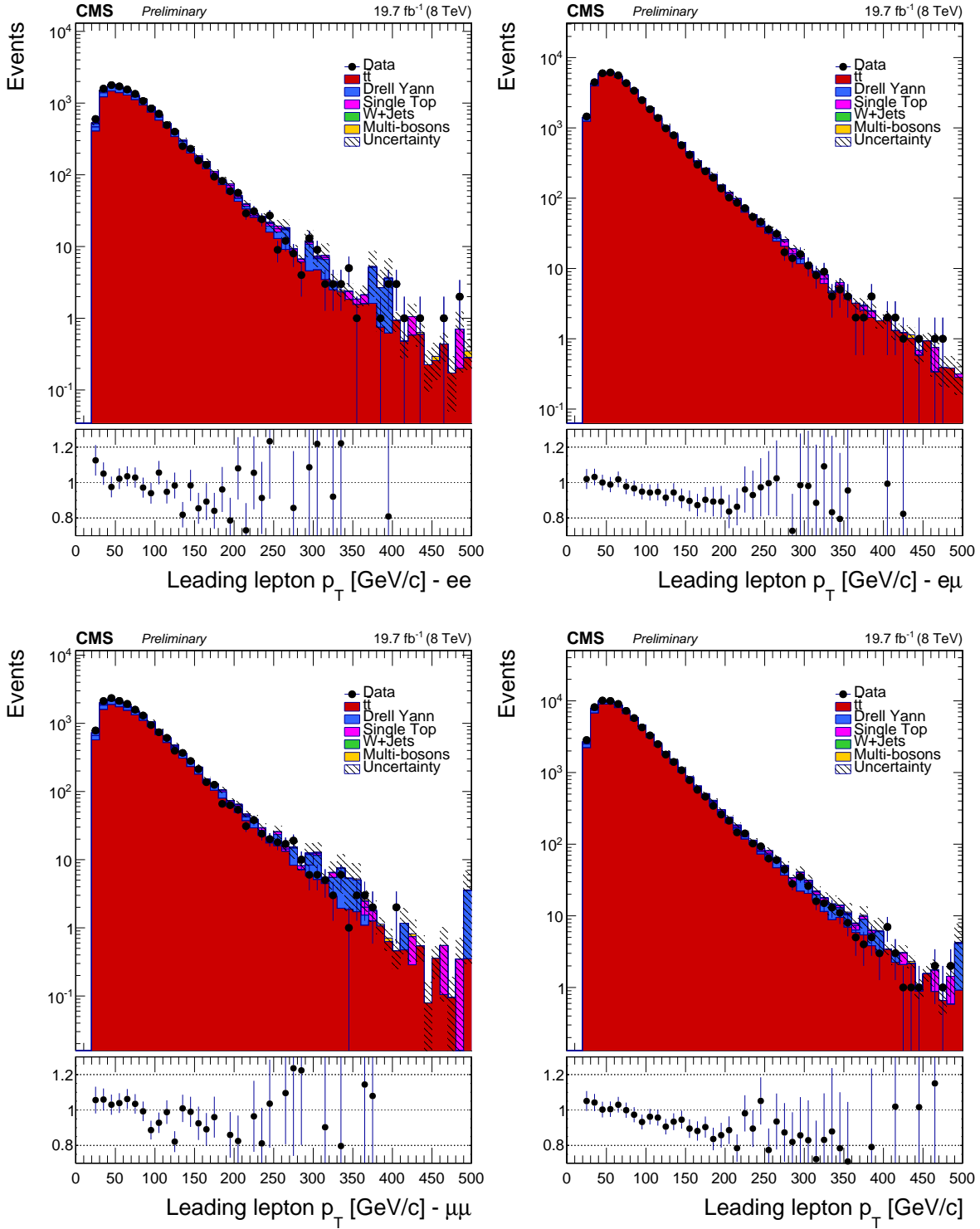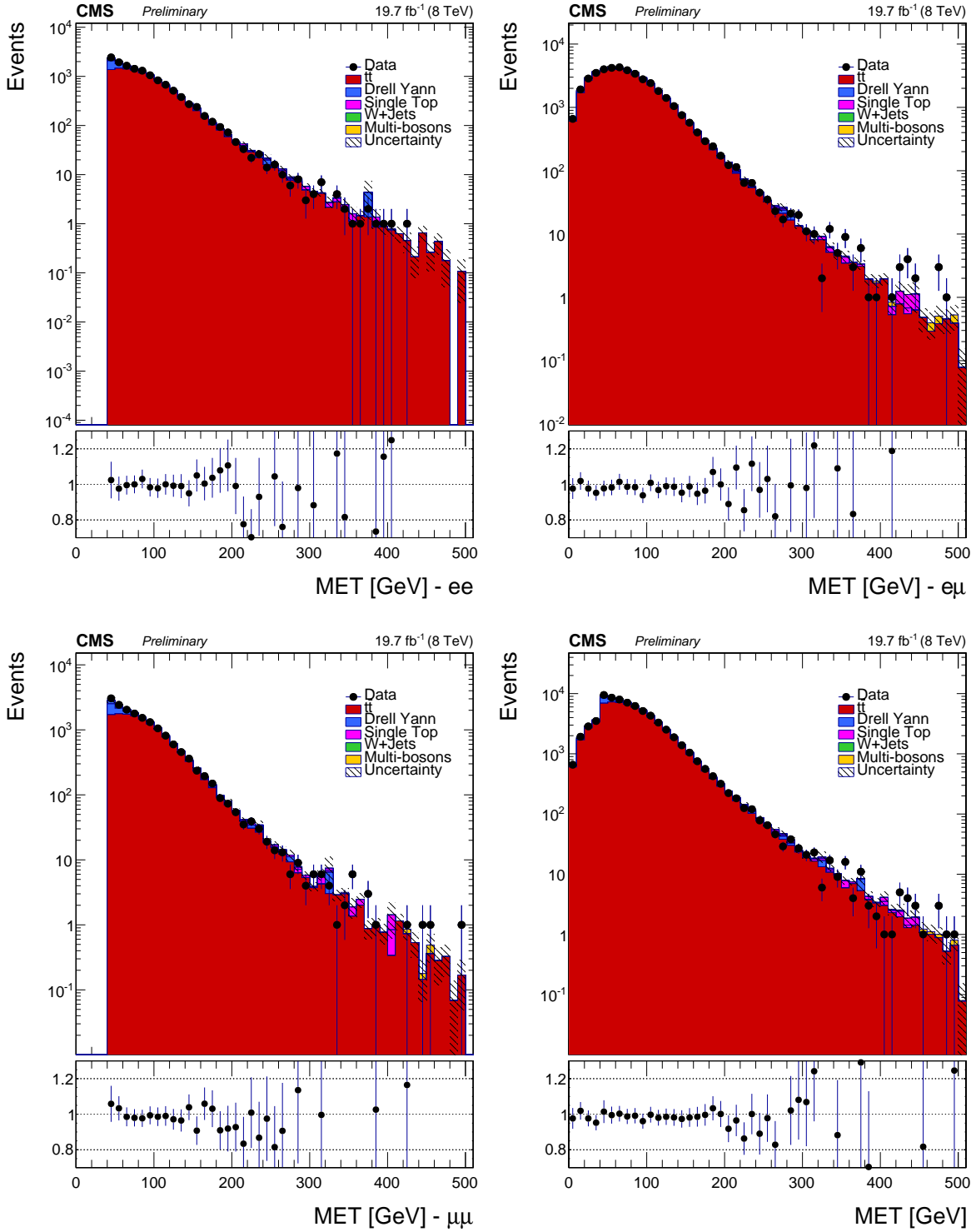
Figure I.5.6: Missing E_T from data and MC events, using the $m_t = 172.5$ GeV MC sample, for *ee* events (top left), *eµ* events (top right), *µµ* events (bottom left), and for all categories combined (bottom right). All selection cuts are used, along with SFs for trigger, lepton selection, and background estimation; the hatched area corresponds to the SF uncertainties as well as the 2.6 % uncertainty on the overall integrated luminosity.
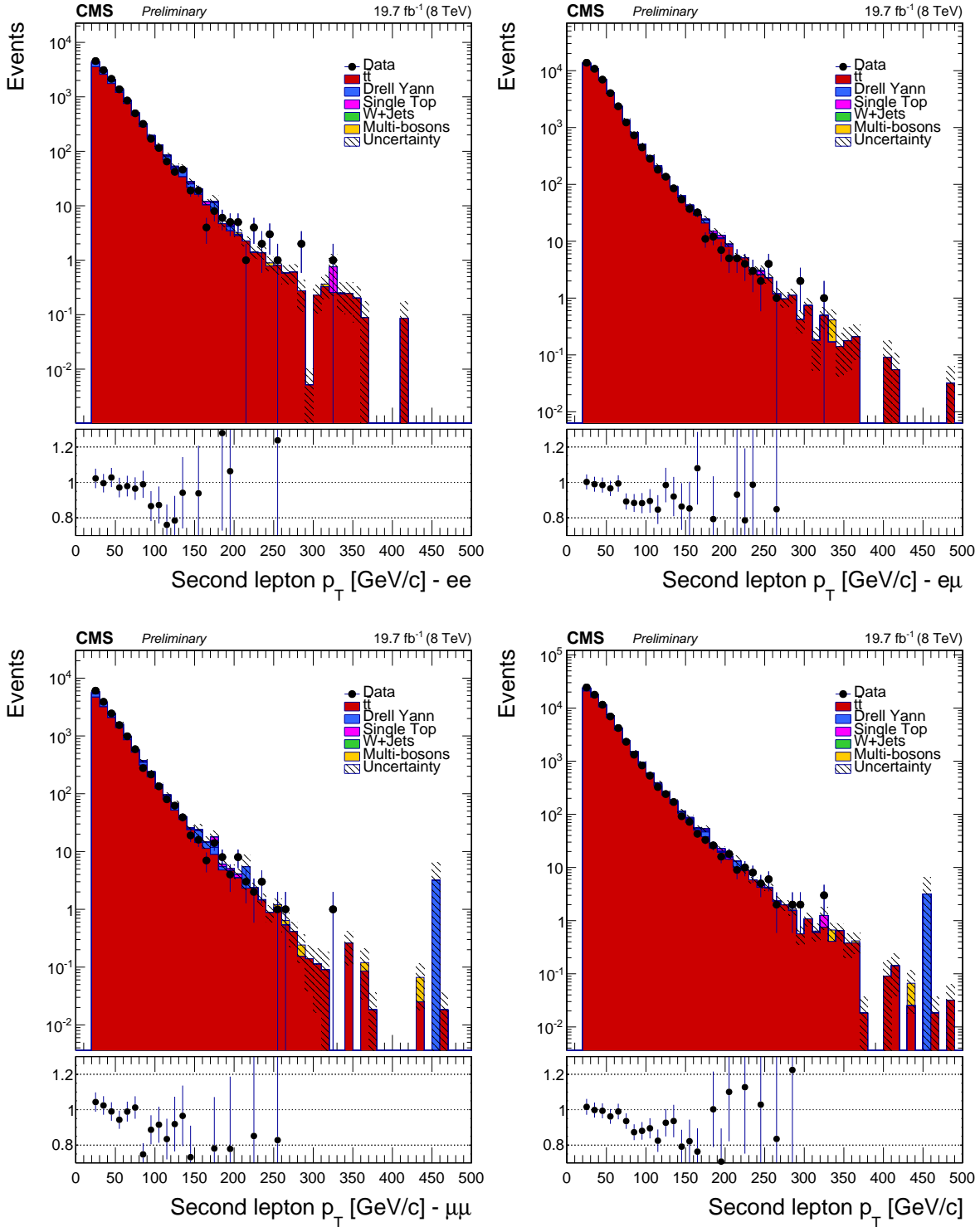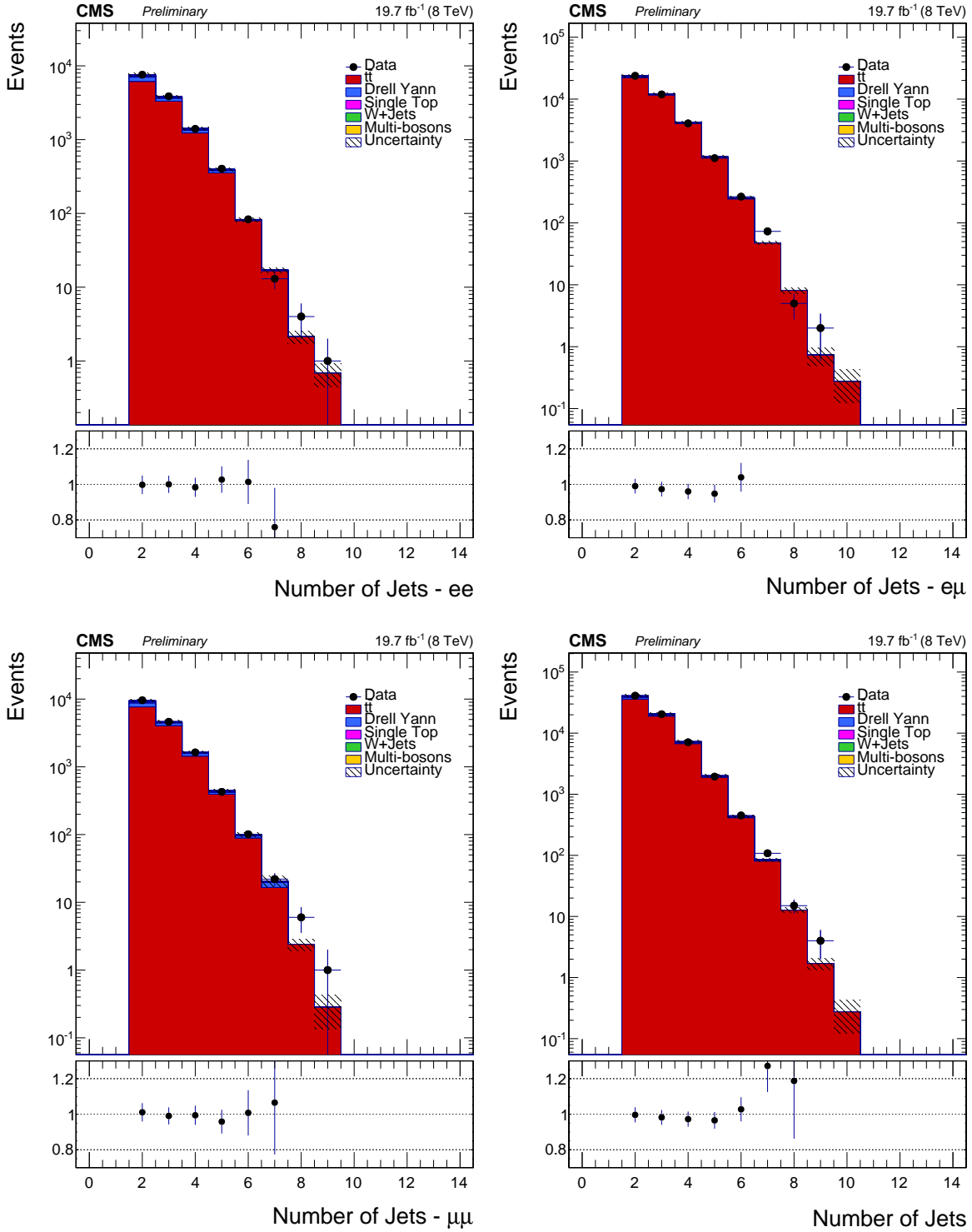
Figure I.5.7: Jet multiplicity from data and MC events, using the $m_t = 172.5$ GeV MC sample, for ee events (top left), $e\mu$ events (top right), $\mu\mu$ events (bottom left), and for all categories combined (bottom right). All selection cuts are used, along with SFs for trigger, lepton selection, and background estimation; the hatched area corresponds to the SF uncertainties as well as the 2.6 % uncertainty on the overall integrated luminosity.

Figure I.5.8: Multiplicity of b-tagged jets from data and MC events, using the $m_t = 172.5$ GeV MC sample, for ee events (top left), $e\mu$ events (top right), $\mu\mu$ events (bottom left), and for all categories combined (bottom right). All selection cuts are used, along with SFs for trigger, lepton selection, and background estimation; the hatched area corresponds to the SF uncertainties as well as the 2.6 % uncertainty on the overall integrated luminosity.
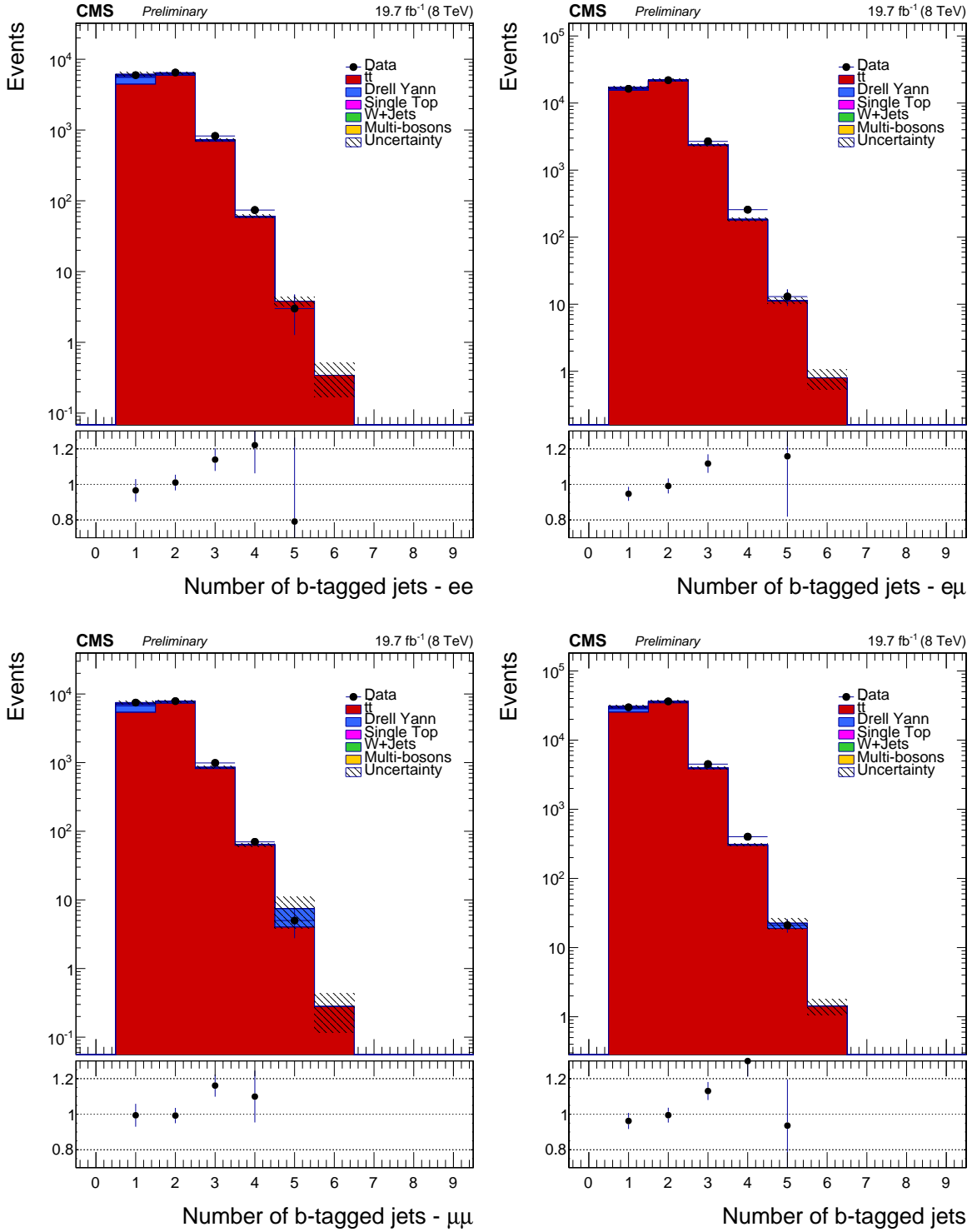
I.6   Event Reconstruction

Our event reconstruction employs what is known as the Analytical Matrix Weighting Technique (AMWT), an improved version of the Matrix Weighting Technique (MWT) first proposed for use by the D0 Collaboration by one of the authors [32]. The AMWT has previously been employed by CMS for use in measurements of the top mass in 2011 and 2010 data [2, 33].

In fully leptonic $t\bar{t}$ decays, the final state products include two charged leptons, two neutrinos, and two jets. This leaves us with 18 total kinematical unknowns: three components of momenta each from the two charged leptons, two jets, and the two neutrinos; these eighteen unknowns completely specifiy the total momentum of the $t\bar{t}$ pair. Of these, we observe the momenta of the two charged leptons and the two jets, and the transverse momentum of all other charged particles and jets; the selection of the jets to be used is facilitated by b-tagging. Hence, after physics object reconstruction, we can assign the momenta of the b and $\bar{b}$ quarks to the decays of the t and $\bar{t}$ quarks, respectively, to find the following observables for each event:

- the momenta $\vec{p}_{\ell+}$ and $\vec{p}_{\ell-}$ of the charged leptons from the W^+ and W^- decays,

- the momenta $\vec{p}_b$ and $\vec{p}_{\bar{b}}$ of the b and $\bar{b}$ produced by the t and $\bar{t}$ quarks,

- the total transverse momentum $p_{T;t\bar{t}}$ of the $t\bar{t}$ pair.

The only decay products we cannot measure are the neutrinos. This leaves us with six unknowns: three each from the momenta of the two neutrinos. Meanwhile, conservation of four-momentum provides the following four constraints on the kinematics, if a top quark mass values is assumed:

- the masses $m_{\ell+\nu}$ and $m_{\ell-\bar{\nu}}$ of the lepton-neutrino pairs from the W^+ and W^- decays must be equal to the mass of the W boson,

- the masses of the systems of particles from the t and $\bar{t}$ decays must equal the mass of the top quark.

There exist several methods to find solutions to these equations. We follow the method of L. Sonnenschein, presented in [34–36]. In [34, 35] it is shown that, if no sources of missing transverse momentum other than the neutrinos are present, no more than eight configurations of neutrino momenta are compatible with a given top mass hypothesis. In particular, the constraints force the transverse momenta of each neutrino to lie on ellipses in the p_x-p_y plane; since we assume all missing transverse momenta comes from the neutrinos, the momentum solutions compatible with the top mass hypothesis are the intersection points of the momentum-space ellipses of the two neutrinos. Any two ellipses can intersect in zero, two, or four places, and there is a twofold ambiguity of assigning momenta to the b and $\bar{b}$ jets, leaving an upper bound total of eight possible neutrino momenta configurations. In rare cases, a latent singularity in the equations used to find these solutions can prohibit the calculation of the longitudinal momenta; in such events, a numerical method is employed to find the uncalculable variables [36].

The implementation of this method of event reconstruction is conceptually straightforward. For each event, we find all solutions of neutrino momenta for mass hypotheses between 100 and 600 GeV, in 1 GeV increments. In general, we expect consistent solutions to be found for a large range of mass hypotheses. To each solution we assign a weight w given by [37]:

$$w = \left[\sum_{\text{initial partons}} F\left(x_1\right) F\left(\bar{x}_2\right) \right] p\left(E_{\ell^+} | m_t\right) p\left(E_{\ell^-} | m_t\right). \qquad (\text{I.6.1})$$

Here, we sum parton distribution functions $F(x)$, evaluated at $Q^2 = m_t^2$ over the possible leading order initial parton states $(u\bar{u}, \bar{u}u, d\bar{d}, \bar{d}d,$ and $gg)$; x_1 and x_2 are the Björkén x values for the initial state partons. The variable $p(E|m_t)$ is the probability density of observing a charged lepton of energy E in the rest frame of a top quark of mass m_t, given by [37]:

$$p(E|m_t) = \frac{4 m_t E(m_t^2 - m_b^2 - 2 m_t E)}{(m_t^2 - m_b^2)^2 + M_W^2(m_t^2 - m_b^2) - 2 M_W^4}. \qquad (\text{I.6.2})$$

For each top mass hypothesis, we find an overall weight by summing the weights of all found solutions. For some events, however, no solutions are found for any top mass hypothesis, usually because of hard gluon radiation removing the correlation between jet and quark momentum or detector resolution-related mismeasurements of momenta. We compensate for this by reconstructing each event, in both data and MC, 500 times, each time with jet momenta drawn randomly from Gaussian distributions of width given by the detector resolution and with mean given by the measured momentum [38]. We average the weights of each hypothesis mass over each reconstruction to find the event's final weight curve. After this randomization procedure, we observe very high rates of successful mass estimator reconstruction, shown for data in Table 9 and for MC in Table 10. Without the resolution smearing the solutions are found only 86% of the times [39]

Table 9: Percentage of events with at least one mass solution in data.

b-tag category	Events passing cuts	Events with a solution	% of events with a solution
1 b-tag	29537	27465	93.0%
$\geq 2b$-tags	40862	38792	95.0%
$\geq 1b$-tag	70399	66257	94.1%

Table 10: Percentage of events with at least one mass solution in signal MC events with $m_t = 172.5$ GeV.

b-tag category	Events passing cuts	Events with a solution	% of events with a solution
1 b-tag	25479	24050	94.4%
$\geq 2b$-tags	38893	37291	95.9%
$\geq 1b$-tag	64372	61341	95.3%

We estimate the top quark mass by extracting the hypothesis mass with the highest average sum weight for each event, called the peak mass m_{peak}. In Figure I.6.1 we show distributions of m_{peak} in data and for MC simulation with $m_t = 172.5$ GeV; here, as above, we see good agreement between data and simulation.

In previous iterations of the analysis, we instituted a lower cut on the sum weight itself, with the intention of removing badly reconstructed or mismeasured events [2, 33]. However, with the

2012 datasets and MCs, we expect the statistics to be sufficiently large that the measurement is robust against this form of noise, and instead merely require that all events have at least one mass solution, and hence positive peak weight.

We do not claim that the peak mass itself is an unbiased measurement of the top quark, merely that it is strongly correlated with the physical top mass. Instead, we perform a true unbiased measurement by comparing the distribution of m_{peak} in data to simulated distributions evaluated at a range of sample top quark masses, as described in the next section.
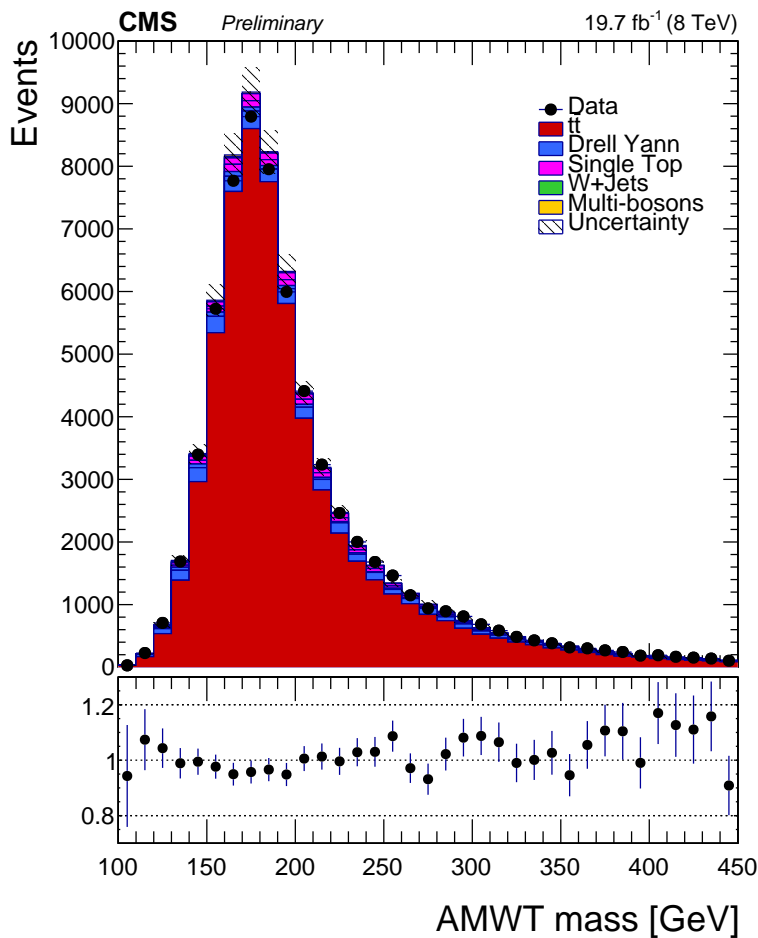
Figure I.6.1: Distribution of the peak mass observed in data and in the simulation for a top mass hypothesis of 172.5 GeV.

I.7   Top Mass Estimate from Template Fits

Our measurement of the top mass is a likelihood fit of the distribution of m_{peak} to templates obtained from Monte Carlo simulations. Templates are generated for samples with masses between $166.5\,\mathrm{GeV}/c^2$ and $178.5\,\mathrm{GeV}/c^2$ in steps of $3\,\mathrm{GeV}/c^2$, with additional templates at $m_t = 171.5\,\mathrm{GeV}/c^2$ and $173.5\,\mathrm{GeV}/c^2$.

The likelihood fit can simultaneously fit data split into several categories, such as b-tag multiplicities and lepton content (i.e. ee, $e\mu$, and $\mu\mu$ channels). In previous analyses, this was found to be beneficial [2, 33]. As will be discussed below, we separate events by b-tags but not leptons, and hence perform a two-category fit. Similarly, in the 2011 analysis, events with $m_{peak} > 300$ GeV/c^2 were cut to exclude the effects of the low-statistics high-mass tail of the distribution. Here, we instead cut events with $m_{peak} > 400$ GeV/c^2.

Each template is fit to data; for each mass point, different categories are treated as separate templates in a simultaneous fit. Following the previous iterations of this analysis, we fit a parabola to the negative logarithms of the likelihoods obtained from the fits in the range spanned by the MC sample masses.

The backgrounds considered are Drell-Yan, single top production, W+Jets, and diboson events. In the fit, the total number of events is not considered; instead, we fix the expected ratio of signal to background, and examine the shapes of the template and data distributions. Because each MC sample distribution has a different m_{peak} profile, it is necessary to fix their relative normalizations in the templates. This is done by normalizing each MC distribution to the sample cross section times luminosity; the sole exception is the DY background, for which the normalization is estimated from data.

I.7.1 Study of the Method on Simulated Data

To study the validity of our technique, we generate 1000 pseudo-experiments at sample top masses equal to those of the MC mass points used in the fit, and examine how close the measured masses are to the input masses. In each pseudo-experiment, signal and background events are generated from a Poisson distribution with mean given by the number of expected events in each channel. The measurement is performed as described above, and we extract a measured mass. A Gaussian is fitted to the distribution of the measured masses; the mean of this Gaussian is called the mean measured mass. The pull width of the distribution is given by the standard deviation of a separate Gaussian fitted to the standardized residual distribution.

We begin with categorization of the data. Multiple such categorizations are possible. In general, these come from splitting by b-tags, lepton content, or both. Calibration tests were performed for several such categorizations, and are summarized in Table 11. The uncertainties found with the different classifications are similar; within the precision of the simulation, all options give essentially the same precision. We choose for convenience to split events only by b-tags. An entirely similar procedure allows us to determine the optimal upper bound for acceptable values of m_{peak}. We examined the influence of removing events with peak mass above 300, 400, and 500 GeV/c^2 on the mean uncertainty of the distribution. These results, summarized in Table 12, indicate that fixing upper bounds of 300 and 400 GeV/c^2 are essentially equivalent, within the precision of the simulation; we choose an upper bound of $m_{peak} < 400$ GeV/c^2.

Table 11: Results of calibration tests for the different event classifications. The corrected uncertainty (CU) is defined as the mean uncertainty times the pull width.

Classification scheme	number cats.	mean uncertainty (GeV)	mass width (GeV)	pull width	CU (GeV)
lepton channels $\{ee, e\mu, \mu\mu\}$	3	0.169	0.163	0.948	0.160
b-tag categories $\{1, \geq 2\ b\text{-tags}\}$	2	0.166	0.161	0.962	0.160
b-tag and leptons	6	0.165	0.158	0.952	0.157

23

Table 12: Results of calibration tests for the different upper bounds on m_{peak}. The corrected uncertainty is defined as the mean uncertainty times the pull width.

Upper bound (GeV)	mean uncertainty (GeV)	mass width (GeV)	pull width	corrected uncertainty (GeV)
300	0.163	0.162	0.962	0.157
400	0.166	0.161	0.962	0.160
500	0.170	0.174	0.999	0.170

In tests of the systematic uncertainty of our measurement, it has been seen that a tighter selection consisting only of events with ≥ 2 b-tags yields a smaller overall uncertainty than the looser selection of events with ≥ 1 b-tag. Thus, we will perform the final fit with one category, looking only at events with ≥ 2 b-tag and with 100 GeV$/c^2 < m_{peak} < 400$ GeV$/c^2$.

Lastly, with our most accurate categorization and bounds, we perform a final calibration. The calibration curves are shown in Fig I.7.1. We observe a bias below 0.1 GeV$/c^2$ everywhere between 169.5 and 175.5 GeV$/c^2$. A line fit to the bias points serves as a correction to the bias induced by the calibration. The pull widths indicate that the statistical uncertainty is overestimated slightly, by about 4% for $m_t = 172.5$ GeV$/c^2$. Taking this overestimation into account, we expect a statistical uncertainty of ± 0.20 GeV$/c^2$ on the final result.

I.7.2   Result with Data

Using data events, the top mass is measured to be $m_t = 172.77 \pm 0.20$ GeV. The distribution of the -log(likelihood) points is shown in Fig. I.7.2. After correcting for the fit bias, the mass of the top quark is measured to be $m_t = 172.82 \pm 0.20$ (stat.) ± 1.22 (syst.) GeV.
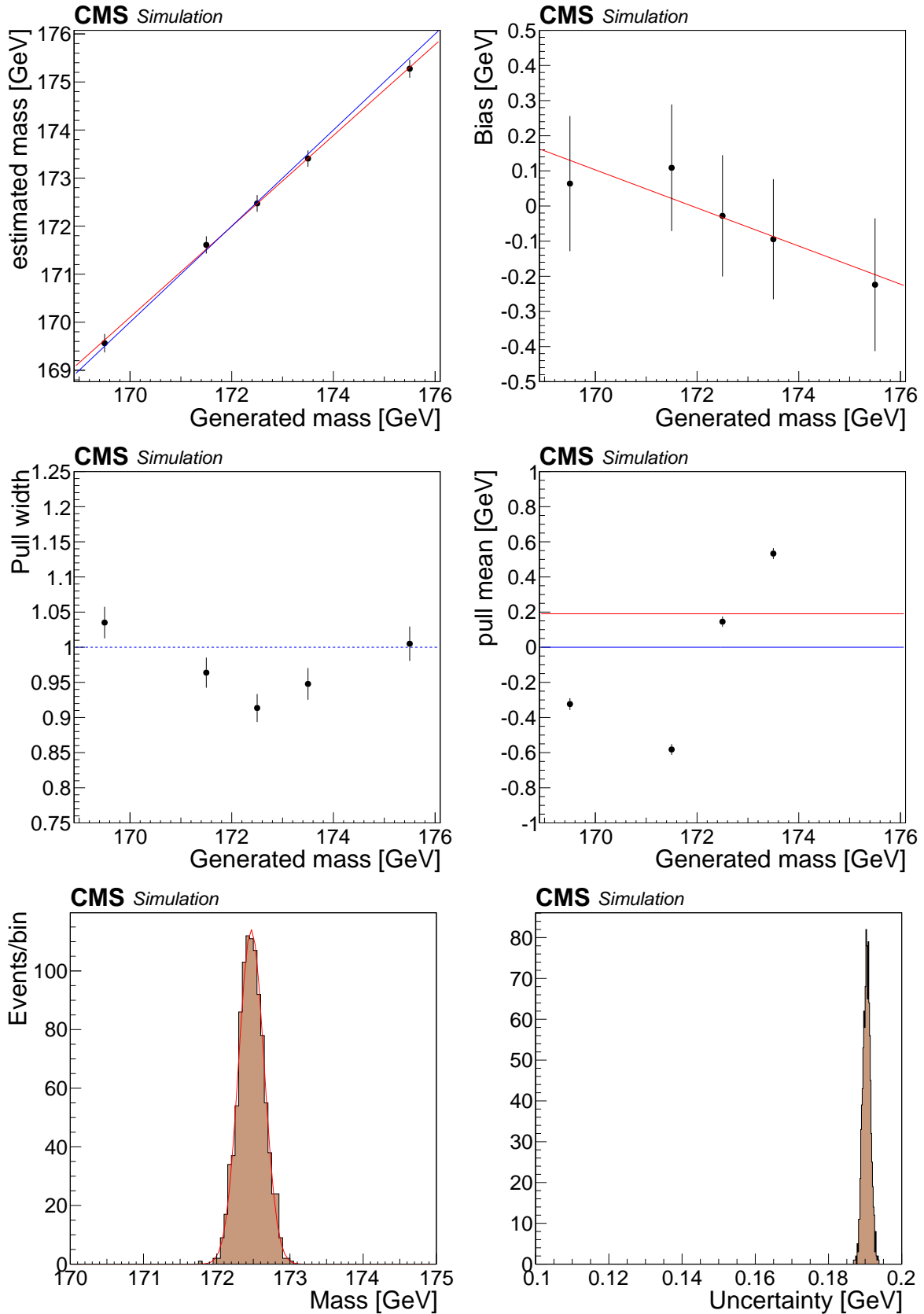
Figure I.7.1: Mean measured mass (top left), and mass bias (top right), pull (middle left) width and pull mean (middle right) for different mass hypotheses. The bottom row shows the distribution of fitted masses (left) and uncertainties (right) of the calibration tests for a mass hypothesis of 172.5 GeV/c^2.
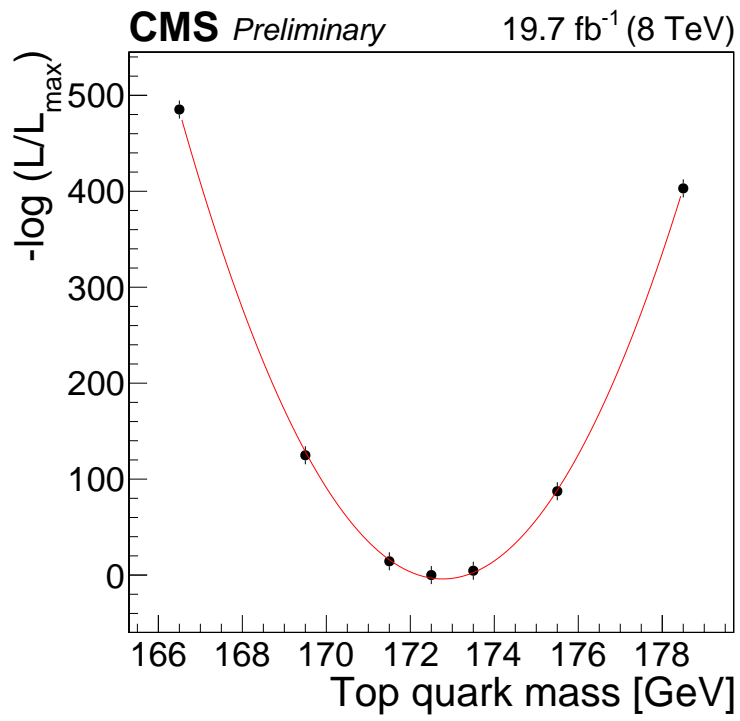
Figure I.7.2: Distribution of the -log(likelihood) points for the data.

I.8 Systematic Uncertainties

The contributions from the different sources of uncertainty are summarised in Table 13. We calculate systematic uncertainties with the prescription outlined in [40], in which systematics are calculated by comparing the mean measured masses of pseudodata derived from modified and unmodified templates. Generically, these modified templates are generated with some systematic variable modified, usually by $\pm 1\sigma$ in the form of up- and down-templates.

- Jet energy Scale (JES):

  The uncertainty of the overall jet energy scale is the dominant source of uncertainty on m_t. It has been evaluated for the different independent sources of systematic uncertainty. To estimate the effect of each source on the measurement of m_t, the (p_T, η)-dependent uncertainty is used to shift concurrently the energy of each jet by $\pm 1\sigma$ with respect to its nominal value, and correcting the $\not{E}_T$ accordingly. For each source, pseudo-experiments are generated from simulated event samples for which the JES is varied by the relevant uncertainty, and the reconstructed top-quark mass distributions are fitted with the templates derived with the nominal JES. The average variation of the top-quark mass is used to estimate the systematic uncertainty. The uncertainties due to the different sources are listed in Table 14. The quadratic sum of the variation for each source is taken as the systematic uncertainty.

- b-quark JES and Hadronization Modeling

  The b-flavour dependent uncertainties arising from the simulation of the parton-jet modeling and the accompanying JES uncertainty are composed of three contributions:

  - flavor-dependent JES term: Depending on the origin of the jets, the jet energies are varied within their respective flavour-dependent uncertainties. The uncertainties for jets from light quarks, b quarks and gluons are evaluated separately and added linearly.
  - b-fragmentation term: The impact of b-fragmentation hardness is estimated by varying x_B in the Lund fragmentation model between the PYTHIA Tune Z2* and the experimental results from ALEPH [41] and DELPHI [42].
  - Semi-leptonic branching fraction term: The semi-leptonic branching fraction of b hadrons is varied within the uncertainties [18].

- Jet energy resolution (JER):

  Since the jet energy resolution in Monte Carlo events is corrected for the observed mismatch, the uncertainty on the top mass is determined by varying the resolution by its uncertainty [43].

- Lepton energy scale:

  An uncertainty of 0.5% is considered for electrons reconstructed in the barrel and 1.5% in the endcap [44]. An uncertainty of 0.2% is considered for muons [45]. These uncertainties have a minimal impact on the result.

- Unclustered MET:

  The scale of the residual unclustered energy contribution to the $\not{E}_T$ is varied by $\pm 10\%$.

- Pile-up:

  Pile-up collisions will give rise to extra jets in the detector. To study the effect of this, a variation of 5% of the total inelastic cross section is considered.

- b-tagging efficiencies:

  The uncertainty due to 1-tagging efficiency was evaluated by varying the 1-tagging efficiency and mistag rates of the algorithm by their respective uncertainties [29]. The two sources are considered separately.

- Fit calibration:

  The calibration of the fit itself induces an additional systematic uncertainty to the overall result, taken to be the precision with which the calibration at the measured value of the top quark mass is determined. From the fit to the mean mass values of the pseudoexperiments we find that this uncertainty is about 0.03 GeV.

- Background:

  To estimate the influence of the number of background events on the fit, the level of background used when generating the pseudo experiments is varied. For the DY background, which is estimated from data, an uncertainty of 30% is used. For the remaining backgrounds, W+Jets and single top, we scale the background up and down by the uncertainty of the cross-section, using the calculated cross-sections given in [46].

- Generator modelling:

  The uncertainty due to the modelling of the signal templates by the Monte Carlo generator are studied by comparing the results of the pseudo-experiments using the reference sample to that from a sample generated with the POWHEG generator.

- Top quark p_T reweighting:

  The impact of the difference between the transverse momentum distribution of top quarks in data and the simulation [47] is evaluated by applying a scale factor to the simulated events to correct for this mismatch. The difference between the results of the pseudo-experiments using this sample and the reference sample is taken as systematic uncertainty.

- Jet-parton matching scale and factorization scale:

  The Monte Carlo samples shown in Table 3, where the jet-parton matching scale and factorization scale have been increased and decreased, are used to evaluate the effect of these variations on the measurement.

- Underlying event (UE):

  The uncertainties due to the underlying event are estimated by comparing alternative PYTHIA tunes with increased and decreased underlying event activity relative to a central tune. The results for the top-quark mass measured in pseudo-experiments using the Perugia 2011 tune are thus compared to the Perugia 2011 mpiHi and Perugia 2011 Tevatron tunes [48]. The difference found between the two samples is taken as an estimate of the uncertainty in the modelling of the underlying event in our simulation.

- Color reconnection (CR):

  The Perugia 2011 noCR tune is a variant in which colour reconnection effects are not taken into account. The difference in the average top-quark mass, measured with and without colour reconnection effects, is taken as the estimate for the colour reconnection systematic uncertainty.

- PDF: To evaluate the systematic uncertainties arising from the parton density functions, the procedure outlined in Ref. [49] is followed.

Table 13: Categories of systematic uncertainty, along with their respective contributions to the overall systematic uncertainty. The symmetrized uncertainty is defined as $\Delta m_t \equiv \frac{1}{2}(|\Delta m_t^{up}| + |\Delta m_t^{down}|)$. Bold face entries appear in the systematics summary table in the PAS.

Source of uncertainty	δm_{t} (GeV)
Fit calibration	0.03
p_T- and η-dependent jet energy calibration	0.37
Lepton energy scale	0.12
Unclustered missing p_T	0.06
Jet energy resolution	0.06
b tagging	0.04
Pile-up	0.12
Non-$t\bar{t}$ background	0.02
Flavor-dependent jet energy scale	0.28
b fragmentation	0.69
Semi-leptonic b hadron decays	0.17
Parton distribution functions	0.16
Renormalization and factorization scales	0.75
Parton-shower matching threshold	0.12
Matrix-element generator	0.35
Underlying event	0.04
Color reconnection modeling	0.11
Total	1.22

I.9   Conclusion

In conclusion, we have presented a measurement of the top quark mass from dilepton $t\bar{t}$ decays, using CMS data corresponding to an integrated luminosity of 19.7 fb^{-1}. We measure the top mass to be $m_t = 172.82 \pm 0.20$ (stat.) ± 1.22 (syst.) GeV. This value is in good agreement with the world average from measurements at the Tevatron and the LHC of $m_t = 173.34 \pm 0.76$ GeV [50] which does not contain any input from the data used for this measurement.

Table 14: Components of the overall JEC contribution to the systematic uncertainty.

Category	Component	Δm_t^{up} (GeV/c^2)	Δm_t^{down} (GeV/c^2)	Δm_t (GeV/c^2)
In-situ correlation group	AbsoluteMPFBias	0.258	-0.221	0.239
JEC inter-calibration group	RelativeFSR	0.036	-0.018	0.027
JEC Pile-up		0.112	-0.127	0.117
	PileUpDataMC	0.074	-0.041	0.057
	PileUpPtBB	0.006	0.024	0.015
	PileUpPtEC1	-0.003	0.005	0.004
	PileUpPtEC2	0.013	0.02	0.017
	PileUpPtHF	0.023	0.026	0.025
JEC uncorrelated group				0.528
	AbsoluteStat	0.026	0.008	0.017
	AbsoluteScale	0.103	-0.102	0.102
	SinglePionECAL	-0.098	0.126	0.112
	SinglePionHCAL	-0.144	0.165	0.154
	RelativeJEREC1	0.014	0.005	0.009
	RelativeJEREC2	0.017	0.007	0.012
	RelativeJERHF	0.022	0.01	0.016
	RelativePtBB	0.072	-0.05	0.061
	RelativePtEC1	-0.12	0.158	0.139
	RelativePtEC2	0.007	0.013	0.01
	RelativePtHF	0.017	0.019	0.018
	RelativeStatEC2	0.011	0.018	0.014
	RelativeStatHF	0.026	0.016	0.021
bJES	Semileptonic B-hadron decays	0.182	-0.182	0.182
	b-fragmentation			0.672
FlavorJES		-0.221	0.342	0.282
	FlavorPureBottom	-0.327	0.360	
	FlavorPureBottom	-0.33	0.341	0.336
	FlavorPureCharm	0.008	0.021	0.015
	FlavorPureGluon	0.084	-0.044	0.064
	FlavorPureQuark	0.017	0.024	0.021

I.A Transverse momentum based reweighting of the $t\bar{t}$ Monte Carlo

Previous analyses have observed that the distribution of top quark transverse momentum is softer in data than in simulation; our data-to-MC comparisons in Figures I.5.1-I.5.6 support this observation. To counteract this phenomenon, MC reweighting scale factors have been calculated [47]. In this Appendix, we demonstrate the effects of this reweighting by displaying data-to-MC comparison plots with the reweighting implemented. As can be seen in FiguresI.A.1-I.A.3, the agreement for the p_T distributions of the leptons and the jets has improved, but the $\not{E}_T$ distributions is now softer in MC (Figure I.A.3). We treat the effects of this reweighting as a systematic uncertainty.

Figure I.A.1: Transverse momentum of the leading (left) and second leading (right) lepton, for data and MC events, using the $m_t = 172.5$ GeV MC sample.
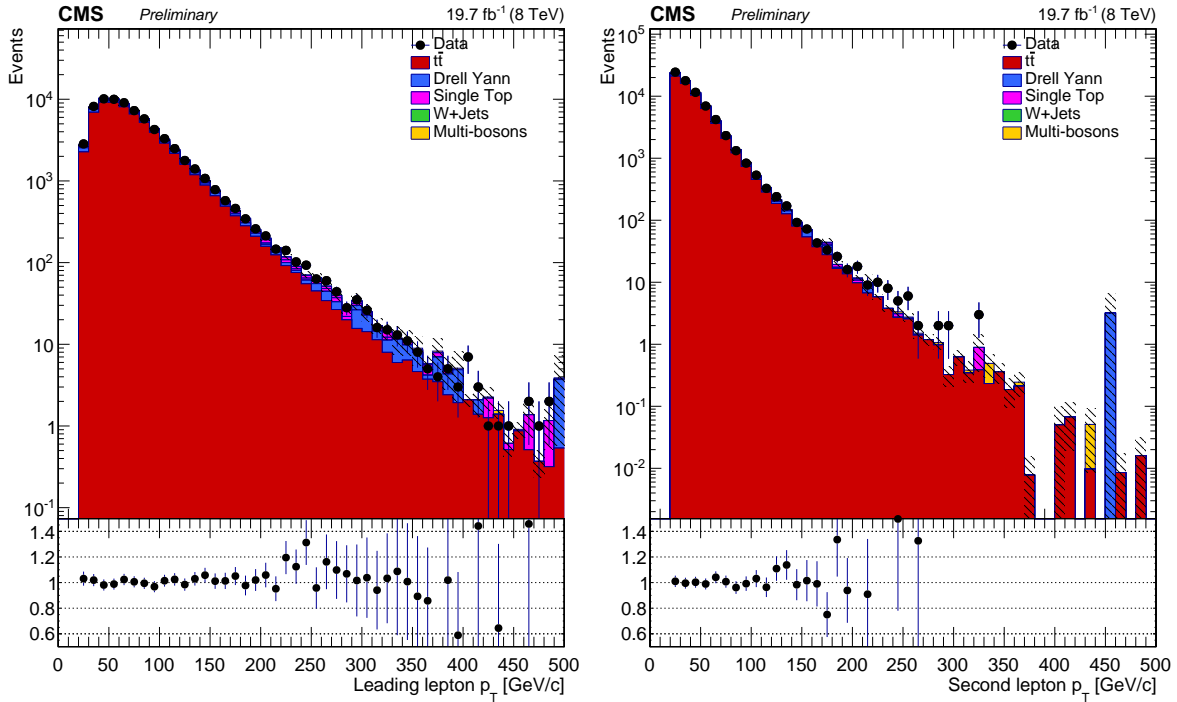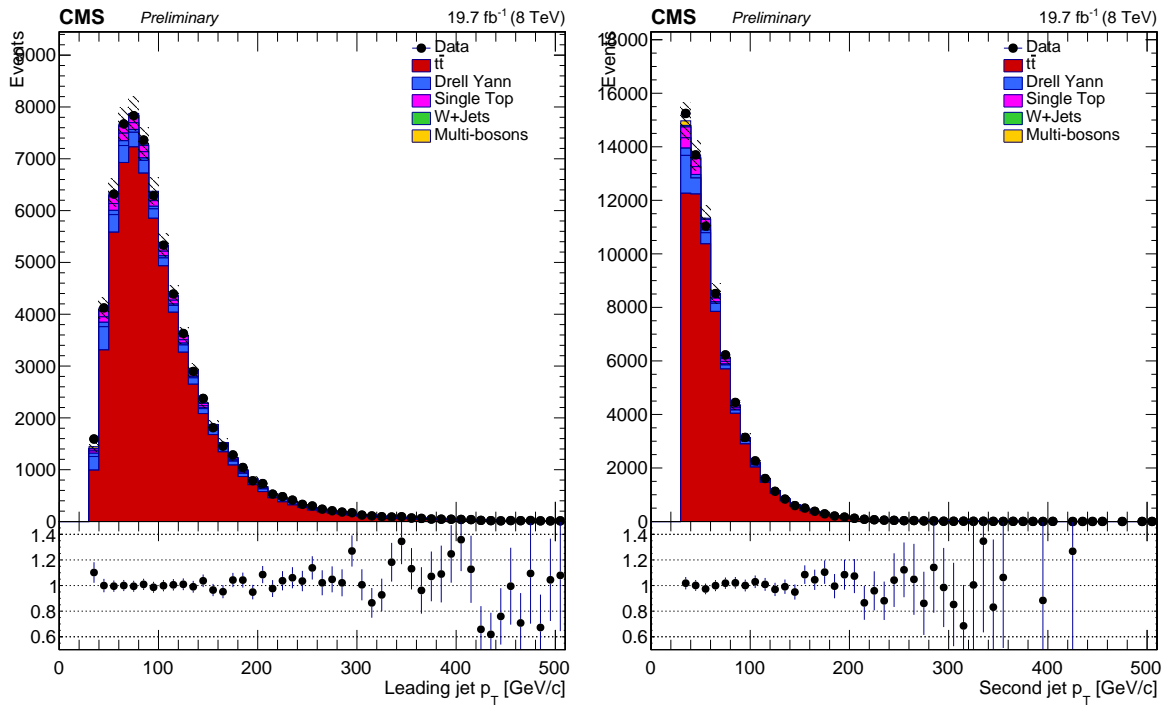
Figure I.A.2: Transverse momentum of the leading (left) and second leading (right) jet, for data and MC events, using the $m_t = 172.5$ GeV MC sample.
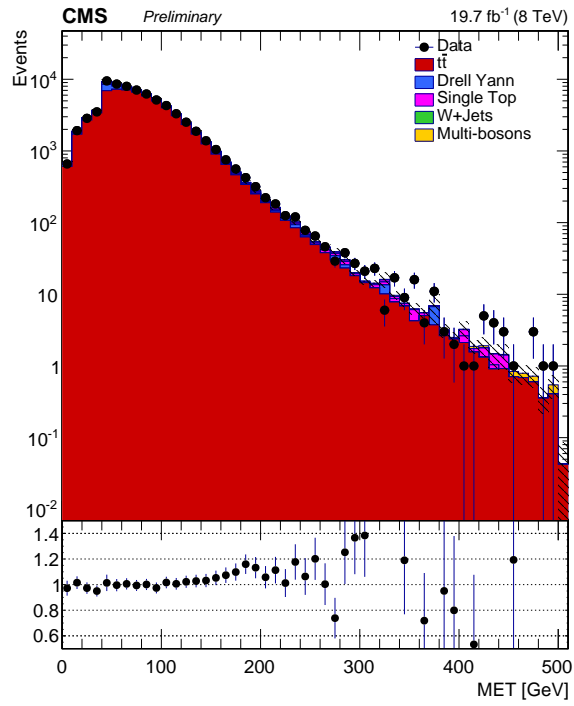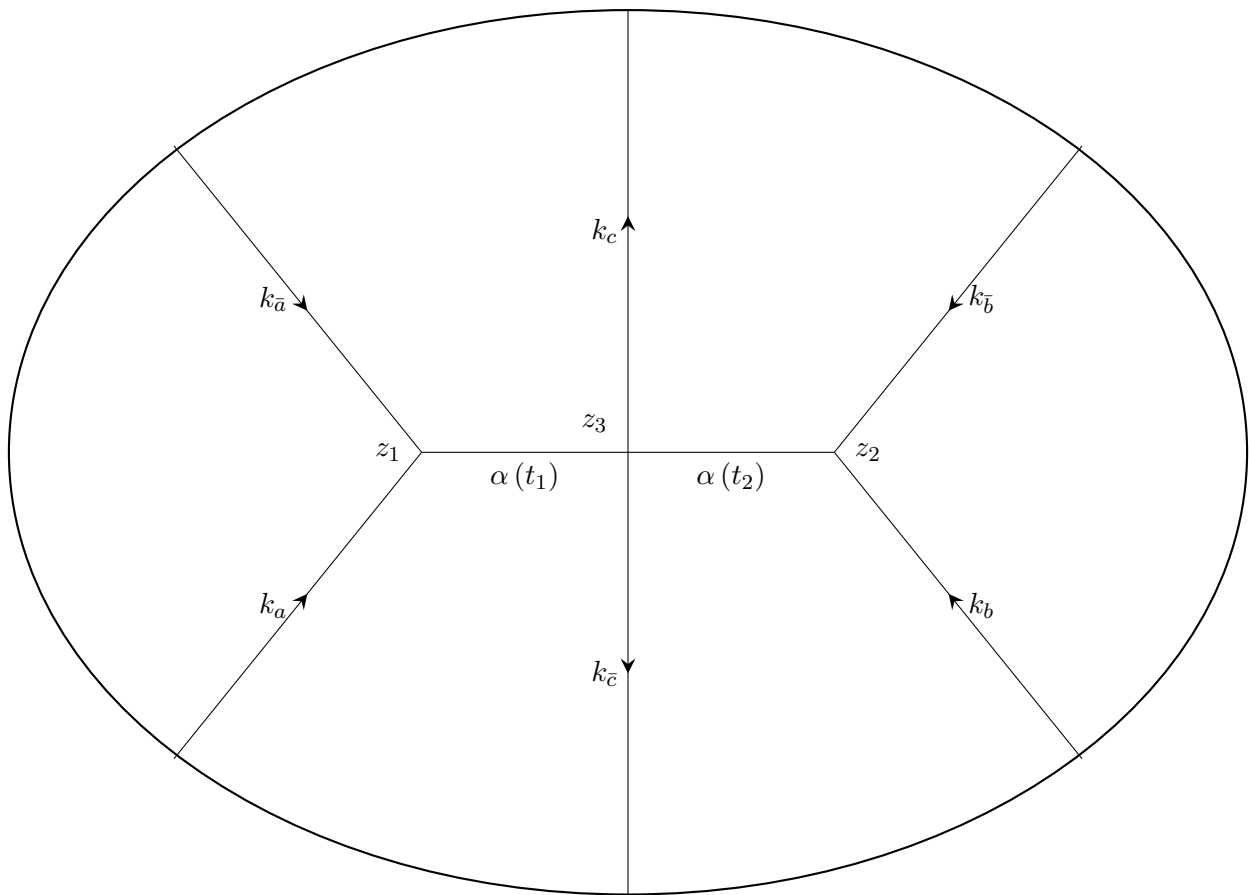
Figure I.A.3: $\displaystyle{\not}E_T$ for data and MC events, using the $m_t = 172.5$ GeV MC sample.

Part II
Computing Inclusive QCD Cross-Sections Through AdS/CFT

Author:
Richard NALLY

Advisors:
Prof. Chung-I TAN

Abstract

A major failing of the initial interpretation of string theory as a model for the strong interaction is its failure to reproduce the empirically observed power-law falloff in the center of mass energy s of certain scattering cross sections. In particular, flat space string theory indicates that the cross section for $2 \to 2$ scattering at fixed angle decays exponentially in s. Here we will demonstrate that curved space string theory can remediate this problem in the case of inclusive single particle production of the form $ab \to cX$ in the large center of mass limit. Starting with a brief review of string theory, we will demonstrate that flat space string theory predicts exponential behavior for this cross section. Then, motivated by the success of curved space string theory to calculate the exclusive fixed-angle $2 \to 2$ scattering cross section, we will discuss string theory in curved space, and in particular the AdS/CFT correspondence between theories of gravity and gauge theories, before demonstrating that the curved space prescription indeed yields results that agree with the empirical phenomena.

II.1 Introduction

Before its modern incarnation as a proposed theory of quantum gravity, string theory was proposed with the much more modest intent of modeling the strong interaction. What is now known as string theory was originally called the dual resonance model, and was intended to provide a way to calculate scattering amplitudes that captured the empirically known Regge phenomenology of strong-mediated scattering [51–53]; the dual resonance model corresponds to what in modern parlance is called flat-space string theory. Although initially quite successful in this goal, the dual resonance model was eventually discarded. Extremely characteristic of its predictions were exponential dependences of amplitudes and cross-sections on the center-of-mass energy s, whereas the physical dependence follows a power law [54–56]; this power law dependence hold good at least until center-of-mass energies of the scale of the Large Hadron Collider (LHC) [57]. A poignant example comes from fixed angle $2 \to 2$ scattering, which in flat space has an exponential decay but experimentally decays only via a power law in s. Eventually, it was shown that Yang-Mills gauge theories yield the correct prediction, and the current SU(3) description of the strong interaction was adopted.

More recently, however, string theory has regained traction as a method to describe strong interactions. It has famously been argued [58] by Maldacena that strings propagating in anti-de Sitter space should have the same dynamics as gauge theories defined on the boundary of this space. In the nearly twenty years since it was conjectured, this so-called "AdS/CFT correspondence" has been the subject of thousands of papers, and the holographic ideas it has inspired have been applied to topics ranging from quantum information theory [59] to condensed matter physics [60]. Most importantly for our purposes, however, AdS/CFT has found great success in describing QCD-like theories. This AdS/QCD correspondence has helped elucidate aspects of QCD ranging from nonperturbative features such as the glueball spectrum [61–63] to calculations of scattering amplitudes [64–69]. Here we will concern ourselves primarily with the use of AdS/QCD to compute cross-sections.

In particular, here we are interested in applying the AdS/QCD correspondence to compute the inclusive single-particle production cross section in QCD; this process is depicted schematically in Figure II.1.1. More precisely, we examine the process $ab \to cX$, where c is a produced central particle with fixed momentum $\mathbf{p}_c$ and X represents some other number of particles produced in

the scattering process, and compute the inclusive cross section

$$\sigma_{inc} \equiv \frac{d^3\sigma_{ab\to cX}}{d\mathbf{p}_c^3}. \tag{II.1.1}$$

We take the produced particles X to have invariant-mass-squared $M^2 = (p_a + p_b - p_c)^2$, but are otherwise uninterested in the properties of X. We work in the limit where the center of mass energy $s \to \infty$. In the context of flat space string theory, this process was studied in [70], which, following an approach suggested in [71], found that the cross section decays exponentially in the center of mass energy.
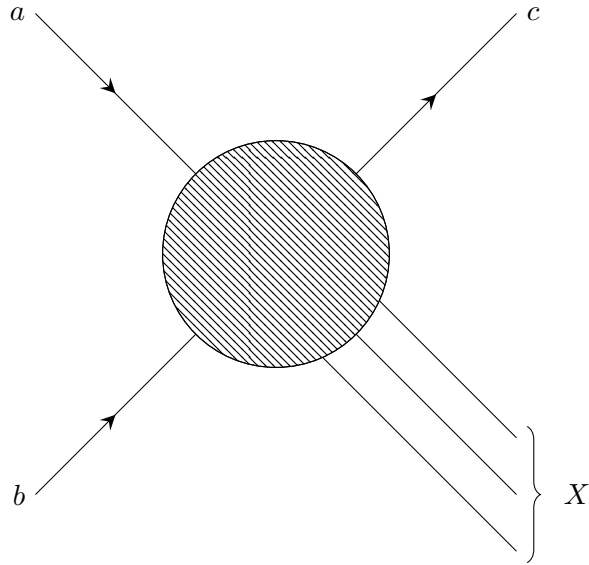
Figure II.1.1: Inclusive single-particle production. The produced particles X are taken to have invariant mass-squared M^2.

In [70], the flat-space string theory prediction for this cross section is evaluated by taking advantage of a generalized optical theorem which relates the desired cross section to the discontinuity amplitude for $3 \to 3$ scattering. We will follow this same method to evaluate the curved space string theory prediction for the cross-section.

In Section II.2, we will discuss flat-space string theory and its application to scattering in gauge theories. In particular, Section II.2.1 features a review of the essentials of flat-space string theory, which segues in Section II.2.2 to a discussion of the simplest possible scattering of strings, the Virasoro-Shapiro amplitude. In Section II.2.3, we will, after a brief discussion of the optical theorem Eq. II.2.81, summarize the results of [70], and derive the flat-space string theory prediction for the inclusive single-particle production cross section. Next, in Section 3 we will discuss curved space string theory, starting in Section II.3.1 with an overview of the AdS/CFT correspondence before moving on to a variant of the conjecture compatible with confining field theories in II.3.2 and then summarizing the results of [64] in Section II.3.3. Finally, we will in Section 4 compute the curved-space string theory prediction for the inclusive cross section. We will conclude with a brief discussion of our essential results in Section 5.

36

II.2 String Scattering in Flat Space

In this section we will discuss some important results in flat space string theory. We will begin with a brief overview of the critical bosonic string, and then proceed to discuss string scattering, giving two examples: a simple example of $2 \to 2$ string scattering in flat space and the case of interest, $3 \to 3$ string scattering.

II.2.1 An Overview of Bosonic String Theory

Here we aim to provide a brief introduction to bosonic string theory. Of course, this is a vast subject, and numerous texts have been written on it, such as [72–76]. We neither can nor will attempt to cover the whole subject; instead, we will follow the discussion in [74,77] to call attention to some of the most important results in the theory before specializing to the topics in flat space string theory most relevant to our work on cross sections.

II.2.1.1 Formalism, Geometry, and the Equations of Motion

Bosonic string theory is in its modern incarnation viewed as a theory of D real bosonic fields X^μ defined on a two-dimensional base manifold; this base manifold is called the string worldsheet, denoted by Σ, and can be viewed as a straightforward generalization of the concept of the worldline of a point particle. The trajectory of a point particle is a map from the interval (τ_1, τ_2), a one-dimensional real manifold, to D-dimensional spacetime, represented once again by fields X^μ. When one transitions from studying point particles to particles with extent in space as well as in time, one must add an additional dimension to the time interval; this two-dimensional space is the string worldsheet.

Quantitatively, we parameterize Σ with coordinates τ and σ, with τ timelike and σ spacelike, and define a metric $h_{\alpha\beta}$ on the worldsheet. The D bosonic fields are taken to be coordinates in a D-dimensional target spacetime manifold with metric $g_{\mu\nu}$. In general, we shall use label worldsheet indices as $\alpha, \beta, \gamma, \delta \in 0, 1$ and spacetime indices as $\mu, \nu, \rho, \lambda \in 0, 1, 2, \ldots, D-1$.

To arrive at an action for the worldsheet string theory, we will return to the point particle analogy. The equations of motion for a (massive) point particle are derived from an action of the form

$$S_{point} = m \int ds = m \int d\tau \sqrt{g_{\mu\nu} \frac{dX^\mu}{d\tau} \frac{dX^\nu}{d\tau}}, \tag{II.2.1}$$

where m is the particle's mass and τ is a parameter along the worldsheet. In particular, the action corresponds to the path length traversed by the point particle in its motion, and is given by an integral over the one-dimensional worldline. The natural analogue of path length in a two-dimensional space is area, so it is reasonable to hypothesize that the string action is given by

$$S_{NG} = T \int_\Sigma dA = T \int_\Sigma d^2\sigma \sqrt{\left(g_{\mu\nu} \frac{\partial X^\mu}{\partial \tau} \frac{\partial X^\nu}{\partial \sigma}\right)^2 - g_{\mu\nu} g_{\rho\lambda} \frac{\partial X^\mu}{\partial \tau} \frac{\partial X^\nu}{\partial \tau} \frac{\partial X^\rho}{\partial \sigma} \frac{\partial X^\lambda}{\partial \sigma}}, \tag{II.2.2}$$

where T is the string tension. This is known as the Nambu-Goto action, and is the correct action for worldsheet string theory. The Nambu-Goto action is classically equivalent to (i.e. gives the same equations of motion as) a different action, known as the Polyakov action:

$$S = \frac{1}{4\pi\alpha'} \int_{\Sigma} d^2\sigma \sqrt{-h} h^{\alpha\beta} \partial_\alpha X^\mu \partial_\beta X^\nu g_{\mu\nu}, \tag{II.2.3}$$

where $\alpha' = \frac{1}{2\pi T}$ is a string parameter known as the Regge slope and $h = \det h_{\alpha\beta}$. The Polyakov action takes the form of a sigma model action, and heuristically corresponds to the alternate point particle metric

$$S_{point} = m \int d\tau g_{\mu\nu} \frac{dX^\mu}{d\tau} \frac{dX^\nu}{d\tau}. \tag{II.2.4}$$

We will take the Polyakov action as the string action going forward. Because in this section we are interested in flat space string theory, we will make the simplifying assumption

$$g_{\mu\nu} = \eta_{\mu\nu} = \begin{pmatrix} 1 & & & & \\ & -1 & & & \\ & & \ddots & & \\ & & & -1 & \\ & & & & -1 \end{pmatrix}. \tag{II.2.5}$$

From the Polyakov action we can read off several symmetries of the worldsheet theory. Firstly, because in the target space this action is a Lorentz scalar, we have invariance under the generalized Poincare group $SO(1, D-1) \rtimes \mathbb{R}^D$, which acts on the X^μ by

$$X^\mu \to X'^\mu = X^\mu + \varepsilon^\mu_\nu X^\nu + c^\mu, \tag{II.2.6}$$

where $\varepsilon^\mu_\nu = -\varepsilon^\nu_\mu$ is an infinitesimal generator. Similarly, the action is invariant under worldsheet reparameterizations of the form

$$\sigma^\alpha \to \sigma'^\alpha = f^\alpha(\sigma^\alpha) \tag{II.2.7a}$$

$$h_{\alpha\beta} \to h'_{\alpha\beta} = \frac{\partial f^\gamma}{\partial \sigma^\alpha} \frac{\partial f^\delta}{\partial \sigma^\beta} h_{\gamma\delta}. \tag{II.2.7b}$$

Both of these symmetries are also found in the point particle action, and fundamentally correspond to special relativity in the target space. The Polyakov action, however, has one extremely important symmetry that has no analogue in the point particle case: Weyl symmetry, invariance under the rescaling transformation

$$h_{\alpha\beta} \to h'_{\alpha\beta} = e^{q(\sigma)} h_{\alpha\beta}. \tag{II.2.8}$$

Because of its relative novelty and paramount importance, we will explicitly demonstrate the Weyl invariance of the Polyakov action. Clearly,

$$\sqrt{-h'} = \sqrt{\det h'_{\alpha\beta}} = \sqrt{-\det \begin{pmatrix} e^q h_{00} & e^q h_{01} \\ e^q h_{10} & e^q h_{11} \end{pmatrix}} = \sqrt{-e^{2q}(h_{00}h_{11} - h_{01}h_{10})} = e^q \sqrt{-h}. \tag{II.2.9}$$

Similarly, because $h^{\alpha\beta}$ is the matrix inverse of $h_{\alpha\beta}$, we have

$$h'^{\alpha\beta} = e^{-q} h^{\alpha\beta}. \tag{II.2.10}$$

38

Then

$$S' = \int_\Sigma d^2\sigma \sqrt{-h'} h'^{\alpha\beta} \partial_\alpha X^\mu \partial_\beta x^\nu \eta_{\mu\nu}$$

$$= \int_\Sigma d^2\sigma \sqrt{-h} e^{-q} e^q h^{\alpha\beta} \partial_\alpha X^\mu \partial_\beta x^\nu \eta_{\mu\nu}$$

$$= \int_\Sigma d^2\sigma \sqrt{-h} h^{\alpha\beta} \partial_\alpha X^\mu \partial_\beta x^\nu \eta_{\mu\nu}$$

$$= S. \tag{II.2.11}$$

We note briefly that the reparameterization and Weyl symmetries of the Polyakov action can be conceived of as a sort of gauge symmetry in the worldsheet metric $h_{\alpha\beta}$. In fact, these symmetries are sufficiently robust that they allow us to work in the so-called conformal gauge, in which $h_{\alpha\beta}$ is the two-dimensional Minkowski metric; for now, however, we leave $h_{\alpha\beta}$ arbitrary, and will only impose this gauge condition later. Having described the symmetries of the Polyakov action, we will now derive the equations of motion for string theory.

We begin by considering the worldsheet metric. The action Eq. II.2.3 has no terms of the form $\partial_\gamma h_{\alpha\beta}$, so by the Euler-Lagrange equations we have

$$\frac{\delta S}{\delta h^{\alpha\beta}} = 0. \tag{II.2.12}$$

Motivated by this, we define the worldsheet stress-energy tensor

$$T_{\alpha\beta} = 4\pi\alpha' \frac{1}{\sqrt{-h}} \frac{\delta S}{\delta h^{\alpha\beta}} = 0. \tag{II.2.13}$$

To find an explicit expression for this tensor, we must evaluate the variational derivative:

$$\frac{\delta S}{\delta h^{\alpha\beta}} = \frac{1}{4\pi\alpha'} \frac{\delta}{\delta h^{\alpha\beta}} \left[\sqrt{-h} h^{\gamma\delta} \partial_\gamma X^\mu \partial_\delta X^\nu \eta_{\mu\nu} \right]$$

$$= \frac{1}{4\pi\alpha'} \left[\frac{\delta\sqrt{-h}}{\delta h^{\alpha\beta}} h^{\gamma\delta} + \delta_\alpha^\gamma \delta_\beta^\delta \right] \partial_\gamma X^\mu \partial_\delta X^\nu \eta_{\mu\nu}$$

$$= \frac{1}{4\pi\alpha'} \left[-\frac{1}{2\sqrt{-h}} \frac{\delta h}{\delta h^{\alpha\beta}} h^{\gamma\delta} + \delta_\alpha^\gamma \delta_\beta^\delta \right] \partial_\gamma X^\mu \partial_\delta X^\nu \eta_{\mu\nu}$$

$$= \frac{1}{4\pi\alpha'} \left[-\frac{1}{2\sqrt{-h}} h h_{\alpha\beta} h^{\gamma\delta} + \delta_\alpha^\gamma \delta_\beta^\delta \right] \partial_\gamma X^\mu \partial_\delta X^\nu \eta_{\mu\nu}$$

$$= \frac{1}{4\pi\alpha'} \sqrt{-h} \left[\partial_\alpha X^\mu \partial_\beta X^\nu \eta_{\mu\nu} - \frac{1}{2} \partial_\gamma X^\mu \partial_\delta X^\nu \eta_{\mu\nu} h^{\gamma\delta} h_{\alpha\beta} \right], \tag{II.2.14}$$

where we have used the identity

$$\delta h = h h_{\alpha\beta} \delta h^{\alpha\beta}. \tag{II.2.15}$$

We then have

$$T_{\alpha\beta} = \partial_\alpha X^\mu \partial_\beta X^\nu \eta_{\mu\nu} - \frac{1}{2} \partial_\gamma X^\mu \partial_\delta X^\nu \eta_{\mu\nu} h^{\gamma\delta} h_{\alpha\beta} = 0. \tag{II.2.16}$$

This is an important constraint on the dynamics of the X^μ, and is essential to successfully quantizing the string. The equation of motion for X^μ is somewhat simpler; only derivatives of X^μ enter into the action, so by the Euler-Lagrange equation

$$\partial_\alpha \left[\sqrt{-h} h^{\alpha\beta} \partial_\beta X^\mu \right] = 0. \tag{II.2.17}$$

As it stands currently, the equations of motion are somewhat intractable; we will fix a gauge for $h_{\alpha\beta}$ to simplify them considerably. As alluded to above, the combination of reparameterization and Weyl invariances of the Polyakov action allow us to entirely fix $h_{\alpha\beta}$; reparameterization invariance allows us to fix two of the three degrees of freedom, and Weyl invariance takes care of the third. We will use this to fix

$$h_{\alpha\beta} = \eta_{\alpha\beta} = \begin{pmatrix} 1 & 0 \\ 0 & -1 \end{pmatrix}. \tag{II.2.18}$$

To avoid confusion with the target spacetime metric $\eta_{\mu\nu}$, we will still refer to the worldsheet metric as $h_{\alpha\beta}$. In this gauge, the equations of motion are

$$\partial_\alpha h_{\alpha\beta} \partial_\beta X^\mu = \left(\partial_\tau^2 - \partial_\sigma^2 \right) X^\mu = 0 \tag{II.2.19a}$$

$$T_{00} = T_{11} = \partial_\tau X^\mu \partial_\tau X_\mu + \partial_\sigma X^\mu \partial_\sigma X_\mu = 0 \tag{II.2.19b}$$

$$T_{01} = T_{10} = \partial_\tau X^\mu \partial_\sigma X_\mu = 0. \tag{II.2.19c}$$

These are the equations of motion for the string, also obtainable from the Nambu-Goto action in perhaps a more direct manner. Eq. II.2.19a is in some sense *the* string equation of motion; it represents an independent wave equation for each of the D bosonic fields, which we may now interpret as oscillators. Eqs. II.2.19b and II.2.19c, on the other hand, are constraints; only solutions to Eq. II.2.19a which meet the constraints are viewed as physical solutions to the theory.

II.2.1.2 Solving the Equations of Motion

Having written down the equations of motion in Eq. II.2.19, we would now like to solve Eq. II.2.19a for the spacetime coordinates X^μ. To do this, we must specify boundary conditions for the X^μ. There are three boundary conditions in the literature. We will focus on only one of these conditions, the so-called "closed string" condition

$$X^\mu \left(\tau, \sigma \right) = X^\mu \left(\tau, \sigma + \pi \right). \tag{II.2.20}$$

The other two conditions correspond to open strings, and are unimportant for the particles of interest.

We are now in a position to fully solve the classical equations of motion. To do so, it is convenient to define new "lightcone" coordinates given by

$$\sigma^\pm = \tau \pm \sigma. \tag{II.2.21}$$

In these coordinates, the Equations II.2.19 become

$$\partial_+ \partial_- X^\mu = 0 \tag{II.2.22a}$$

$$T_{++} = \partial_+ X^\mu \partial_+ X_\mu = 0 \tag{II.2.22b}$$

$$T_{--} = \partial_- X^\mu \partial_- X_\mu = 0. \tag{II.2.22c}$$

Then the solution is given by

$$X^\mu\left(\sigma^\pm\right) = X_L^\mu\left(\sigma^+\right) + X_R^\mu\left(\sigma^-\right), \tag{II.2.23}$$

where X_L^μ corresponds to left-moving excitations and X_R^μ corresponds to right-moving excitations. X_L^μ and X_R^μ have Fourier mode expansions given by

$$X_L^\mu = \frac{1}{2}x^\mu + \frac{1}{2}l_s^2 p^\mu \sigma^+ + \frac{i}{2}l_s \sum_{n\neq 0}\frac{1}{n}\tilde{\alpha}_n^\mu e^{-2in\sigma^+} \tag{II.2.24}$$

$$X_R^\mu = \frac{1}{2}x^\mu + \frac{1}{2}l_s^2 p^\mu \sigma^- + \frac{i}{2}l_s \sum_{n\neq 0}\frac{1}{n}\alpha_n^\mu e^{-2in\sigma^-}. \tag{II.2.25}$$

Here we have introduced the center-of-mass position x^μ and momentum p^μ, as well as the string length

$$l_s = \sqrt{2\alpha'}. \tag{II.2.26}$$

For future convenience, we will also define

$$\alpha_0^\mu = \tilde{\alpha}_0^\mu = \frac{1}{2}l_s p^\mu; \tag{II.2.27}$$

this convention will simplify our expression for some important results later on. Because we demand that the spacetime coordinates of the physical string, i.e. the value of the X^μ, be strictly real, we must have

$$\alpha_n^\mu = \left(\alpha_{-n}^\mu\right)^*. \tag{II.2.28}$$

An entirely similar identity holds for the $\tilde{\alpha}^\mu$. In principle, these solutions have D degrees of freedom, one for each of the spacetime oscillators. However, the Virasoro constraints (Eqs. II.2.22b and II.2.22c) remove two of these, leaving us with $D-2$ degrees of freedom. This can be seen explicitly in the light cone gauge, in which we take $X^+ = \tau$. Then the Virasoro constraints can be solved for X^- as a function of the other X^i, leaving us with $D-2$ degrees of freedom. One route towards quantizing string theory, known as light cone quantization, stems from working in this gauge, and is worked out in [76].

II.2.1.3 Quantizing String Theory

We will now set out to quantize this theory; the full procedure of quantizing string theory is quite involved, and we will in the interest of brevity merely emphasize the most salient points. To do so, we compute the conjugate momentum

$$P^\mu = \frac{\delta S}{\delta \partial_\tau X_\mu} = \frac{1}{2\pi\alpha'}\partial_\tau X^\mu \tag{II.2.29}$$

and the equal-time Poisson brackets

$$\left\{P^\mu\left(\tau,\sigma\right), P^\nu\left(\tau,\sigma'\right)\right\} = 0 \tag{II.2.30a}$$

$$\left\{X^\mu\left(\tau,\sigma\right), X^\nu\left(\tau,\sigma'\right)\right\} = 0 \tag{II.2.30b}$$

$$\left\{X^\mu\left(\tau,\sigma\right), P^\nu\left(\tau,\sigma'\right)\right\} = -\eta^{\mu\nu}\delta\left(\sigma - \sigma'\right). \tag{II.2.30c}$$

We can now proceed with a canonical quantization procedure, and replace each of these Poisson brackets with i times a commutator to find that

$$\left[P^\mu\left(\tau,\sigma\right), P^\nu\left(\tau,\sigma'\right)\right] = 0 \tag{II.2.31a}$$

$$\left[X^\mu\left(\tau,\sigma\right), X^\nu\left(\tau,\sigma'\right)\right] = 0 \tag{II.2.31b}$$

$$\left[X^\mu\left(\tau,\sigma\right), P^\nu\left(\tau,\sigma'\right)\right] = i\eta^{\mu\nu}\delta\left(\sigma-\sigma'\right). \tag{II.2.31c}$$

Inserting the expansions Eqs. II.2.24 and II.2.25 and defining the annihilation and creation operators

$$a_m^\mu = \frac{1}{\sqrt{m}}\alpha_m^\mu, \quad \text{and} \quad a_m^{\mu\dagger} = \frac{1}{\sqrt{m}}\alpha_{-m}^\mu, \tag{II.2.32}$$

respectively, we find that

$$\left[a_m^\mu, a_n^{\nu\dagger}\right] = -\eta^{\mu\nu}\delta_{m,n} \tag{II.2.33a}$$

$$\left[\tilde{a}_m^\mu, \tilde{a}_n^{\nu\dagger}\right] = -\eta^{\mu\nu}\delta_{m,n} \tag{II.2.33b}$$

$$\left[a_m^\mu, \tilde{a}_n^{\nu\dagger}\right] = 0. \tag{II.2.33c}$$

These operators look like two independent sets of quantum harmonic oscillators. In particular, we can create states of the form

$$|\psi\rangle = \alpha_{n_1}^{\mu_1\dagger}\alpha_{n_2}^{\mu_2\dagger}\ldots\alpha_{n_m}^{\mu_m\dagger}|0\rangle, \tag{II.2.34}$$

where $|0\rangle$ is the ground state; such states are eigenstates of the momentum operator p^μ. It is worth noting here that there exist states with negative norm. For instance, the state $|\psi\rangle = \alpha_m^{0\dagger}|0\rangle$ has norm

$$\langle\psi|\psi\rangle = \langle 0|\alpha_m^0\alpha_m^{0\dagger}|0\rangle = \langle 0|\left[\alpha_m^0, \alpha_m^{0\dagger}\right]|0\rangle + \langle 0|\alpha_m^{0\dagger}\alpha_m^0|0\rangle = -\langle 0|0\rangle + 0 = -1. \tag{II.2.35}$$

This is unacceptable in a physical theory, and removing such states has important consequences for the internal algebra of the theory.

We can now plug the mode expansions Eqs. II.2.24 and II.2.25 into the lightcone stress-energy conditions to find constraints on the allowed oscillation modes. Quantum mechanically, this discussion must be treated more carefully, so we will give slightly more detail. Recall from Eq. II.2.22b that, in lightcone coordinates,

$$T_{++} = \partial_+ X^\mu \partial_+ X_\mu.$$

A major advantage of the lightcone decomposition Eq. II.2.23 is that the σ^+ dependence is completely decoupled from the σ^- dependence, so that the derivatives in this expression are independent, and we can evaluate T_{++} without considering right-moving solutions at all. From Eq. II.2.24 we can easily read off that

$$\partial_+ X^\mu = \partial_+ X_L^\mu = \frac{1}{2}l_s^2 p^\mu + l_s\sum_{n\neq0}\tilde{\alpha}_n^\mu e^{-2in\sigma^+} = l_s\sum_{m=-\infty}^{\infty}\tilde{\alpha}_m^\mu e^{-2im\sigma^+} \tag{II.2.36}$$

so that

$$T_{++} = l_s^2 \sum_{m=-\infty}^{\infty} \sum_{n=-\infty}^{\infty} \tilde{\alpha}_m^\mu \tilde{\alpha}_\mu^n e^{-2im\sigma+} e^{-2in\sigma+}. \tag{II.2.37}$$

Classically, the ordering of the mode coefficients $\tilde{\alpha}$ is irrelevant, since they are just complex numbers, so we can rewrite II.2.37 and the exactly corresponding result for T_{--} as

$$T_{++} = 2l_s^2 \sum_{m=-\infty}^{\infty} \tilde{L}_m e^{-2im\sigma^+} \tag{II.2.38a}$$

$$T_{--} = 2l_s^2 \sum_{m=-\infty}^{\infty} L_m e^{-2im\sigma^-}, \tag{II.2.38b}$$

where we have introduced the new mode expansion coefficients

$$L_m = \frac{1}{2} \sum_{n=-\infty}^{\infty} \alpha_{m-n} \cdot \alpha_n \tag{II.2.39a}$$

$$\tilde{L}_m = \frac{1}{2} \sum_{n=-\infty}^{\infty} \tilde{\alpha}_{m-n} \cdot \tilde{\alpha}_n. \tag{II.2.39b}$$

These are the famous Virasoro generators, and classically close an algebra given by

$$\{L_m, L_n\} = i(m-n)L_{m+n}. \tag{II.2.40}$$

In quantum mechanics, however, we are not free to simply commute the mode coefficients, as they are operators, rather than numbers. Instead, we must adopt an ordering convention for the creation and annihilation operators. It is conventional to adopt the so-called normal ordering, in which annihilation operators always act to the right of creation operators; a normal ordered product of the operators $\mathcal{O}_1$ and $\mathcal{O}_2$ is written as $: \mathcal{O}_1 \mathcal{O}_2 :$. In the quantized string theory, then, the worldsheet stress-energy conditions $T_{++} = T_{--} = 0$ still take the form

$$T_{++} = 2l_s^2 \sum_{m=-\infty}^{\infty} \tilde{L}_m e^{-2im\sigma^+} \tag{II.2.41a}$$

$$T_{--} = 2l_s^2 \sum_{m=-\infty}^{\infty} L_m e^{-2im\sigma^-}, \tag{II.2.41b}$$

but we now define the normal-ordered Virasoro operators

$$L_m = \frac{1}{2} \sum_{n=-\infty}^{\infty} : \alpha_{m-n} \cdot \alpha_n : \tag{II.2.42a}$$

$$\tilde{L}_n = \frac{1}{2} \sum_{m=-\infty}^{\infty} : \tilde{\alpha}_{m-n} \cdot \tilde{\alpha}_n : . \tag{II.2.42b}$$

43

The normal ordering introduces an ambiguity in L_0 related to convention choice, so in general we expect

$$L_0 = \frac{1}{2} \sum_{n=-\infty}^{\infty} \alpha_{-n}^{\mu} \alpha_{\mu,n} + a = \frac{1}{2}\alpha_0^2 + \sum_{n=1}^{\infty} \alpha_{-n}^{\mu} \alpha_{\mu,n} + a \tag{II.2.43}$$

for some constant a. These normal ordered operators have commutator

$$[L_m, L_n] = (m-n)L_{m+n} + \frac{c}{12}m\left(m^2 - 1\right)\delta_{m+n,0}. \tag{II.2.44}$$

This second term, which has no analogue in the classical theory, can be viewed as stemming from normal ordering conditions; moreover, it can be shown that c, the so-called central charge of the Virasoro algebra, must be equal to the dimension D of the target spacetime manifold.

II.2.1.4 Constructing the State Space

The second term in the commutator has important physical implications. Classically, Eqs. II.2.38 and II.2.22 imply that

$$L_m = \tilde{L}_m = 0 \forall m. \tag{II.2.45}$$

It is tempting to take this vanishing condition as a definition of physical states in the quantum theory, i.e. to demand that, for all physical states $|\varphi\rangle$, we have

$$L_m |\varphi\rangle = \tilde{L}_m |\varphi\rangle = 0, \tag{II.2.46}$$

but this is inconsistent with the commutator Eq. II.2.44. To see this, we simply note that Eq. II.2.46 implies that

$$\langle\varphi| [L_m, L_{-m}] |\varphi\rangle = \langle\varphi|L_m L_{-m}|\varphi\rangle - \langle\varphi|L_{-m} L_m|\varphi\rangle = 0 - 0 = 0. \tag{II.2.47}$$

However, direct evaluation of the commutator yields

$$[L_m, L_{-m}] = 2mL_0 + \frac{D}{12}m\left(m^2 - 1\right), \tag{II.2.48}$$

so Eq. II.2.46 is not a satisfactory condition. Instead, we call a state $|\varphi\rangle$ if it is both annihilated by all L_m for m nonzero, and also satisfies the "mass-shell" condition, i.e. there exists some a such that

$$(L_0 - a) |\varphi\rangle = \left(\tilde{L}_0 - a\right) |\varphi\rangle = 0. \tag{II.2.49}$$

Not all states satisfying this condition are physical; certain states, known as "spurious states", are orthogonal to all physical states. Although in general we will not consider the full details of constructing the physical state space of the bosonic string theory, and hence will not work through the full formalism of the spurious state, we can study these spurious states to determine the appropriate value of a in Eq. II.2.49.

Consider a basis set of states $|\xi_i\rangle$ satisfying $(L_0 - a + i) |\xi_i\rangle = 0 \forall i > 0$, and define the vector

$$|\varphi_{spur}\rangle = aL_{-1} |\xi_1\rangle + bL_{-2} |\xi_2\rangle. \tag{II.2.50}$$

This is a spurious state, and moreover all spurious states can be written in this form through appropriate use of the Virasoro commutator. In particular, we will consider the state

$$|\psi\rangle = L_{-1} |\xi_1\rangle, \tag{II.2.51}$$

where as before $L_m |\xi_1\rangle = 0 \forall \ m > 0$ and $(L_0 - a + 1) |\xi_1\rangle = 0$. $|\psi\rangle$ is a spurious state; let us consider the conditions that make it also a physical state. If it is to be physical, we must have $L_m |\psi\rangle = 0 \ \forall m > 0$ and also $(L_0 - a) |\psi\rangle = 0$. Then

$$0 = L_1 |\psi\rangle = L_1 L_{-1} |\xi_1\rangle = (2L_0 + L_{-1}L_1) |\xi_1\rangle = 2L_0 |\xi_1\rangle + L_{-1}L_1 |\xi_1\rangle = 2(a-1) |\xi_1\rangle + 0, \tag{II.2.52}$$

where we have used Eq. II.2.44 to find $L_1 L_{-1} - L_{-1}L_1 = 2L_0$. By definition, $|\xi_1\rangle \neq 0$, so for this to hold we must have

$$a = 1. \tag{II.2.53}$$

In some sense, a is a free parameter of the theory; we take it to be 1 to maximize the overlap between spurious and physical states. This is desirable because states that are both spurious and physical have zero norm, since spurious states are orthogonal to all physical states, and so they will decouple from the physics of non-spurious physical states without any additional constraints.

II.2.1.5 The Closed String Spectrum

We are now in a position to compute the closed string spectrum, i.e. the properties of excited closed string states. This will directly enable us to compute the dimension D of the target spacetime manifold. We will see that $D = 26$; there are numerous ways of showing this, and we will merely demonstrate one method out of the very many ways of doing so. Consider the number operators

$$N = \sum_{n=1}^{\infty} \alpha^\mu_{-n} \alpha_{\mu,n} = \sum_{n=1}^{\infty} n a^\dagger_{n\mu} a^\mu_n, \ \ \tilde{N} = \sum_{n=1}^{\infty} \tilde{\alpha}^\mu_{-n} \tilde{\alpha}_{\mu,n} = \sum_{n=1}^{\infty} n \tilde{a}^\dagger_{\mu,n} \tilde{a}^\mu_n. \tag{II.2.54}$$

We note that $L_0 = \frac{1}{2}\alpha_0^2 + N$, $\tilde{L}_0 = \frac{1}{2}\tilde{\alpha}_0^2 + \tilde{N}$. Then, since $\alpha_0 = \tilde{\alpha}_0$, for any physical state $|\varphi\rangle$ of the closed string we have

$$0 = \left[L_0 - a - \left(\tilde{L}_0 - a\right)\right] |\varphi\rangle = \left(L_0 - \tilde{L}_0\right) |\varphi\rangle = \left(N - \tilde{n} + \frac{1}{2}\alpha_0^2 - \frac{1}{2}\tilde{\alpha}_0^2\right) |\varphi\rangle = \left(N - \tilde{N}\right) |\varphi\rangle, \tag{II.2.55}$$

and hence we must have

$$N = \tilde{N} \tag{II.2.56}$$

for all closed string states. This is known as the level matching condition, and provides an important relation between the left and right movers.

Consider a vacuum state $|0, 0, k\rangle$, which is an eigenstate of the momentum operator:

$$p^\mu |0, k\rangle = k^\mu |0, k\rangle. \tag{II.2.57}$$

In principle, we should label this state as $|0, 0, k\rangle$, where the first parameter is the number of left moving excitations and the second is the number of right-moving excitations, but by Eq. II.2.56, only states of the form $|N, N, k\rangle$ are allowed, and we can happily proceed with the $|N, k\rangle$ notation. In particular, consider the normalized, physical state

$$|N, k\rangle = \left[\prod_{\mu=1}^{D-2} \prod_{n=1}^{\infty} \frac{\left(a_n^{\dagger, \mu} \right)^{N_{n,\mu}} \left(\tilde{a}_n^{\dagger, \mu} \right)^{N_{n,\mu}}}{N_{n,\mu}} \right] |0, k\rangle, \tag{II.2.58}$$

where $N_{\mu, n}$ is the eigenvalue of $a_{n,\mu}^{\dagger} a_n^{\mu}$ (and, by the level matching condition, also of $\tilde{a}_{n,\mu}^{\dagger} \tilde{a}_n^{\mu}$); following the discussion of Section 2.1.2., we have only allowed for $D - 2$ degrees of freedom. Such a state has a mass given by

$$M^2 = \frac{2}{\alpha'} \left(2 \sum_{\mu=1}^{D-2} \sum_{n=0}^{\infty} n N_{\mu, n} + \frac{2 - D}{12} \right). \tag{II.2.59}$$

This formula is nontrivial to derive; its mysterious-looking second term stems from a zeta-function regularization of the form $(D - 2) \sum_{n=0}^{\infty} n$. Because $\zeta(-1) = -\frac{1}{12}$, this sum after regularization becomes $-\frac{D-2}{12} = \frac{2-D}{12}$.

The state in Eq. II.2.58 is quite general. To examine the spectrum more concretely, it is helpful to consider less general states. First consider the vacuum $|0, k\rangle$. By Eq. II.2.59, this state has mass-squared

$$M_0^2 = \frac{2}{\alpha'} \frac{2 - D}{12} = \frac{2 - D}{6\alpha'}. \tag{II.2.60}$$

Next consider the state $|\psi_1^{\mu\nu}\rangle = a_1^{\dagger \mu} \tilde{a}^{\dagger \mu} |0, k\rangle$. Once again by Eq. II.2.59, the mass of this state is

$$M_1^2 = \frac{26 - D}{6\alpha'}, \tag{II.2.61}$$

since $N_{\mu, n} = 1$ here. This is sufficient to see that we must have $D = 26$, since this state should be invariant under the residual SO(D-2) symmetry of the closed string modes. It is a general theorem of representation theory that rank-2 tensor representations of special orthogonal groups must be massless, so we must have $M_1^2 = 0$, i.e.

$$D = 26. \tag{II.2.62}$$

We can now evaluate the mass in Eq. II.2.60:

$$M_0^2 = \frac{2 - 26}{6\alpha'} = -\frac{4}{\alpha'}. \tag{II.2.63}$$

These are tachyonic modes! This is a serious problem in bosonic string theory, and can only be rectified in superstring theory.

Because we could just as easily have constructed $|\psi_1^{\mu\nu}\rangle$ by exciting modes along any of the $D-2 = 24$ directions, there are $24^2 = 576$ massless tensor states. These correspond to symmetric and

antisymmetric tensor states, and also a scalar state known as the dilaton, which will be especially important later on.

By adding on additional operators of the form $a_i^{\dagger,\mu} a_j^{\dagger,\nu}$ to $|\psi_1^{\mu\nu}\rangle$, one can construct states of the form

$$|\psi_n^{\mu_1\nu_2\mu_2\nu_2\cdots\mu_{n-1}\nu_{n-1}\mu_n\nu_n}\rangle = a^{\dagger,\mu_1}\tilde{a}^{\dagger,\nu_2} a^{\dagger,\mu_2}\tilde{a}^{\dagger,\nu_2}\cdots a^{\dagger,\mu_{n-1}}\tilde{a}^{\dagger,\nu_{n-1}} a^{\dagger,\mu_n}\tilde{a}^{\dagger,\nu_n}|0,k\rangle. \qquad \text{(II.2.64)}$$

In general, one can show that $|\psi_n\rangle$ has a mass given by

$$M_n^2 = \frac{4 - 4n}{\alpha'}. \qquad \text{(II.2.65)}$$

This is the full spectrum of the closed string; all physical states can be created as a sum over the $|\psi_n\rangle$, and each of these states has known mass and tensor behavior (given from the Lorentz indices of the creation operators). This concludes our review of critical bosonic string theory; there are of course more topics to cover in this theory, to say nothing of the entirety of superstring theory, but in the interests of brevity we will terminate this section. In what follows, the general structure of string theory as a quantized theory of the relativistic, two-parameter spacetime surface is probably more important than any specifics of the theory; however, working through this formalism is an interesting exercise.

II.2.2   A Simple Example: $2 \rightarrow 2$ Scattering of Tachyons

Having discussed the basics of flat-space string theory, we will now demonstrate its application to scattering problems. We begin with perhaps the simplest string scattering amplitude, the elastic scattering of two tachyons in flat space, i.e. the process $ab \rightarrow cd$, shown in Figure II.2.1. This is known as Virasoro-Shapiro scattering, and is a historically important problem in string theory; more importantly, studying the Virasoro amplitude will establish a program with which we will attack all future amplitudes. Here we will follow the discussion in [72]; similar discussions can be found in [73, 74].
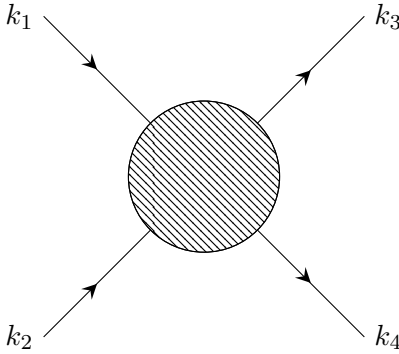

Figure II.2.1: Virasoro-Shapiro scattering of tachyons.

We begin with momenta k_1, k_2, k_3, k_4 and vertices z_1, z_2, z_3, z_4, and will concern ourselves only with the tree-level contribution to this amplitude. Before we can compute the amplitude, however,

we must define kinematical invariants with which to describe the scattering. For $2 \to 2$ scattering, these are the classical Mandelstam variables:

$$s = (k_1 + k_2)^2 \tag{II.2.66a}$$

$$t = (k_1 - k_3)^2 \tag{II.2.66b}$$

$$u = (k_1 - k_4)^2 . \tag{II.2.66c}$$

These are Lorentz invariants, and fully encode the kinematics of $2 \to 2$ scattering. Of these, the most important are the center-of-mass energy-squared s and momentum transfer squared t. It is important to note that

$$s + t + u = m_1 + m_2 + m_3 + m_4, \tag{II.2.67}$$

which can be easily verified. We saw in Eq. II.2.63 that the mass of a tachyon with string parameter α' is $m = -\frac{4}{\alpha'}$, so for tachyon scattering we have

$$s + t + u = -\frac{16}{\alpha'}. \tag{II.2.68}$$

We are now in a position to compute the scattering amplitude.

As in standard perturbation theory, we can formulate the scattering amplitude as a power series in the coupling constant. In string perturbation theory, the k-th term in this sum is given as an integral over each vertex z_i over a surface of genus k, or equivalently Euler characteristic $\chi = 2 - 2j$. Thus the tree level amplitude stems from integrating the vertices over a complex surface of genus 0, i.e. the Riemann sphere. However, the sphere is homeomorphic to the complex plane by the well-known stereographic projection map [78], so we can take each integration to be over $\mathbb{C}$ itself. We will correspondingly take $z_j = x_j + iy_j \in \mathbb{C}$, and take the integration measure $d^2 z_j = 2 dx_j dy_j$. Then the amplitude T_4 is given by

$$T_4 = g_s^2 \delta^{26} (k_1 + k_2 + k_3 + k_4) V_4, \tag{II.2.69}$$

where g_s is the string coupling and V_4 is the four-point closed string vertex operator, itself given by

$$V_4 \sim \int_{\mathbb{C}} d^2 z_1 d^2 z_2 d^2 z_3 d^2 z_4 \prod_{j<k}^4 |z_j - z_k|^{\alpha' k_j \cdot k_k} . \tag{II.2.70}$$

We are primarily concerned with V_4, and will focus on simplifying it. The above procedure of mapping from the sphere to $\mathbb{C}$ is not unique; there is a residual symmetry under simultaneous transformation of the z_i. This symmetry takes the form of invariance under the action of a Mobius transformation, and allows us to simultaneously assign three of the z_i to 0, 1, and ∞, respectively. We will take $z_1 \to 0$, $z_2 \to 1$, $z_3 \to \infty$, so that only z_4 is free to be integrated over. Then the amplitude simplifies considerably:

$$V_4 \sim \int_{\mathbb{C}} d^2 z_4 \, |z_4|^{\alpha' k_1 k_4} \, |1 - z_4|^{\alpha' k_2 k_4} . \tag{II.2.71}$$

With the use of Eq. II.2.68, this integral can be performed explicitly to obtain the amplitude in terms of gamma functions. We will not reproduce the calculation, which can be found in almost any elementary string theory text, here, but will merely quote the result:

$$V_4 \sim \frac{\Gamma\left(-1 - \alpha's/4\right)\Gamma\left(-1 - \alpha't/4\right)\Gamma\left(-1 - \alpha'u/4\right)}{\Gamma\left(2 + \alpha's/4\right)\Gamma\left(2 + \alpha't/4\right)\Gamma\left(2 + \alpha'u/4\right)}. \tag{II.2.72}$$

The form of this amplitude, and in particular its singularity structure, has profound consequences for string scattering. It is well-known that $\Gamma(x)$ diverges iff x is a negative integer or zero. Then V_4 has singularities in s at an infinite number of values s_n^∞ given by

$$s_n^\infty = \frac{4 - 4n}{\alpha'}, \ n = 0, 1, 2, \ldots \tag{II.2.73}$$

Recall from Eq. II.2.65 that these are exactly the squares of the masses of excited states of closed strings. Hence we can conceive of this scattering as a sum over all excited string states of s-channel single-string exchanges. However, because the amplitude is symmetric in s and t (and also in the less important u), we can in exactly the same way conceive of this scattering as a tower of t- or u-channel exchanges; in these channels, we again have infinite towers of poles given by

$$t_n^\infty = u_n^\infty = \frac{4 - 4n}{\alpha'}, \ n = 0, 1, 2, \ldots \tag{II.2.74}$$

This duality in scattering mechanism is the origin of the original name for string theory, the so-called "dual-resonance model", and was a driving factor in the initial study of string theory as a model for the strong interaction.

There is an interesting kinematical limit to discuss, the so-called near-forward limit in which $s \to \infty$ while t remains small and fixed; because at high s the scattering angle $\theta \sim \frac{t}{s}$, this limit corresponds to small-angle scattering. In this limit, the amplitude is given approximately by

$$T_4 \sim \Gamma\left[-\alpha(t)\right)\left[(-s)^{\alpha(t)} + (-u)^{\alpha(t)}\right], \tag{II.2.75}$$

where

$$\alpha(t) = \alpha_0(t) + \frac{\alpha'}{4}t \tag{II.2.76}$$

is the Regge trajectory; in flat space, the Regge intercept $\alpha_0 = 2$.

For what follows it will be useful to write Eq. II.2.75 strictly in terms of s. BY Eq. II.2.68 we have

$$u = -\frac{16}{\alpha'} - t - s \sim -s \tag{II.2.77}$$

so that

$$V_4 \sim (-s)^{\alpha(t)} + (s)^{\alpha(t)}. \tag{II.2.78}$$

In the forward limit, the singularities in negative u become singularities in positive, real u. To avoid these singularities in the $s \to \infty$, we give s a small imaginary part. This procedure induces an effective branch cut in s along the positive real axis.

This concludes our discussion of the Virasoro-Shapiro amplitude. Because the method we employed to analyze this scattering process is more important to what follows than the details of the result, we will summarize it briefly here. We begin by parameterizing the kinematics of the scattering in terms of Lorentz invariants; for this example it sufficed to consider the classical Mandelstam variables, but in the more complicated processes studied below we will need to construct generalized Mandelstam invariants. We then wrote down an explicit form of the scattering amplitude, including the vertex operator, in terms of these invariants and the string parameter α'. Lastly, we will take the $s \to \infty$ limit (or, for more complicated amplitudes, a similarly structured limit) to simplify the amplitude into a useful form. This is the method we will employ in all further studies.

II.2.3   The Inclusive Single-String Production Cross Section in Flat Space

Here we will compute the inclusive single-string production cross section in flat space. This is the physical quantity of interest; if string theory is to be an accurate model of quantum chromodynamical processes, its prediction for this cross section should agree at least qualitatively with the result in traditional gauge theory calculations. We will see, however, that the two results are fundamentally incompatible, and so we will be driven to consider string theory in curved space.

Our approach will echo the discussion in Section 1. We will consider the six-point amplitude for $3 \to 3$ scattering, and compute its discontinuity to find the cross section. First, we will in Section II.2.3.1 justify this method through a discussion the optical theorem used in [70].

II.2.3.1   Optical Theorems

In this thesis, we are interested in computing an inclusive cross section. In general, such calculations are nontrivial; there exist, however, several profound identities that facilitate these computations. In particular, there exists a series so-called optical theorems relating inclusive cross sections to scattering amplitudes in certain kinematic regimes.

The first optical theorem is the most-well known, and is frequently referred to as *the* optical theorem. It pertains to the total two-particle cross section for the process $ab \to X$, and indicates that this cross section can be viewed as the imaginary part of the $2 \to 2$ cross section evaluated at the forward limit, $t = 0$, where here t is the same momentum-transfer invariant defined above [79]:

$$\sigma_{2\to2} \sim \frac{1}{s} \operatorname{Im} T_4 \big|_{t=0}. \tag{II.2.79}$$

Being essentially a consequence of unitarity, Eq. II.2.79 is always true, but it is not always useful. Consider, for instance, the scattering of two closed-string tachyons. The optical theorem indicates that this has a total cross section given by the imaginary part of the $2 \to 2$ tachyon scattering amplitude, i.e. the Virasoro amplitude Eq. II.2.72. For generic s, it can be quite difficult to evaluate the imaginary part of this amplitude. In the forward limit, however, the amplitude takes the simple form given in Eq. II.2.78, albeit with a branch cut in s. Consider two points in the complex s-plane, $s_1 = |s_1|e^{i\delta}$ and its complex conjugate $s_2\bar{s}_1 = |s_1|e^{-i\delta}$, where we take $\delta \ll 1$. Then $\operatorname{Im} T_4(s_1) = -\operatorname{Im} T_4(s_2)$ so that the discontinuity $\operatorname{Disc}_s T_4$ of T_4 in s at s_1 is

$$\operatorname{Disc}_s T_4\big|_{s_1} = \operatorname{Im} T_4(s_1) - \operatorname{Im} T_4(s_2) = 2\operatorname{Im} T_4(s_1). \tag{II.2.80}$$

In this way, we can conceive of the imaginary part of the amplitude as given approximately as its discontinuity across a suitably defined branch cut. This "smoothing" of the amplitude in the limit

of infinite-center-of-mass energy is extremely characteristic of string theory, and allows the optical theorems to be at least in principle useful in many situations.

Our goal, then, is to take advantage of this "smoothing" to calculate the inclusive single-particle production cross section in the limit of infinite center-of-mass energy. The analogy to Eq. II.2.79 for single-particle production relates the cross section to the amplitude of $3 \rightarrow 3$ scattering. The theorem is schematically depicted in Figure II.2.2, and quantitatively has the form [70]

$$\frac{d^3\sigma_{ab\to cX}}{d\mathbf{p}_c^3} \sim \frac{1}{s}\operatorname{Disc}_{M^2} T_6. \tag{II.2.81}$$

This is the central result we will use to compute the inclusive single-particle production cross section; we will effectively be analyzing the six-point amplitude instead of the four-point amplitude. Additionally, we will need to work in the limit of infinite center-of-mass energy; this limit will be discussed below, and enables us to write the discontinuity of the amplitude in a convenient form.
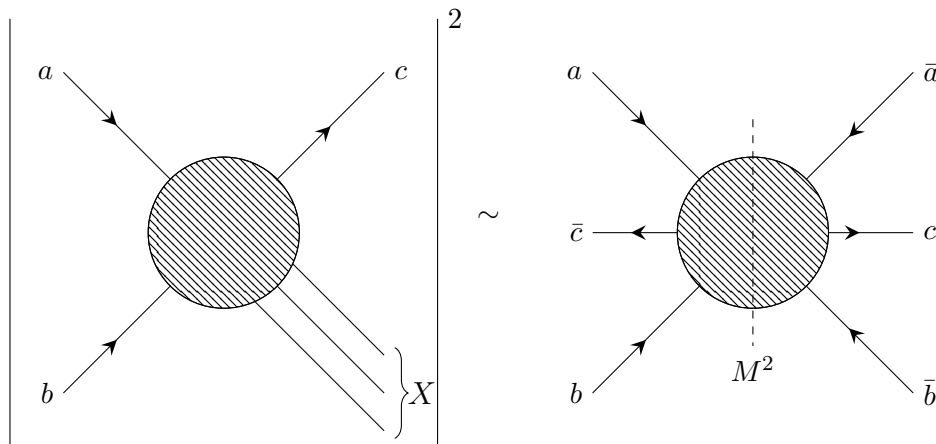

Figure II.2.2: A schematic representation of the generalized optical theorem given in Eq. II.2.81.

II.2.3.2   The Six-Point String Amplitude

We consider $3 \rightarrow 3$ scattering of the form $ab\bar{c} \rightarrow \bar{a}\bar{b}c$, with the intention of computing a six-point amplitude from which we can find the inclusive single-particle production cross section. The kinematics of $3 \rightarrow 3$ scattering are shown in Figure II.2.3. We will consider the case when all external lines are scalar glueballs; however, a similar discussion holds some or all of the external lines are hadrons [66]. The internal lines are pomerons with Regge trajectory $\alpha(t_i) = \alpha_0 + \frac{\alpha'}{4}t_i$. Here, we will take all strings to be open for simplicity; it was shown in [80] that entirely similar results hold for closed-string scattering. Because we do use open strings, however, some modification will be needed when we reuse the results of this section in the closed string scattering of Section 4. In particular, our final result will involve the quantity α', the Regge slope. However, this is the Regge slope of *open* strings, properly denoted α'_{open}; the appropriate Regge slope for closed strings, α'_{closed}, is given by

$$\alpha'_{\text{closed}} = \frac{1}{2}\alpha'_{\text{open}}, \tag{II.2.82}$$

so to translate our results for use in closed string scattering we will need to substitute

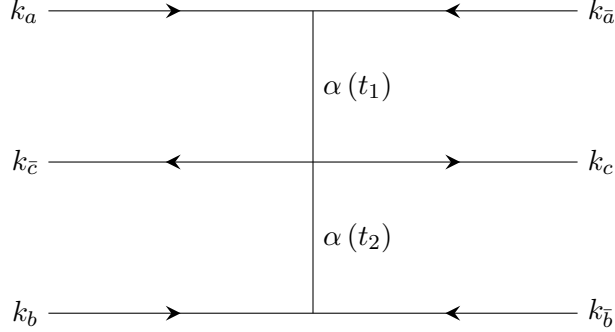$$\alpha' \to \frac{1}{2}\alpha'. \tag{II.2.83}$$

Figure II.2.3: Schematic representation of 3→3 scattering of strings.

To encode the kinematics of this process, we construct generalized Mandelstam invariants [66]:

$$s = (k_a + k_b)^2 \tag{II.2.84a}$$
$$s_1 = (k_a + k_{\bar{c}})^2 \tag{II.2.84b}$$
$$s_2 = (k_b + k_{\bar{c}})^2 \tag{II.2.84c}$$
$$s_3 = (k_{\bar{a}} + k_c)^2 \tag{II.2.84d}$$
$$s_4 = (k_{\bar{b}} + k_c)^2 \tag{II.2.84e}$$
$$t_1 = (k_a - k_{\bar{a}})^2 \tag{II.2.84f}$$
$$t_2 = (k_b - k_{\bar{b}})^2 \tag{II.2.84g}$$
$$\Sigma_1 = (k_a + k_{\bar{a}} + k_{\bar{c}})^2 \tag{II.2.84h}$$
$$\Sigma_2 = (k_b + k_{\bar{b}} + k_{\bar{c}})^2. \tag{II.2.84i}$$

We also define the energy ratio

$$\kappa = \frac{s_1 s_2}{s}. \tag{II.2.85}$$

These are labelled in analogy with the traditional Mandelstam variables. In particular, s is the center of mass energy, the s_i are partial energies, and the t_i are the momentum transfers. We are in particular interested in the so-called double diffractive limit [66, 70], also known as the double Regge limit. In this limit, the energies $s, s_1, s_2 \to \infty$ with $s \gg s_1, s_2$ so that the ratio κ remains fixed; we will later take $\kappa \to \infty$ to obtain the cross section. We also demand that the t_i are fixed and constant. Physically, this corresponds to fixed angle scattering, in which the incoming particles are deflected only slightly from their initial trajectories [66]. We note briefly that in this limit the kinematics of the produced particle c are described by κ:

$$\kappa \equiv p_{\mathrm{T},\,c}^2 + m_c^2, \tag{II.2.86}$$

52

where $p_{\text{T}, c}$ is the spatial momentum of c in directions transverse to the collision.

In the region of phase space of interest to our calculation, the amplitude for this $3 \to 3$ scattering is given by [70]

$$T_6^{\text{flat}} = g_0 \, (s_1)^{\alpha(t_1)} \, \kappa^{-2} V_6 \left(\Sigma_1, \Sigma_2, t_1, t_2, \kappa \right) (s_2)^{\alpha(t_2)} \, g_0, \tag{II.2.87}$$

where the two-pomeron-to-two-glueball vertex operator V_6 is given in terms of the two-pomeron-to-one-glueball vertex operator V_5 as

$$V_6(\Sigma_1, \Sigma_2, t_1, t_2, \kappa) \sim \int_0^1 dz \; z^{-\Sigma_2 - 1} \left(1 - z \right)^{-\Sigma_1 - 1} V_5 \left(\alpha\left(t_1\right), \alpha\left(t_2\right), \underbrace{\frac{\kappa}{z\left(1 - z\right)}}_{\equiv x} \right). \tag{II.2.88}$$

To take advantage of the optical theorem, we must compute the discontinuity of T_6^{flat} in the missing mass M^2, i.e. in the center-of-mass energy s. However, from Eq. II.2.87 we see that all of the s dependence of T_6^{flat}, and hence of its discontinuity, enters through the s-dependence of κ. Thus we can use the optical theorem by calculating the discontinuity of T_6^{flat} in κ. Now, the only (possibly) discontinuous term in this expression for T_6^{flat} is V_6, and hence the κ-dependence of the discontinuity in T_6^{flat} is given by

$$\text{Disc}_{M^2} T_6^{\text{flat}} = \kappa^{-2} \, \text{Disc}_{M^2} V_6. \tag{II.2.89}$$

Meanwhile, the only discontinuity in V_6 stems from the κ-discontinuity of V_5, so we must have

$$\text{Disc}_{M^2} V_6 \sim \int_0^1 dz \; z^{-\Sigma_2 - 1} \left(1 - z \right)^{-\Sigma_1 - 1} \left[\text{Disc}_x V_5 \left(\alpha\left(t_1\right), \alpha\left(t_2\right), x \right) \right]. \tag{II.2.90}$$

To evaluate this discontinuity, we must examine in detail the behavior of $V_5(\alpha\left(t_1\right), \alpha\left(t_2\right), x)$, which is discussed in Section II.2.3.3.

II.2.3.3 The Five-Point String Amplitude and Its Discontinuities

First we will describe the kinematics of $2 \to 3$ scattering of the form $ab \to \bar{a}\bar{b}c$, depicted pictorially in Figure II.2.4.
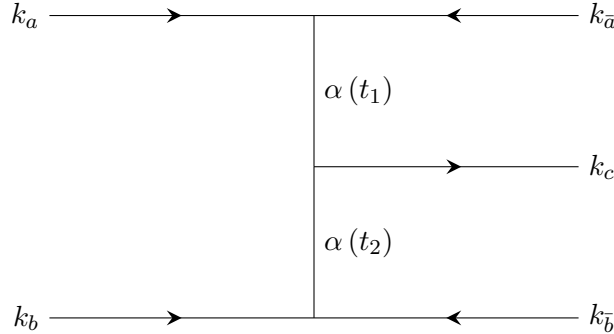

Figure II.2.4: Schematic representation of $2 \to 3$ scattering of strings.

As before, we take all external lines to be scalar glueballs, and all internal lines to be pomerons. We define generalized Mandelstam invariants to parameterize the process:

$$s = (k_a + k_b)^2 \tag{II.2.91a}$$

$$s_1 = (k_c + k_{\bar{a}})^2 \tag{II.2.91b}$$

$$s_2 = (k_c + k_{\bar{b}})^2 \tag{II.2.91c}$$

$$t_1 = (k_{\bar{a}} - k_a)^2 \tag{II.2.91d}$$

$$t_2 = (k_{\bar{b}} - k_b)^2 . \tag{II.2.91e}$$

We also again define the energy ratio

$$\kappa = \frac{s_1 s_2}{s}. \tag{II.2.92}$$

We will again work in the double Regge limit. In terms of channel invariants $s_1, s_2, t_1, t_2, \kappa$, the five point amplitude is (up to a constant)

$$T_5(s_1, s_2, t_1, t_2, \kappa) \sim (-s_1)^{\alpha(t_1)} (-s_2)^{\alpha(t_2)} V_5 (\alpha(t_1), \alpha(t_2), \kappa), \tag{II.2.93}$$

where α is the Regge trajectory and the vertex operator V_5 is given by [81, 82]

$$V_5 (\alpha(t_1), \alpha(t_2), \kappa) = \int_0^\infty dx_1 \int_0^\infty dx_2 \; x_1^{-\alpha(t_1)-1} x_2^{-\alpha(t_2)-1} e^{-x_1 - x_2 + x_1 x_2/(\alpha'\kappa)}. \tag{II.2.94}$$

We will begin to analyze this amplitude by studying $V_5 (\alpha(t_1), \alpha(t_2), \kappa)$ in the limit $\kappa \to \infty$. Recall the identity

$$\int_0^\infty du \; u^n e^{-au} = \frac{\Gamma(n+1)}{a^{n+1}}, \tag{II.2.95}$$

found by repeated application of integration by parts. Immediately, we see that, as $\kappa \to \infty$,

$$
\begin{aligned}
V_5 (\alpha(t_1), \alpha(t_2), \infty) &\equiv \lim_{\kappa \to \infty} V_5 (\alpha(t_1), \alpha(t_2), \kappa) \\
&= \lim_{\kappa \to \infty} \int_0^\infty dx_1 \int_0^\infty dx_2 \; x_1^{-\alpha(t_1)-1} x_2^{-\alpha(t_2)-1} e^{-x_1 - x_2 + x_1 x_2/(\alpha'\kappa)} \\
&= \int_0^\infty dx_1 \int_0^\infty dx_2 \; x_1^{-\alpha(t_1)-1} x_2^{-\alpha(t_2)-1} e^{-x_1 - x_2} \\
&= \left[\int_0^\infty dx_1 \; x_1^{-\alpha(t_1)-1} e^{-x_1} \right] \left[\int_0^\infty dx_2 \; x_2^{-\alpha(t_2)-1} e^{-x_2} \right] \\
&= \Gamma(-\alpha(t_1)) \Gamma(-\alpha(t_2)) .
\end{aligned}
\tag{II.2.96}
$$

Importantly, $V_5 (\alpha(t_1), \alpha(t_2), \infty)$ is real and finite. For more general κ, the situation is some-

what more complicated:

$$
\begin{aligned}
V_5\left(\alpha\left(t_1\right),\alpha\left(t_2\right),\kappa\right) &= \int_0^\infty dx_1 \int_0^\infty dx_2 \; x_1^{-\alpha(t_1)-1} x_2^{-\alpha(t_2)-1} e^{-x_1-x_2+x_1 x_2/(\alpha'\kappa)} \\
&= \int_0^\infty dx_1 \; x_1^{-\alpha(t_1)-1} e^{-x_1} \int_0^\infty x_2^{-\alpha(t_2)-1} e^{-x_2(1-x_1/\alpha'\kappa)} \\
&= \int_0^\infty dx_1 x_1^{-\alpha(t_1)-1} e^{-x_1} \left[\frac{\Gamma\left(-\alpha\left(t_2\right)\right)}{\left(1-\frac{x_1}{\alpha'\kappa}\right)^{-\alpha(t_2)}} \right] \\
&= \Gamma\left(-\alpha\left(t_2\right)\right) \int_0^\infty dx_1 x_1^{-\alpha(t_1)-1} e^{-x_1} \left(1-\frac{x_1}{\alpha'\kappa}\right)^{\alpha(t_2)}. \quad\text{(II.2.97)}
\end{aligned}
$$

It is tempting here to express $\left(1-\frac{x_1}{\alpha'\kappa}\right)^{\alpha(t_2)}$ (where $\alpha\left(t_2\right)$ is not in general an integer) as an infinite sum using the generalized binomial theorem and integrate term-by-term over the sum, but this does not in general converge. Instead, we must examine this more closely. Here we are primarily interested in the κ-dependency of the amplitude; for different values of κ, vastly different behavior is observed. Whereas for $x < \alpha'\kappa$, $\left(1-\frac{x_1}{\alpha'\kappa}\right)^{\alpha(t_2)}$ is real, for $x > \alpha'\kappa$, it is in general complex. It is natural, then, to split this integral into two:

$$
\begin{aligned}
V_5\left(\alpha\left(t_1\right),\alpha\left(t_2\right),\kappa\right) &= \Gamma\left(-\alpha\left(t_2\right)\right) \int_0^\infty dx_1 x_1^{-\alpha(t_1)-1} e^{-x_1} \left(1-\frac{x_1}{\alpha'\kappa}\right)^{\alpha(t_2)} \\
&= \Gamma\left(-\alpha\left(t_2\right)\right) \left[\underbrace{\int_0^{\alpha'\kappa} dx_1 x_1^{-\alpha(t_1)-1} e^{-x_1} \left(1-\frac{x_1}{\alpha'\kappa}\right)^{\alpha(t_2)}}_{\equiv \Gamma(-\alpha(t_2))^{-1} f_1(\kappa,\alpha(t_1),\alpha(t_2))} \right. \\
&\quad \left. + \underbrace{\int_{\alpha'\kappa}^\infty dx_1 x_1^{-\alpha(t_1)-1} e^{-x_1} \left(1-\frac{x_1}{\alpha'\kappa}\right)^{\alpha(t_2)}}_{\equiv \Gamma(-\alpha(t_2))^{-1} f_2(\kappa,\alpha(t_1),\alpha(t_2))} \right]. \quad\text{(II.2.98)}
\end{aligned}
$$

Because f_1 is everywhere real, the imaginary part of V_5 can be obtained entirely from f_2:

$$
\begin{aligned}
f_2(\kappa) &= \Gamma\left(-\alpha\left(t_2\right)\right) \int_{\alpha'\kappa}^\infty dx_1 x_1^{-\alpha(t_1)-1} e^{-x_1} \left(1-\frac{x_1}{\alpha'\kappa}\right)^{\alpha(t_2)} \\
&= \Gamma\left(-\alpha\left(t_2\right)\right) \int_{\alpha'\kappa}^\infty dx_1 x_1^{-\alpha(t_1)-1} e^{-x_1} \left[\left(e^{i\pi}\right)\left(\frac{x_1}{\alpha'\kappa}-1\right)\right]^{\alpha(t_2)} \\
&= e^{i\pi\alpha(t_2)}\Gamma\left(-\alpha\left(t_2\right)\right) \int_{\alpha'\kappa}^\infty dx_1 x_1^{-\alpha(t_1)-1} e^{-x_1} \left(\frac{x_1}{\alpha'\kappa}-1\right)^{\alpha(t_2)} \quad\text{(II.2.99)}
\end{aligned}
$$

so that

$$
I(\kappa) \equiv \mathrm{Im}(V_5) = \sin\pi\alpha\left(t_2\right)\Gamma\left(-\alpha\left(t_2\right)\right) \int_{\alpha'\kappa}^\infty dx_1 x_1^{-\alpha(t_1)-1} e^{-x_1} \left(\frac{x_1}{\alpha'\kappa}-1\right)^{\alpha(t_2)}. \quad\text{(II.2.100)}
$$

We saw earlier that V_5 is asymptotically real as $\kappa \to \infty$, so it is reasonable to check that $\lim_{\kappa\to\infty} I(\kappa) = 0$. We proceed straightforwardly albeit through a roundabout series of substitutions $(u = (\alpha'\kappa)^{-1}x_1;\; \bar{u} = u - 1; v = \kappa\bar{u})$:

$$I(\kappa) = \sin \pi \alpha\,(t_2)\Gamma\left(-\alpha\,(t_2)\right) \int_{\alpha'\kappa}^{\infty} dx_1 x_1^{-\alpha(t_1)-1} e^{-x_1} \left(\frac{x_1}{\alpha'\kappa} - 1\right)^{\alpha(t_2)}$$

$$= (\alpha'\kappa)^{-\alpha(t_1)} \sin \pi \alpha\,(t_2)\Gamma\left(-\alpha\,(t_2)\right) \int_{1}^{\infty} du\ u^{-\alpha(t_1)-1} e^{-\kappa u} (u-1)^{\alpha(t_2)}$$

$$= (\alpha'\kappa)^{-\alpha(t_1)} \sin \pi \alpha\,(t_2)\Gamma\left(-\alpha\,(t_2)\right) \int_{0}^{\infty} d\bar{u}\, (1+\bar{u})^{-\alpha(t_1)-1} e^{-\kappa(1+\bar{u})} \bar{u}^{\alpha(t_2)}$$

$$= (\alpha'\kappa)^{-1-\alpha(t_1)-\alpha(t_2)} e^{-\kappa} \sin \pi \alpha\,(t_2)\Gamma\left(-\alpha\,(t_2)\right) \int_{0}^{\infty} dv\ \left(1 + \frac{v}{\alpha'\kappa}\right)^{-\alpha(t_1)-1} e^{-v} v^{\alpha(t_2)} \quad \text{(II.2.101)}$$

This is quite general; we have never explicity taken $\kappa \to \infty$. In this limit, $I(\kappa)$ simplifies considerably:

$$\lim_{\kappa\to\infty} I(\kappa) = \alpha'\kappa^{-1-\alpha(t_1)-\alpha(t_2)} e^{-\alpha'\kappa} \sin \pi \alpha\,(t_2)\Gamma\left(-\alpha\,(t_2)\right) \int_{0}^{\infty} dv\ \left(1 + \frac{v}{\alpha'\kappa}\right)^{-\alpha(t_1)-1} e^{-v} v^{\alpha(t_2)}$$

$$\approx \alpha'\kappa^{-1-\alpha(t_1)-\alpha(t_2)} e^{-\alpha'\kappa} \sin \pi \alpha\,(t_2)\Gamma\left(-\alpha\,(t_2)\right) \int_{0}^{\infty} dv\ e^{-v} v^{\alpha(t_2)}$$

$$= \alpha'\kappa^{-1-\alpha(t_1)-\alpha(t_2)} e^{-\alpha'\kappa} \sin \pi \alpha\,(t_2)\Gamma\left(-\alpha\,(t_2)\right) \Gamma\left(\alpha\,(t_2)+1\right)$$

$$= -\pi \alpha'\kappa^{-1-\alpha(t_1)-\alpha(t_2)} e^{-\alpha'\kappa}, \quad \text{(II.2.102)}$$

where we have taken $\frac{v}{\alpha'\kappa} \to 0$ as $\kappa \to \infty$; in the last step we have made use of the identity

$$\Gamma(x)\Gamma(1-x) = \frac{\pi}{\sin(\pi x)}. \quad \text{(II.2.103)}$$

We hence confirm what we have seen above: as $\kappa \to \infty$, $I(\kappa)$ vanishes exponentially quickly in κ. This will be essential to what follows.

II.2.3.4   The Discontinuity in the Six-Point Function and The Inclusive Cross Section

Having computed the discontinuity in V_5, we are ready to evaluate the discontinuity in V_6. For fixed t_1, t_2, $V_5(\alpha\,(t_1), \alpha\,(t_2), x)$ converges iff $x < 0$; in particular, $V_5(\alpha\,(t_1), \alpha\,(t_2), x)$ is infinite for all $x > 0$. If we allow x to be complex, we can evaluate directly the discontinuity in V_5 about the real-κ axis by examining $\lim_{\varepsilon \to 0} V_5(\alpha\,(t_1), \alpha\,(t_2), x + i\varepsilon)$ and $\lim_{\varepsilon \to 0} V_5(\alpha\,(t_1), \alpha\,(t_2), x - i\varepsilon)$. From Eq. 3.6, we see that, whereas $\lim_{\varepsilon \to 0} \text{Re } V_5(\alpha\,(t_1), \alpha\,(t_2), x + i\varepsilon) = \lim_{\varepsilon \to 0} \text{Re } V_5(\alpha\,(t_1), \alpha\,(t_2), x - i\varepsilon)$, $\lim_{\varepsilon \to 0} \text{Im } V_5(\alpha\,(t_1), \alpha\,(t_2), x + i\varepsilon) \neq \lim_{\varepsilon \to 0} \text{Im } V_5(\alpha\,(t_1), \alpha\,(t_2), x - i\varepsilon)$. Thus the discontinuity in V_5 across x is given approximately by (the absolute value of) its imaginary part:

$$\text{Disc}_x V_5(\alpha\,(t_1), \alpha\,(t_2), x) \sim \left|\text{Im } V_5(\alpha\,(t_1), \alpha\,(t_2), x)\right|. \quad \text{(II.2.104)}$$

We saw above that

$$\left|\text{Im } V_5(\alpha\,(t_1), \alpha\,(t_2), x)\right| = \alpha'x^{-1-\alpha(t_1)-\alpha(t_2)} e^{-\alpha'x} \sin \pi \alpha\,(t_2)\Gamma\left(-\alpha\,(t_2)\right) \int_{0}^{\infty} dv\ \left(1 + \frac{v}{\alpha'x}\right)^{-\alpha(t_1)-1} e^{-v} v^{\alpha(t_2)},$$
$$\text{(II.2.105)}$$

or, in the limit $x \to \infty$,

$$\left| \mathrm{Im}\ V_5 \left(\alpha\left(t_1 \right), \alpha\left(t_2 \right), x \right) \right| = \pi \alpha' x^{-1-\alpha(t_1)-\alpha(t_2)} e^{-\alpha' x}. \tag{II.2.106}$$

Thus, in this limit, the inclusive cross section is given by

$$\mathrm{Disc}_{M^2}\ V_6 = \pi \int_0^1 dz\ z^{-\Sigma_2-1} \left(1-z \right)^{-\Sigma_1-1} \left[\left(\frac{\alpha' \kappa}{z\left(1-z\right)} \right)^{-1-\alpha(t_1)-\alpha(t_2)} \exp\left(-\frac{\alpha' \kappa}{z\left(1-z\right)} \right) \right]. \tag{II.2.107}$$

This simplifies considerably; because of the $\left[z\left(1-z\right) \right]^{-1-\alpha(t_1)-\alpha(t_2)}$ term, the integrand is sharply peaked about $z = \frac{1}{2}$, and we can approximate

$$\mathrm{Disc}_{M^2}\ V_6 \sim \pi \left[\left(4\alpha' \kappa \right)^{-1-\alpha(t_1)-\alpha(t_2)} e^{-4\alpha' \kappa} \right]. \tag{II.2.108}$$

Then by Eq. II.2.89, we have

$$\mathrm{Disc}_{M^2}\ T_6^{\mathrm{flat}} \sim \kappa^{-2}\, \mathrm{Disc}_{M^2}\ V_6 \sim 16\pi \left[\left(4\alpha' \kappa \right)^{-3-\alpha(t_1)-\alpha(t_2)} e^{-4\alpha' \kappa} \right]. \tag{II.2.109}$$

This is the central result in flat space string theory. We see that, in the double Regge limit, the inclusive particle cross section decays exponentially quickly in κ. This stands in stark contrast to the result from QCD, in which the decay is only polynomial. Historically, this discrepancy was an important contribution to the abandonment of flat-space string theory as a model for the strong interaction.

II.3   AdS/CFT Correspondence and Curved Space String Theory

In this section we review some of the developments that suggest that curved space string theory might alleviate the discrepancy between the predictions of string theory, derived in Section II.2.3.4, and QCD. In particular, we give a brief introduction to the AdS/CFT Correspondence and conclude with a discussion of the results of [64], the first paper to demonstrate that curved space string theory can describe QCD processes.

II.3.1   The AdS/CFT Correspondence: A Brief Discussion

The AdS/CFT correspondence is a conjectured equivalence between semiclassical gravity in $d+1$-dimensional Anti de-Sitter (AdS) space and a conformal field theory (CFT) defined on the d-dimensional boundary of AdS space. The correspondence was suggested by Maldacena in 1997 [58], and since then has inspired thousands of papers, becoming one of the most vibrant research topics in high energy theory. It has never been proven to be true, however; all evidence supporting the conjecture is circumstantial. We will discuss here the two physical theories linked by AdS/CFT correspondence, and then illustrate why they are believed to be linked. The literature on these topics is vastly too large to be summarized here, and so our goal here is only to provide a brief introduction to the aspects to the correspondence that will be most useful to us later on.

II.3.1.1 Anti de Sitter Space

Anti-de Sitter space is a vacuum solution to the D-dimensional Einstein field equations

$$R_{\mu\nu} - \frac{1}{2}Rg_{\mu\nu} + \Lambda g_{\mu\nu} = 0 \qquad (\text{II.3.1})$$

with negative cosmological constant Λ, where $R_{\mu\nu}$ is the Ricci tensor and R is the Ricci scalar. For $D = 5$, the AdS metric takes the familiar form

$$ds^2_{AdS_5} = \frac{r^2}{R^2}\eta_{\mu\nu}dx^\mu dx^\nu - \frac{R^2}{r^2}dr^2, \qquad (\text{II.3.2})$$

where here $\eta_{\mu\nu}$ is the four-dimensional Minkowski metric, the x^μ are three-plus-one dimensional coordinates, and R is the AdS radius, a length scale characteristic of the solution.

The AdS/CFT correspondence involves type II supergravity in an AdS background [58, 77]; however, type II supergravity, like all traditional superstring theories, requires ten dimensions of spacetime. Thus to arrive at a suitable metric for the AdS/CFT correspondence, we multiply five-dimensional AdS space with a compact, transverse 5-dimensional space, usually taken to be the five-sphere S^5:

$$ds^2_{AdS/CFT} = \frac{r^2}{R^2}\eta_{\mu\nu}dx^\mu dx^\nu - \frac{R^2}{r^2}dr^2 - R^2 ds^2_{S^5}; \ 0 < r < \infty, \qquad (\text{II.3.3})$$

where $ds^2_{S^5}$ is the metric on the five-sphere.

II.3.1.2 Conformal Field Theories

Although the AdS/CFT correspondence was originally formulated for conformal field theories, these are unsuited to describe QCD, and we will discuss them only briefly. In particular, Maldacena arrived at the correspondence by considering the most famous CFT, the so-called $\mathcal{N} = 4$ supersymmetric Yang-Mills theory (SYM) [58]. This theory has four generations of supersymmetry, the maximum number allowed in four-dimensions, and is defined by the Lagrangian [77]

$$\mathcal{L} = \text{Tr}\left(-\frac{1}{g^2_{YM}}F_{\mu\nu}F^{\mu\nu} + \frac{\vartheta}{16\pi^2}F_{\mu\nu}\tilde{F}^{\mu\nu} - i\bar{\lambda}^a\bar{\sigma}^\mu D_\mu\lambda_a - D_\mu\varphi^i D^\mu\varphi_i \right.$$
$$\left. + g_{YM}C^{ab}_i\lambda_a\left[\varphi^i, \lambda_b\right] + g_{YM}\bar{C}_{iab}\bar{\lambda}^a\left[\varphi^i, \bar{\lambda}^b\right] + \frac{g^2_{YM}}{2}\left[\varphi^i, \varphi^j\right]^2 \right). \qquad (\text{II.3.4})$$

In this Lagrangian, the A_μ are Lorentz vectors, the the λ^a are Weyl fermions, and φ^i are real scalar fields; these are all defined to live in representations of SU(4), and the C^{ab}_i are the Clebsch-Gordan coefficients for this group. We further define the Yang-Mills coupling f_{YM}, the field strength tensor $F_{\mu\nu} = \partial_\mu A_\nu - \partial_\nu A_\mu + i\left[A_\mu, A_\nu\right]$ and its Hodge dual $\tilde{F}_{\mu\nu} = \frac{1}{2}\varepsilon_{\mu\nu\lambda\rho}F^{\lambda\rho}$, and the covariant derivative D_μ. We take this theory to have SU(N) gauge symmetry; note the important difference between the number $\mathcal{N}$ of supersymmetry generations and N the number of colors in the theory.

This Lagrangian contains a rich structure which is entirely unnecessary to provide a reasonable model of QCD. In particular, we will calculate glueball-glueball scattering, so we can neglect these

terms. Additionally, the parameter ϑ describes the CP violation scale of the theory, so it can be set to zero for our purposes. Then the Lagrangian simplifies drastically:

$$\mathcal{L} = -\frac{1}{g_{\mathrm{YM}}^2} \mathrm{Tr} \left(F_{\mu\nu} F^{\mu\nu} - D_\mu \varphi^i D^\mu \varphi_i + \frac{g_{\mathrm{YM}}^2}{2} \left[\varphi^i, \varphi^j \right]^2 \right). \tag{II.3.5}$$

Because it only contains massless fields and the coupling constant g_{YM} is dimensionless, $\mathcal{N} = 4$ SYM is classically scale invariant; moreover, upon quantization the beta function of this theory is believed to vanish order-by-order in perturbation theory, so we expect $\mathcal{N} = 4$ SYM to remain scale invariant quantum mechanically. We will not need any more information about this theory, so in the interest of brevity we will curtail our discussion of it.

II.3.1.3 The Correspondence

Having discussed the basic elements of the AdS/CFT correspondence, we will now explain how to equate the two theories. Maldacena identified the correspondence in [58] essentially by identifying degrees of freedom between the two theories, which he accomplished by embedding the state space of type IIB supergravity inside of the state space of SYM. For our purposes, it suffices to consider the practical details of the correspondence, which consist of a carefully structured series of limits of coupling constants designed to ensure equivalence of results between the two theories. In what follows, we will follow the conventions of [64, 66].

We immediately relate the coupling constants as

$$g_{\mathrm{YM}}^2 = 4\pi g_s, \tag{II.3.6}$$

where g_s is the string coupling. Moreover, we take the number of colors N in the gauge theory to infinity, while keeping the 't Hooft coupling

$$\lambda \equiv g_{\mathrm{YM}}^2 N \tag{II.3.7}$$

fixed but large; this forces g_{YM}, and hence g_s, to be small, and hence limits the importance of string splitting. We relate λ to the AdS radius R and the Regge slope α' by

$$\lambda = \frac{R^4}{\alpha'^2}. \tag{II.3.8}$$

An interesting consequence of this relationship is that the AdS radius R is large; this allows us to treat the AdS geometry classically, and work in supergravity rather than using the full apparatus of superstring theory. These relationships suffice to quantitatively link results between the bulk gravity theory and the boundary gauge theory. This so-called "AdS dictionary" was worked out in [83] soon after the AdS/CFT correspondence was discovered.

We now discuss the kinematics of these holographic theories. It has been observed in many holographic models that the kinematics of four-dimensional processes in higher-dimensional space have a dependence on transverse coordinates [64, 77]. It can be seen that the metric Eq. II.3.3 is invariant under infinitesimal translation in x^μ, so by Noether's theorem there exist conserved four-momenta

$$p_\mu \equiv i\partial_\mu. \tag{II.3.9}$$

Correspondingly, from the metric it is clear that the four-dimensional components $\tilde{p}_\mu$ of the full ten-dimensional momentum measured in a frame localized at some r are related to the four-momentum components by

$$p_\mu = \frac{r}{R}\tilde{p}_\mu, \tag{II.3.10}$$

so that in particular states strongly localized at R, and hence of characteristic ten-dimensional energy $\tilde{p} \sim R^{-1}$, have dual four-dimensional energy

$$p = \frac{r}{R^2}. \tag{II.3.11}$$

Finally, we discuss the dynamics of string scattering in the bulk, which is dual to scattering in the gauge theory. All of the following can be made rigorous through an analysis of the string partition function and generating functionals for gauge theory correlation functions; this discussion can be found in, inter alia, [77, 84] and will not be repeated here. We will instead focus on computational aspects of the AdS/CFT correspondence following the discussion in [77].

In traditional QFTs, computations of amplitudes and other important quantities in scattering theory are facilitated by diagrams, schematic visual representations of the power-series expansion of the generating functional for the field theory. Feynman diagrams are formulated in flat spacetime, and are insufficient to describe string scattering in AdS space. We can, however, utilize an analogue of Feynman diagrams known as Witten diagrams to perform these calculations in curved space. Defined entirely analogously to traditional Feynman diagrams, Witten diagrams are uniquely suited to describe string scattering in curved space. A Witten diagram is shown in Figure II.3.1; we will discuss its interpretation below.
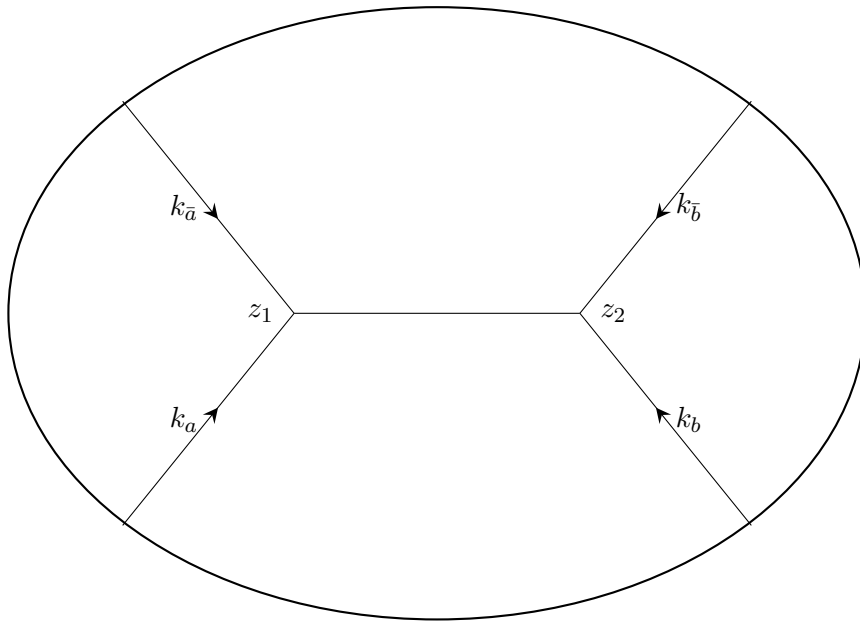

Figure II.3.1: Example of a Witten diagram corresponding to $2 \to 2$ scattering in curved space.

For simplicity, we take all particles in Figure II.3.1 to be scalars with mass-squared m^2 and conformal dimension Δ. The circle surrounding the diagram represents the $d-1$ dimensional

60

boundary of AdS space; this is the surface on which the CFT is defined; the interior of the circle represents the full d-dimensional bulk of AdS. To compute an amplitude from this diagram, we need to define two types of propagators: the boundary-to-bulk propagator and the bulk-to-bulk propagator. The boundary-to-bulk propagator is used for the external strings, and the bulk-to-bulk propagator is used exclusively for internal lines.

To relate the wavefunction φ of a scalar at a point (x, r) in the bulk to the boundary wavefunction $\varphi_\infty(y)$, we can introduce a kernel K_Δ given by

$$\varphi(x, r) = \int_{\partial \text{AdS}} d^{d-1}y K_\Delta(x, r; y) \varphi_\infty(y). \tag{II.3.12}$$

Similarly, to relate the wavefunctions at bulk points (x, r_1) and (y, r_2), we can introduce a Green's function G_Δ given by

$$\left(\Box - m^2\right) G_\Delta(x, r_1; y, r_2) = \frac{\delta^{d-1}(x - y)\delta(r_1 - r_2)}{\sqrt{g}}, \tag{II.3.13}$$

where $\Box$ is the laplacian on AdS space and g is the determinant of the metric. Then, introducing a bulk source function $J(x, r)$, we can write

$$\varphi(x, r_1) = \int_{\text{AdS}} d^{d-1}y dr_2 \sqrt{g} \, G_\Delta(x, r_1; y, r_2) J(y, r_2). \tag{II.3.14}$$

These functions K_Δ and G_Δ are, respectively, the boundary-to-bulk and bulk-to-bulk propagators for a particle of conformal dimension Δ. Explicit representations for these functions can be found in terms of hypergeometric functions, but for our purposes the definitions in Eqs. II.3.12 and II.3.14 are sufficient. Because boundary points can be considered as bulk points at infinite radius, we have

$$K_\Delta(x, r_1; y) \propto \lim_{r_2 \to \infty} G_\Delta(x, r_1; y, r_2), \tag{II.3.15}$$

so we can for the moment focus on G_Δ.

In what follows, it will be convenient to work with the momentum space propagators, i.e. the Fourier transforms of Eqs. II.3.12 and II.3.14. As discussed above, the metric is invariant under translations in the x^μ, so by Lorentz invariance the propagators must be functions only of the difference $x - y$. Then by suitable Poincare transformation we can rewrite the propagators to be functions of only one four-coordinate $x_\perp$. Under this transformation,

$$K_\Delta(x, r; y) \to K_\Delta(x_\perp, r) \tag{II.3.16a}$$

$$G_\Delta(x, r_1; y, r_2) \to G_\Delta(x_\perp, r_1; r_2). \tag{II.3.16b}$$

We can then define the Fourier transforms of these propagators as a function of the momentum q along the $x_\perp$ direction:

$$\tilde{K}_\Delta(r, t) = \int d^{d-1}x e^{-iqx} K_\Delta(x, r) \tag{II.3.17a}$$

$$\tilde{G}_\Delta(r_1, r_2, t) = \int d^{d-1}x e^{-iqx} G_\Delta(x, r_1; r_2), \tag{II.3.17b}$$

61

where we have defined $t = q^2$ after noting that Lorentz invariance ensures that these are only functions of the momentum-squared. It is now convenient to abandon r and instead work with the coordinate $z = \frac{R^2}{r}$; the boundary of AdS space is now found at $z = 0$ so that

$$K_\Delta(z, t) \propto \lim_{z' \to 0} G_\Delta\left(z, z', t\right). \tag{II.3.18}$$

It can can be shown that

$$\tilde{G}_\Delta\left(z, z', t\right) \propto \int_0^\infty dk \, k \frac{J_{\Delta-2}\left(kz\right) J_{\Delta-2}(kz')}{k^2 - t}. \tag{II.3.19}$$

Here, k corresponds to the mass of the propagating particle, and the integral over k indicates that particles of arbitrary mass are allowed in the theory; this is in line with the conformal properties of the boundary theory. By taking the $z' \to 0$ limit, one can show that

$$\tilde{K}_\Delta(z, t) \propto \int_0^\infty dk \frac{k^3 J_{\Delta-2}\left(kz\right)}{k^2 - t}. \tag{II.3.20}$$

With these propagators defined, one can construct from Figure II.3.1 an amplitude in much the same way one would construct an amplitude from a Feynman diagram. The discussion in Section 4 will entail the use of momentum-space propagators analagous to those in Eqs. II.3.19 and II.3.20 to evaluate a Witten diagram to facilitate the calculation of the six-point function in curved-space string theory.

II.3.2   AdS/CFT Without Conformality: the Hard Wall Model

As originally formulated, the AdS/CFT correspondence holds that conformal field theories can be thought of as dual to the dynamics of strings in ten dimensional AdS space with metric given in Eq. II.3.3. However, string theory in this space has a characteristic conformal symmetry that is not found in QCD. Although at high energies QCD is nearly conformal, in general QCD can not be well approximated as conformal, and so we do not expect results for strings in such a space to accurately model QCD dynamics; in particular, conformal field theories feature neither confinement nor mass gaps in the glueball spectrum, both of which are important characteristics of QCD. Instead, we must break the conformality of the metric 2.1 in such a way that it is dual to confining theories with mass gap. In has been shown that this can be done straightforwardly, by simply imposing a lower limit r_{min} on r, i.e. working in the metric

$$ds^2 = \frac{r^2}{R^2} \eta_{\mu\nu} dx^\mu dx^\nu - \frac{R^2}{r^2} dr^2 - R^2 ds_{S^5}^2; \; r_{min} < r < \infty, \tag{II.3.21}$$

known as the hard wall metric [64, 66, 77]. The numerical value of r_{min} is closely related to the mass gap scale of the dual field theory, in a way that can be read off clearly from the holographic dynamics in the sawn-off AdS space. Hence, for the hard wall metric to correspond to a four dimensional mass gap scale Λ, the discussion of Section II.3.1.3 indicates that we must have

$$r_{min} = R^2 \Lambda. \tag{II.3.22}$$

It can be argued that the presence of this mass gap demonstrates that the gauge theory dual to this gravity model is confining [77].

As we saw above, it is convenient to replace the AdS radial coordinate with its normalized inverse

$$z \equiv \frac{R^2}{r}. \tag{II.3.23}$$

In terms of z, the hard wall metric is

$$ds^2 = \frac{R^2}{z^2} \left(\eta_{\mu\nu} dx^\mu dx^\nu - dz^2 \right) - R^2 ds_{S^5}^2; \ 0 < z < z_{max}, \tag{II.3.24}$$

where

$$z_{max} = \frac{1}{\Lambda}, \tag{II.3.25}$$

and the holographic momenta are

$$\tilde{p} = \frac{z}{R} p. \tag{II.3.26}$$

II.3.2.1 Propagators in the Hard Wall Model

The propagators derived in Sec. II.3.1.3 have dynamics dual to those of a conformal field theory, and hence are unsuited for use in the hard wall model, in which the gravity dual is instead a confining field theory. In particular, whereas the propagators II.3.19 and II.3.20 correspond to the propagation of particles of arbitrary mass, only particles with discrete masses are allowed in a confining field theory. To arrive at propagators satisfying this discrete mass condition, we simply replace the integral in Eqs. II.3.19 and II.3.20 with a sum over allowed particle states:

$$\tilde{K}_\Delta (z, t) \propto \sum_n \frac{\varphi_{n,\Delta} (z)}{m_n^2 - t} \tag{II.3.27a}$$

$$\tilde{G}_\Delta (z, z', t) \propto \sum_n \frac{\varphi_{n,\Delta} (z) \varphi_{n,\Delta} (z')}{m_n^2 - t}, \tag{II.3.27b}$$

where

$$\varphi_{n,\Delta} \propto J_{\Delta-2} J_2 (m_n) \tag{II.3.28}$$

is the normalized wavefunction for the n-th excited state of conformal dimension Δ and m_n is this state's mass. These are the propagators that will be used in Section 4.

II.3.3 Calculating QCD Cross Sections From AdS/CFT

Here we will outline the argument of [64]; in this article, Polchinski and Strassler showed that the AdS/CFT correspondence can be exploited to allow the computation of gauge theoretic quantities through string theoretic calculations. We are interested in the $2 \rightarrow m$ exclusive scattering cross section of scalar glueballs in four dimensions; the AdS/CFT dictionary maps this scattering to the scattering of dilatons. We will work in the hard wall model, with geometry given by II.3.21, with

$$r_{min} \sim \Lambda R^2. \tag{II.3.29}$$

63

Here, Λ corresponds to the mass of the glueballs being scattered. We will further take the fixed-angle scattering limit, in which

$$s \to \infty, \ t \to \infty \text{ with } \frac{t}{s} \text{ fixed.} \tag{II.3.30}$$

The dilaton wavefunction can be written as

$$\Phi = e^{ipx}\psi(r, W), \tag{II.3.31}$$

where the W parameterize the transverse compact space. This wavefunction has two sources of r dependence: the four-momentum p in the exponent has a holographic r dependence, and the radial wavefunction ψ has an r dependence with a scale set by R. In the regime where the AdS/CFT holds good, i.e. large gN, approximate the scattering as occurring at a fixed four-dimensional coordinate x^μ. Then the full scattering amplitude $\mathcal{T}(p)$ can be expressed as an integral over dimensions transverse to the four-dimensional physics:

$$\mathcal{T} = \int dr \ d^5W \sqrt{-g}\mathcal{A}_{string}(\tilde{p}) \prod_{i=1}^{4} \psi_i(r, W). \tag{II.3.32}$$

Importantly, the amplitude $\mathcal{A}_{string}(\tilde{p})$ is a function of the holographic momentum $\tilde{p}$. The amplitude $\mathcal{A}(p)$ has an exponential dependence on its argument, so, since

$$\tilde{p} = \frac{R}{r}p, \tag{II.3.33}$$

at small r this amplitude exponentially suppresses the integrand. Similarly, at large r the dilaton wavefunctions suppress the integrand, so we can approximate the integrand as being sharply peaked at

$$r_{scatt} \sim R\sqrt{\alpha'}p \sim p\sqrt{\alpha'}r_{min}. \tag{II.3.34}$$

For large r, the radial wavefunction ψ factorizes as

$$\psi(r, W) = Cf\left(\frac{r}{r_{min}}\right)g(W)., \tag{II.3.35}$$

where

$$f \sim \left(\frac{r}{r_{min}}\right)^{-\Delta}. \tag{II.3.36}$$

with Δ being the conformal dimension of the state Φ. The radial wavefunctions obey a normalization condition

$$C^2R^4 \int dr \left\{ r\left[f\left(\frac{r}{r_{min}}\right)\right]^2 \right\} = 1. \tag{II.3.37}$$

The conformal dimension $\Delta > 0$ so this integrand is dominated by $r \sim r_{min}$, and hence we have

$$C \sim \frac{1}{R^2r_{min}}. \tag{II.3.38}$$

Finally, dimensional considerations indicate that, for $2 \rightarrow m$ scattering of 10-dimensional strings, the amplitude has the form

$$\mathcal{A}_{string}\left(\tilde{p}\right) = g_s^m \alpha'^{2m-1} F\left(\tilde{p}\sqrt{\alpha'}\right),$$ (II.3.39)

where F is a dimensionless factor. Inserting Eqs. II.3.35, II.3.38, and II.3.39 into Eq. II.3.32, we find

$$\mathcal{T}(p) \sim \frac{g_s^m \alpha'^{2m-1}}{R^{2m+2}r_{min}^{m+2}} \int dr \; r^3 \left(\frac{r_{min}}{r}\right)^\Delta F\left(\tilde{p}\sqrt{\alpha'}\right).$$ (II.3.40)

This is sharply peaked around $r \sim r_{scat}$, so we can effect the integration to find

$$\mathcal{T}(p) \sim \frac{(g_s N)^{1/4(\Delta-2)}}{N^m \Lambda^{m-2}} \left(\frac{\Lambda}{p}\right)^{\Delta-4}.$$ (II.3.41)

In this calculation, we have used Eq. II.3.29 and the discussion of II.3.1.3 to relate r_{min}, r_{scatt}, and R to gauge theory quantities such as the lightest glueball mass Λ and number of colors N.

This is the central result of [64]. The QCD prediction of this quantity is

$$\mathcal{T}(p) \sim \frac{(g_s N)^{1/2(n-2)}}{N^m \Lambda^{m-2}} \left(\frac{\Lambda}{p}\right)^{n-4}.$$ (II.3.42)

Here, n is the total number of partons in the QCD particles involved in the scattering, and plays the role of Δ in the string theory. We see the same Λ-, N-, and p-dependence in both theories, with the 't Hooft coupling $\lambda = gN$ being replaced with its square root. This tremendous success is a direct result of the holographic kinematics of the string theoretic calculation, which allowed us to perform the r-integration in a region where the exponential dependence of $\mathcal{A}_{string}\left(\tilde{p}\right)$ is unimportant. We will see the same process happen in Section 4, and it will there prove to have the same effect it has here.

II.4 Computing the Inclusive Single-Particle Production Cross Section Through Curved Space String Theory

Inspired by the results of Polchinski and Strassler, we will now use the AdS/CFT correspondence to compute the QCD cross section we are interested in. We will study, as we did in Section II.2.3.2, the scattering of six strings of the form $ab\bar{c} \rightarrow \bar{a}\bar{b}c$, but this time we will take the background spacetime to be ten-dimensional AdS space in the hard wall model, with the metric given in Eq. II.3.24. A Witten diagram for this scattering is shown in Figure II.4.1.

The external lines are scalar glueballs with conformal dimension $\Delta = 4$, and the internal lines are pomerons that line on the Regge trajectory

$$\alpha(t) = \alpha_0 + \frac{\alpha'}{4}t,$$ (II.4.1)

where in curved space

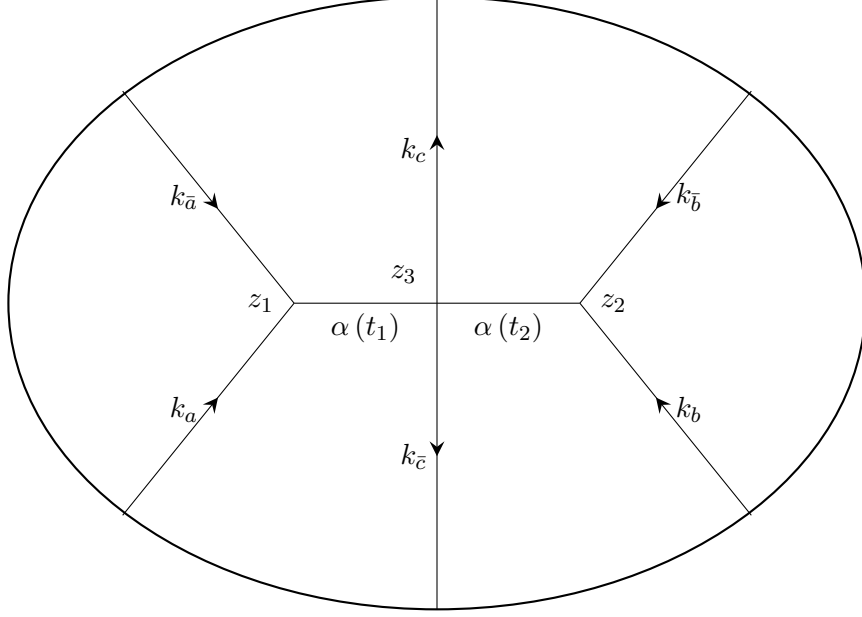$$\alpha_0 \sim 2 - \frac{2}{\sqrt{\lambda}}.$$ (II.4.2)

Figure II.4.1: Witten diagram for $3 \rightarrow 3$ scattering in curved space.

From this Witten diagram we can read off that the full six-point amplitude in curved space is

$$
T_6\left(\kappa, s_1, s_2, t_1, t_2\right) = \frac{g_0^2}{R^4} \int_0^{z_{max}} dz_1 \sqrt{-g\left(z_1\right)} \int_0^{z_{max}} dz_2 \sqrt{-g\left(z_2\right)} \int_0^{z_{max}} dz_3 \sqrt{-g\left(z_3\right)}
$$
$$
\times e^{-2A(z_1)} \varphi_a\left(z_1\right) \varphi_{\bar{a}}\left(z_1\right) K_G\left(\tilde{s}_1, \tilde{t}_1, z_1, z_3\right) z_3^2 \varphi_c\left(z_3\right) V_6\left(\tilde{\kappa}, \tilde{t}_1, \tilde{t}_2, z_3\right)
$$
$$
\times z_3^2 \varphi_{\bar{c}}\left(z_3\right) K_G\left(\tilde{s}_2, \tilde{t}_2, z_2, z_3\right) e^{-2A(z_2)} \varphi_b\left(z_2\right) \varphi_{\bar{b}}\left(z_2\right). \tag{II.4.3}
$$

This has the same form as the flat-space six point amplitude given in Eq. II.2.87; in this amplitude, the φ_i are the wavefunctions of the i-th glueball, and V_6 is the vertex operator defined in Eq. II.2.88. However, we must modify this vertex somewhat; whereas since the AdS/CFT dictionary dictates that glueballs are mapped to dilatons we are here considering the scattering of closed strings, the vertex described in Eq. II.2.88 is for open string scattering. For simplicity, we will assume the vertex has the same form, but will make the substitution $\alpha' \rightarrow \frac{1}{2}\alpha'$ given in Eq. II.2.83. Importantly, we have introduced the Reggeized graviton propagators K_G, described in [65, 67, 68]. We will not discuss this propagator in detail, but will, for reasons that will become clear, note that each of these propagator has a discontinuity in the subenergy s_i given by

$$
\text{Disc}_{s_i} K_G\left(s_i, t_i, z_i, z_3\right) \propto s_i^{\alpha_0}. \tag{II.4.4}
$$

It is essential that all Mandelstam invariants in this amplitude are holographic quantities, related to the flat space invariants in Eq. II.2.84 by the prescription in Eq. II.3.26. For instance, $\tilde{s}_1$ is given by

$$
\tilde{s}_1 = \left(\tilde{k}_a + \tilde{k}_{\bar{c}}\right)^2 = \left(\frac{z_1}{R}k_a + \frac{z_3}{R}k_{\bar{c}}\right)^2 = \frac{z_1^2}{R^2}k_a^2 + \frac{z_1 z_3}{R^2}k_a k_{\bar{c}} + \frac{z_3^2}{R^2} \sim \frac{z_1 z_3}{R^2}k_a k_{\bar{c}} \sim \frac{z_1 z_3}{R^2}s_1, \tag{II.4.5}
$$

where the k_a^2 and k_c^2 terms are neglected as they are masses, taken to be small relative to the large center of mass energy. The most important holographic Mandelstam invariants are

$$\tilde{s} = \left(\tilde{k}_a + \tilde{k}_b\right)^2 \sim \frac{z_1 z_2}{R^2} s \tag{II.4.6a}$$

$$\tilde{s}_1 = (k_a + k_{\bar{c}})^2 \sim \frac{z_1 z_3}{R^2} s_1 \tag{II.4.6b}$$

$$\tilde{s}_2 = (k_b + k_{\bar{c}})^2 \sim \frac{z_2 z_3}{R^2} s_2 \tag{II.4.6c}$$

$$\tilde{\kappa} = \frac{\tilde{s}_1 \tilde{s}_2}{\tilde{s}} \sim \frac{z_3^2}{R^2} \kappa. \tag{II.4.6d}$$

In particular, the vertex operator V_6, taken to be the same in form as in flat space, is now a function of $\tilde{\kappa} \equiv \frac{z_3^2}{R^2} \kappa$. We must now compute the complete discontinuity in this amplitude across the missing mass M^2. This comes from two sources: The vertex operator V_6 has a discontinuity across a $\kappa=0$ branch cut, and the two Reggeized graviton propagators K_G both contain discontinuities in the partial energies s_i. Recalling the definition $\kappa = \frac{s_1 s_2}{s}$, we argue that these discontinuities from the Reggeized gravitons contribute to the overall κ dependence of the discontinuity. Then

$$\begin{aligned}
\text{Disc}_{M^2} T_6 = \frac{g_0^2}{R^4} \int_0^{z_{max}} dz_1 \sqrt{-g(z_1)} \int_0^{z_{max}} dz_2 \sqrt{-g(z_2)} \int_0^{z_{max}} dz_3 \sqrt{-g(z_3)} \\
\times e^{-2A(z_1)} \varphi_a(z_1)\, \varphi_{\bar{a}}(z_1)\, \text{Disc}\left[K_G\left(\tilde{s}_1, \tilde{t}_1, z_1, z_3\right)\right] z_3^2 \varphi_c(z_3) \\
\times \text{Disc}\left[V_6\left(\tilde{\kappa}, \tilde{t}_1, \tilde{t}_2, z_3\right)\right] z_3^2 \varphi_{\bar{c}}(z_3)\, \text{Disc}\left[K_G\left(\tilde{s}_2, \tilde{t}_2, z_2, z_3\right)\right] e^{-2A(z_2)} \varphi_b(z_2)\, \varphi_{\bar{b}}(z_2).
\end{aligned} \tag{II.4.7}$$

These continuities are given in Eqs. II.2.108 and II.4.4. Because the exponent of κ in Eq. II.2.108 is highly model dependent, we will consider here only the exponential term of this equation; this will not affect the character of our final result. We will also remember to substitute $\alpha' \to \frac{1}{2}\alpha'$ in the discontinuity in V_6. Inserting those discontinuities into Eq. II.4.7, we have

$$\begin{aligned}
\text{Disc}_{M^2} T_6 = \frac{g_0^2}{R^4} \int_0^{z_{max}} dz_1 \sqrt{-g(z_1)} \int_0^{z_{max}} dz_2 \sqrt{-g(z_2)} \int_0^{z_{max}} dz_3 \sqrt{-g(z_3)} \\
\times e^{-2A(z_1)} \varphi_a(z_1)\, \varphi_{\bar{a}}(z_1)\, \tilde{s}_1^{\alpha_0} z_3^2 \varphi_c(z_3)\, e^{-2\alpha'\tilde{\kappa}} z_3^2 \varphi_{\bar{c}}(z_3)\, \tilde{s}_2^{\alpha_0} e^{-2A(z_2)} \varphi_b(z_2)\, \varphi_{\bar{b}}(z_2).
\end{aligned} \tag{II.4.8}$$

Crucially, the discontinuity in V_6 induces an exponential cutoff in $\tilde{\kappa}$, which itself exponentially suppresses the z_3 integrand:

$$e^{-2\alpha'\tilde{\kappa}} = e^{-2\alpha'\kappa z^2/R^2}. \tag{II.4.9}$$

Thus, for large values of z_3 the contribution is small, and there exists some scattering length $z_s < z_{max}$ past which the z_3 integral becomes negligible; hence, we are free to integrate only over z_3 in the domain $[0, z_s]$. From Eq. II.4.9, we read off that

$$z_s \sim \frac{R}{\sqrt{2\alpha'\kappa}}. \tag{II.4.10}$$

67

Because we work in a limit where $\kappa \to \infty$, all z in this interval are small, and we can approximate $e^{-2\alpha' \tilde{\kappa}} \sim 1$ and neglect the exponential term in the integral. Now, writing

$$\tilde{s}_1^{\alpha_0} \tilde{s}_2^{\alpha_0} = \left(s_1 \frac{z_1}{R} \frac{z_3}{R}\right)^{\alpha_0} \left(s_2 \frac{z_2}{R} \frac{z_3}{R}\right)^{\alpha_0} = (s_1 s_2)^{\alpha_0} \frac{z_1^{\alpha_0}}{R^{\alpha_0}} \frac{z_2^{\alpha_0}}{R^{\alpha_0}} \frac{z_3^{2\alpha_0}}{R^{2\alpha_0}} = s^{\alpha_0} \kappa^{\alpha_0} \frac{z_1^{\alpha_0}}{R^{\alpha_0}} \frac{z_2^{\alpha_0}}{R^{\alpha_0}} \frac{z_3^{2\alpha_0}}{R^{2\alpha_0}}, \quad \text{(II.4.11)}$$

we have

$$\text{Disc}_{M^2} T_6 = \frac{g_0^2 s^{\alpha_0} \kappa^{\alpha_0}}{R^{4+4\alpha_0}} \int_0^{z_{max}} dz_1 \sqrt{-g(z_1)} \int_0^{z_{max}} dz_2 \sqrt{-g(z_2)} \int_0^{z_s} dz_3 \sqrt{-g(z_3)}$$

$$\times e^{-2A(z_1)} \varphi_a(z_1) \varphi_{\bar{a}}(z_1) z_3^2 \varphi_c(z_3) z_3^2 \varphi_{\bar{c}}(z_3) e^{-2A(z_2)} \varphi_b(z_2) \varphi_{\bar{b}}(z_2) \left[z_1^{\alpha_0} z_2^{\alpha_0} z_3^{2\alpha_0}\right].$$

$$\text{(II.4.12)}$$

In what remains, the z_3 terms are completely independent of the z_1 and z_2 terms, and moreover all residual κ dependence stems from the κ dependence of z_s. Thus the z_1 and z_2 integrals contribute only an overall numerical prefactor, which we write as β. Then

$$\text{Disc}_{M^2} T_6 = \frac{g_0^2 s^{\alpha_0} \kappa^{\alpha_0} \beta}{R^{4+4\alpha_0}} \int_0^{z_s} dz_3 \sqrt{-g(z_3)}\, z_3^{4+2\alpha_0} \varphi_c(z_3) \varphi_{\bar{c}}(z_3). \quad \text{(II.4.13)}$$

We will now analyze the components of this integrand to extract the final κ dependence of the discontinuity, and hence of the inclusive cross section. From the hard wall metric

$$ds^2 = \frac{R^2}{z^2} \left(\eta_{\mu\nu} dx^\mu dx^\nu + dz^2\right) + ds_{S^5}^2, \quad \text{(II.4.14)}$$

we can read off

$$-\det(g) = \frac{R^{10}}{z^{10}}, \quad \text{(II.4.15)}$$

where we have neglected the dependence of the metric on the transverse compact space, and hence

$$\sqrt{-g} = \frac{R^5}{z^5}. \quad \text{(II.4.16)}$$

Now, the open-string wavefunctions near $z = 0$ are

$$\varphi(z) = \frac{z^2}{R^2} J_{\Delta-2}(m_0 z), \quad \text{(II.4.17)}$$

where Δ is the conformal dimension of the operator producing the particle and m_0 is an energy constant corresponding to the string mass. To leading order in small z, then,

$$\varphi(z) \approx R^{-2} z^\Delta. \quad \text{(II.4.18)}$$

Inserting these results into Eq. II.4.13, we find that

$$\text{Disc}_{M^2} T_6 = \frac{g_0^2 s^{\alpha_0} \kappa^{\alpha_0} \beta}{R^{3+4\alpha_0}} \int_0^{z_s} dz_3 z_3^{-5} z_3^{4+2\alpha_0} z_3^{\Delta_c} z_3^{\Delta_{\bar{c}}} \tag{II.4.19}$$

$$= \frac{g_0^2 s^{\alpha_0} \kappa^{\alpha_0} \beta}{R^{3+4\alpha_0}} \int_0^{z_s} \frac{dz_3}{z_3} z_3^{\Delta_c + \Delta_{\bar{c}} + 2\alpha_0}$$

$$= \frac{g_0^2 s^{\alpha_0} \kappa^{\alpha_0} \beta}{R^{3+4\alpha_0} (\Delta_c + \Delta_{\bar{c}} + 2\alpha_0)} z_3^{\Delta_c + \Delta_{\bar{c}} + 2\alpha_0} \Big|_0^{z_s}$$

$$= \frac{g_0^2 s^{\alpha_0} \kappa^{\alpha_0} \beta}{R^{3+4\alpha_0} (\Delta_c + \Delta_{\bar{c}} + 2\alpha_0)} z_s^{\Delta_c + \Delta_{\bar{c}} + 2\alpha_0}. \tag{II.4.20}$$

Finally, we insert Eq. II.4.10 into this result to find that

$$\text{Disc}_{M^2} T_6 = \frac{g_0^2 s^{\alpha_0} \kappa^{\alpha_0} \beta}{R^{3+4\alpha_0} (\Delta_c + \Delta_{\bar{c}} + 2\alpha_0)} \left(\frac{R}{\sqrt{2\alpha' \kappa}} \right)^{\Delta_c + \Delta_{\bar{c}} + 2\alpha_0}$$

$$= \frac{R^{\Delta_c + \Delta_{\bar{c}} - 2\alpha_0 - 3} g_0^2 \beta}{(2\alpha')^{(\Delta_c + \Delta_{\bar{c}} + 2\alpha_0)/2} (\Delta_c + \Delta_{\bar{c}} + 2\alpha_0)} s^{\alpha_0} \kappa^{-(\Delta_c + \Delta_{\bar{c}})/2}. \tag{II.4.21}$$

With this result, we directly calculate the inclusive cross section

$$\frac{d^3 \sigma_{ab \to cX}}{d\mathbf{p}_c^3} = \frac{1}{s} \text{Disc}_{M^2} T_6 = \frac{R^{\Delta_c + \Delta_{\bar{c}} - 2\alpha_0 - 3} g_0^2 \beta}{(2\alpha')^{(\Delta_c + \Delta_{\bar{c}} + 2\alpha_0)/2} (\Delta_c + \Delta_{\bar{c}} + 2\alpha_0)} s^{\alpha_0 - 1} \kappa^{-(\Delta_c + \Delta_{\bar{c}})/2}. \tag{II.4.22}$$

For the calculation we have performed, the external particles c and $\bar{c}$ are scalar glueballs, so $\Delta_c = \Delta_{\bar{c}} = 4$ [83]. Then our cross section is given essentially by

$$\frac{d^3 \sigma_{ab \to cX}}{d\mathbf{p}_c^3} \sim s^{\alpha_0 - 1} \kappa^{-4}. \tag{II.4.23}$$

This is our final desired result. Its simplicity is striking, as is its origin. That curved space string-theory predicts this exponential cutoff in κ is a direct consequence of the holographic momenta. Because all kinematic quantities in the AdS calculation gain a dependence in the AdS coordinate z, we are allowed to integrate only over a region in which the exponential dependence is unimportant, and this allows us to extract a power-law dependence. This is exactly the sort of physics seen in [64], and is a spectacular demonstration of the power of AdS/CFT.

We will now examine the physical consequences of Eq. II.4.23, which should be thought of as a distribution of the cross section in the momentum $\mathbf{p}_c$ of the produced particle. Then the s-dependence determines the height of the distribution, i.e. the total cross section, since s is independent of $\mathbf{p}_c$. As we saw in Eq. II.2.86, at high energies $\kappa \sim p_T^2$. Thus the power law behavior in κ translates immediately to a power law behavior in the transverse momentum of the produced particle:

$$\frac{d^3 \sigma_{ab \to cX}}{d\mathbf{p}_c^3} \sim s^{\alpha_0 - 1} p_T^{-8}. \tag{II.4.24}$$
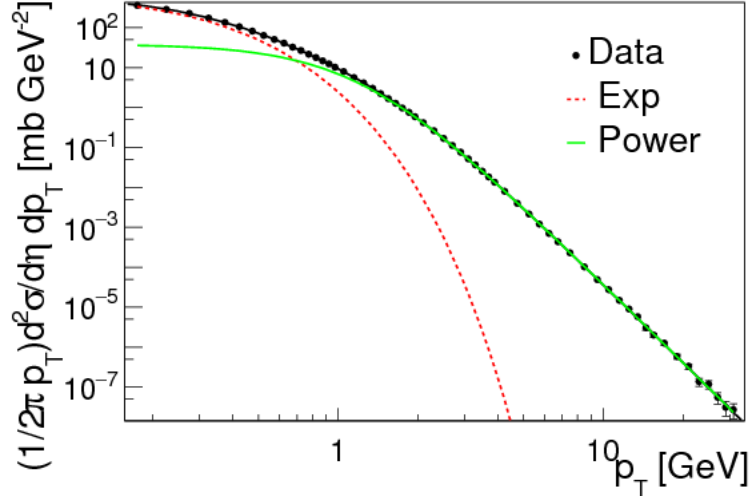
Figure II.4.2: A fit of the distribution in Eq. II.4.25 to particle collider data. Extremely good agreement between theory and experiment is seen in all kinematic regimes. Figure originally appeared in [57].

This distribution can be directly compared to experiment. In particular, [57] fits the inclusive charged particle cross section found in particle collider data to a distribution of the form

$$\frac{d^2\sigma}{d\eta d^2 p_{\mathrm{T}}} = A_1 \exp\left(-\frac{K}{T_1}\right) + A_2 \left(1 + \frac{p_{\mathrm{T}}^2}{T_2^2 N}\right)^N, \tag{II.4.25}$$

where η is the pseudorapidity of the produced particle, K is its (relativistic) kinetic energy, and A_1, A_2, T_1, T_2, N are fit parameters. This distribution, suggested in [85], is the sum of a Boltzmann-like exponential distribution and a power-law distribution; each of these is expected to dominate in a certain kinematic regime. The fit to data is shown in Figure II.4.2, originally found in [57].

The agreement between the fitted function and the experimental data is striking; in all kinematic regimes, the fitted distribution is seen to match the data excellently. In particular, in the high p_{T} regime, the fit is entirely dominated by the power-law distribution, as the exponential contribution becomes exponentially small. This qualitatively matches the curved space prediction in Eq. II.4.23, and reinforces our faith in the ability of the hard wall model to give accurate predictions for QCD processes.

II.5 Conclusion

Through use of the AdS/QCD correspondence, we have employed curved-space string theory to calculate the inclusive single-particle production cross section in QCD. We find good agreement with the experimental observation of a power-law decay, in contrast to the exponential cutoff predicted by flat space string theory. Although the AdS/CFT correspondence has never been proven theoretically, results such as this one add to the already enormous pile of circumstantial evidence supporting this duality that has accumulated in the literature, and adds to our confidence in this seminally important idea.

Outlook: Beam Experiments and QCD

Here I have presented the two research projects that I have worked on at Brown. Naively, it looks like these are completely disparate; the LHC doesn't operate at infinite energy, or interact with more than three colors of gluons, much less an infinite number of them! However, at second glance, and with an eye towards the future of collider physics, it seems like these two topics might not be as unrelated as they seem.

The LHC is, of course, a proton collider. At the high energies it operates at, however, what that label translates to is a gluon collider; the three quarks inside the proton are much less important than the high-energy virtual gluons inside the proton. This is why, for instance, the dominant method of Higgs production at the LHC is gluon fusion (mediated, as it happens, by virtual tops; the top-Higgs coupling is proportional to the top mass, so this represents yet another important application of top mass physics!).

However, to understand the dynamics of gluon-gluon interactions requires the full, massively nonlinear dynamics of QCD. Computationally, making any sense of this theory is almost impossible. No exact solutions are known, and it seems like wishful thinking to ever expect one to appear. The only way to attack the gluon field equations is perturbation theory; for a myriad of theoretical reasons, however, the standard procedure, familiar from any graduate course in quantum field theory, does not really apply to QCD. Feynman was, after all, working with QED firmly in mind when he wrote down his famous rules for coupling-constant perturbation theory, and the coupling constants of QED and QCD inhabit completely different regimes. It has been suggested that a new toolbox, beyond the familiar processes of MC simulation, might be needed to fully exploit the potential of the LHC and its eventual successor.

While the somewhat simple hard wall analysis discussed here of course is insufficient to completely describe LHC physics, it is a clear step in the right direction. Cross sections are the observables most directly applicable to experimental particle physics as it exists today, and baring a dramatic shift away from collider experiments are posed to remain so in the future. It is now clear that AdS/CFT methods can make predictions for QCD cross sections at experimentally relevant energies. Even beyond cross sections, AdS/CFT can be much more useful than perturbative methods; it has been, and remains, the best theoretical technique to describe the firmly nonperturbative quark-gluon plasma phase of QCD studied at RHIC and ALICE.

Although I cannot predict the theoretical tools necessary for the next generation of experiments, or even what those experiments will be, it seems that AdS/CFT can provide a profoundly useful tool to perform the sorts of calculations necessary to understand their results. From perturbative cross sections to nonperturbative physics, many questions remain in the study of nonabelian gauge theory, many of which are at least in principle accesible to AdS/CFT methods theoretically, and experimentally to the supercolliders of the future.

References

[1] The ATLAS, CMS, CDF, and D0 Collaborations. First combination of Tevatron and LHC measurements of the top-quark mass. 2014, 1403.4427.

[2] J. Andrea, U. Heintz, M. Narain, Th. Speer. Measurement of the Top quark mass with fully-leptonic $t\bar{t}$ decays in pp collisions at $\sqrt{s} = 7$ TeV with the full 2011 dataset. *CMS*, AN-12-134, 2012.

[3] Serguei Chatrchyan et al. Measurement of the top-quark mass in $t\bar{t}$ events with dilepton final states in pp collisions at $\sqrt{s} = 7$ TeV. *Eur.Phys.J.*, C72:2202, 2012, 1209.2393.

[4] January 22 reco. *CMS TWiki page*, pages https://cms–service–dqm.web.cern.ch/cms–service–dqm/CAF/certification/Collisions12/8TeV/Reprocessing/Cert_190456–208686_8TeV_22Jan2013ReReco_Collisions12_JSON.txt.

[5] Pileup studies. *CMS TWiki page*, page https://twiki.cern.ch/twiki/bin/view/CMS/PileupInformation.

[6] Utilities for accessing pileup information for data. *CMS TWiki page*, page https://twiki.cern.ch/twiki/bin/view/CMS/PileupJSONFileforData.

[7] Johan Alwall, Michel Herquet, Fabio Maltoni, Olivier Mattelaer, and Tim Stelzer. MadGraph 5 : going beyond. *JHEP*, 06:128, 2011, 1106.0522.

[8] Pierre Artoisenet, Rikkert Frederix, Olivier Mattelaer, and Robbert Rietkerk. Automatic spin-entangled decays of heavy resonances in Monte Carlo simulations. *JHEP*, 03:015, 2013, 1212.3460.

[9] Torbjörn Sjöstrand, Stephen Mrenna, and Peter Skands. PYTHIA 6.4 physics and manual. *JHEP*, 05:026, 2006, hep-ph/0603175.

[10] Serguei Chatrchyan et al. Measurement of the underlying event activity at the LHC with $\sqrt{s} = 7$ TeV and comparison with $\sqrt{s} = 0.9$ TeV. *JHEP*, 09:109, 2011, 1107.0330.

[11] Michelangelo L. Mangano, Mauro Moretti, Fulvio Piccinini, and Michele Treccani. Matching matrix elements and shower evolution for top- quark production in hadronic collisions. *JHEP*, 01:013, 2007, hep-ph/0611129.

[12] Paolo Nason. A new method for combining NLO QCD with shower Monte Carlo algorithms. *JHEP*, 11:040, 2004, hep-ph/0409146.

[13] Stefano Frixione, Paolo Nason, and Carlo Oleari. Matching NLO QCD computations with parton shower simulations: the POWHEG method. *JHEP*, 11:070, 2007, 0709.2092.

[14] Simone Alioli, Paolo Nason, Carlo Oleari, and Emanuele Re. A general framework for implementing NLO calculations in shower Monte Carlo programs: the POWHEG BOX. *JHEP*, 06:043, 2010, 1002.2581.

[15] Michal Czakon, Paul Fiedler, and Alexander Mitov. The total top quark pair production cross-section at hadron colliders through $O(\alpha_S^4)$. *Phys. Rev. Lett.*, 110:252004, 2013, 1303.6254.

[16] Nikolaos Kidonakis. Differential and total cross sections for top pair and single top production. pages 831–834, 2012, 1205.3453.

[17] Ye Li and Frank Petriello. Combining QCD and electroweak corrections to dilepton production in FEWZ. *Phys.Rev.*, D86:094034, 2012, 1208.5967.

[18] K Nakamura and PARTICLE Data Group. Review of particle physics. *Journal of Physics G: Nuclear and PARTICLE Physics*, 37(7A):075021, 2010.

[19] CMS Collaboration. Particle flow event reconstruction in cms and performance for jets, taus, and met. *CMS Physics Analysis Summary*, CMS-PAS-PFT-09-001, 2009.

[20] Dilepton trigger results. *CMS TWiki page*, page https://twiki.cern.ch/twiki/bin/view/CMS/DileptonTriggerR

[21] CMS Collaboration. Performance of the CMS muon reconstruction in pp Collisions at $\sqrt{s} = 7$ TeV. *PAS*, MUO-10-002.

[22] Top event selection. *CMS TWiki page*, page https://twiki.cern.ch/twiki/bin/view/CMS/TWikiTopRefEventSe

[23] Muon efficiency scale factors. *CMS TWiki page*, page https://twiki.cern.ch/twiki/bin/view/CMS/MuonReferenceEffs.

[24] CMS Collaboration. Electon reconstruction and identification at $\sqrt{s} = 7$ TeV. *PAS*, EGM-10-004.

[25] https://twiki.cern.ch/twiki/bin/viewauth/CMS/EgammaEARhoCorrection.

[26] e/γ scale factor. *CMS TWiki page*, page https://twiki.cern.ch/twiki/bin/view/CMS/KoPFAElectronTagAndP

[27] Jec data/mc. *CMS TWiki page*, page https://twiki.cern.ch/twiki/bin/view/CMS/JECDataMC.

[28] Jet resolution. *CMS TWiki page*, page https://twiki.cern.ch/twiki/bin/view/CMS/JetResolution.

[29] Performance of b tagging at $\sqrt{s} = 8$ tev in multijet, $t\bar{t}$ and boosted topology events. CMS Physics Analysis Summary CMS-PAS-BTV-13-001, CERN, 2013.

[30] J. Andrea et al. Measurement of the top dilepton cross section using b-tagging at $\sqrt{s} = 7$ TeV with $2.2\,\text{fb}^{-1}$ in pp collisions. *CMS*, AN-11-477, 2012.

[31] Serguei Chatrchyan et al. Measurement of the t t-bar production cross section and the top quark mass in the dilepton channel in pp collisions at sqrt(s) =7 TeV. *JHEP*, 1107:049, 2011, 1105.5661.

[32] B. Abbott et al. Measurement of the top quark mass using dilepton events. *Phys. Rev. Lett.*, 80:2063–2068, 1998, hep-ex/9706014.

[33] J. Andrea, A. Avetisyan, U. Heintz, M. Narain and Th. Speer. Measurement of the Top quark mass with fully-leptonic $t\bar{t}$ decays in pp collisions at $\sqrt{s} = 7$ TeV. *CMS*, AN-10-259.

[34] Lars Sonnenschein. Analytical solution of $t\bar{t}$ dilepton equations. *Phys. Rev. D*, 73(5):054015, Mar 2006.

[35] Lars Sonnenschein. Erratum: Analytical solution of $t\bar{t}$ dilepton equations [phys. rev. d 73, 054015 (2006)]. *Phys. Rev. D*, 78(7):079902, Oct 2008.

[36] Lars Sonnenschein. Algebraic approach to solve $t\bar{t}$ dilepton equations. *Phys. Rev. D*, 72(9):095020, Nov 2005.

[37] R. H. Dalitz and Gary R. Goldstein. Decay and polarization properties of the top quark. *Phys. Rev. D*, 45(5):1531–1543, Mar 1992.

[38] R. Ciesielski, H. Held, P. Schieferdecker, and M. Zielinski. Jet energy resolutions derived from qcd simulation for the analysis of first $\sqrt{s} = 7$ tev collision data. *CMS*, AN-10-121.

[39] http://cds.cern.ch/record/1692900/files/Thesis-2012-Avetisyan.pdf?version=1.

[40] https://twiki.cern.ch/twiki/bin/viewauth/CMS/TopMassSystematics.

[41] A. Heister et al. Study of the fragmentation of b quarks into B mesons at the Z peak. *Phys.Lett.*, B512:30–48, 2001, hep-ex/0106051.

[42] J. Abdallah et al. A study of the b-quark fragmentation function with the DELPHI detector at LEP I and an averaged distribution obtained at the Z Pole. *Eur.Phys.J.*, C71:1557, 2011, 1102.4748.

[43] Serguei Chatrchyan et al. Determination of Jet Energy Calibration and Transverse Momentum Resolution in CMS. *JINST*, 6:P11002, 2011, 1107.4277.

[44] Serguei Chatrchyan et al. Energy Calibration and Resolution of the CMS Electromagnetic Calorimeter in pp Collisions at $\sqrt{s} = 7$ TeV. *JINST*, 8:P09009, 2013, 1306.2016.

[45] Serguei Chatrchyan et al. Performance of CMS muon reconstruction in pp collision events at $\sqrt{s} = 7$ TeV. *JINST*, 7:P10002, 2012, 1206.4071.

[46] Standard Model Cross Sections for CMS at 8 TeV. *CMS TWiki Page*, https://twiki.cern.ch/twiki/bin/viewauth/CMS/StandardModelCrossSectionsat8TeV.

[47] Top $p_{\rm t}$ reweighting. *CMS TWiki page*, page https://twiki.cern.ch/twiki/bin/view/CMS/TopPtReweighting.

[48] Peter Zeiler Skands. Tuning Monte Carlo Generators: The Perugia Tunes. *Phys. Rev. D*, 82:074018, 2010, 1005.3457.

[49] P. Biallass et al. Parton distribution uncertainty determination within cmssw. *CMS AN*, 2009/048, 2009.

[50] First combination of Tevatron and LHC measurements of the top-quark mass. 2014, 1403.4427.

[51] Gabriele Veneziano. Construction of a crossing-simmetric, regge-behaved amplitude for linearly rising trajectories. *Il Nuovo Cimento A*, 57(1):190–197, 1968.

[52] M. A. Virasoro. Alternative constructions of crossing-symmetric amplitudes with regge behavior. *Phys. Rev.*, 177:2309–2311, Jan 1969.

[53] K. Kikkawa, B. Sakita, and M. A. Virasoro. Feynman-like diagrams compatible with duality. i. planar diagrams. *Phys. Rev.*, 184:1701–1713, Aug 1969.

[54] V.A. Matveev, R.M. Muradian, and A.N. Tavkhelidze. Automodellism in the large - angle elastic scattering and structure of hadrons. *Lett.Nuovo Cim.*, 7:719–723, 1973.

[55] Stanley J. Brodsky and Glennys R. Farrar. Scaling Laws at Large Transverse Momentum. *Phys.Rev.Lett.*, 31:1153–1156, 1973.

[56] Stanley J. Brodsky and Glennys R. Farrar. Scaling Laws for Large Momentum Transfer Processes. *Phys.Rev.*, D11:1309, 1975.

[57] Alexander Bylinkin, Nadezda S. Chernyavskaya, and Andrei A. Rostovtsev. Predictions on the transverse momentum spectra for charged pARTICLE production at LHC-energies from a two component model. 2015, 1501.05235.

[58] Juan Martin Maldacena. The Large N limit of superconformal field theories and supergravity. *Int.J.Theor.Phys.*, 38:1113–1133, 1999, hep-th/9711200.

[59] Shinsei Ryu and Tadashi Takayanagi. Holographic derivation of entanglement entropy from AdS/CFT. *Phys.Rev.Lett.*, 96:181602, 2006, hep-th/0603001.

[60] S. Sachdev. What can gauge-gravity duality teach us about condensed matter physics? August 2011, 1108.1197.

[61] Csaba Csaki, Hirosi Ooguri, Yaron Oz, and John Terning. Glueball mass spectrum from supergravity. *JHEP*, 9901:017, 1999, hep-th/9806021.

[62] Robert de Mello Koch, Antal Jevicki, Mihail Mihailescu, and Joao P. Nunes. Evaluation of glueball masses from supergravity. *Phys.Rev.*, D58:105009, 1998, hep-th/9806125.

[63] Richard C Brower, Samir D Mathur, and Chung-I Tan. Glueball spectrum for qcd from ads supergravity duality. *Nuclear Physics B*, 587(1):249–276, 2000.

[64] Joseph Polchinski and Matthew J. Strassler. Hard scattering and gauge / string duality. *Phys.Rev.Lett.*, 88:031601, 2002, hep-th/0109174.

[65] Richard C. Brower, Joseph Polchinski, Matthew J. Strassler, and Chung-I Tan. The Pomeron and gauge/string duality. *JHEP*, 0712:005, 2007, hep-th/0603115.

[66] Christopher P. Herzog, Steve Paik, Matthew J. Strassler, and Ethan G. Thompson. Holographic Double Diffractive Scattering. *JHEP*, 0808:010, 2008, 0806.0181.

[67] Richard C. Brower, Marko Djuric, and Chung-I Tan. Diffractive Higgs Production by AdS Pomeron Fusion. *JHEP*, 1209:097, 2012, 1202.4953.

[68] Richard Brower, Marko Djuric, and Chung-I Tan. Holographic Double Diffractive Production of Higgs and the AdS Graviton/Pomeron. 2012, 1204.0451.

[69] Richard C. Brower, Marko Djuric, Ina Sarcevic, and Chung-I Tan. The AdS Graviton/Pomeron Description of Deep Inelastic Scattering at Small x. 2011, 1106.5681.

[70] C. E. DeTar, Kyungsik Kang, Chung-I Tan, and J. H. Weis. Duality and single-particle production. *Phys. Rev. D*, 4:425–439, Jul 1971.

[71] AM Mueller. O (2, 1) analysis of single-particle spectra at high energy. *Physical Review D*, 2(12):2963, 1970.

[72] David Tong. String Theory. 2009, 0908.0333.

[73] J. Polchinski. *String Theory: Volume 1, An Introduction to the Bosonic String*. Cambridge Monographs on Mathematical Physics. Cambridge University Press, 1998.

[74] K. Becker, M. Becker, and J.H. Schwarz. *String Theory and M-Theory: A Modern Introduction*. Cambridge University Press, 2006.

[75] Hirosi Ooguri and Zheng Yin. TASI lectures on perturbative string theories. pages 5–81, 1996, hep-th/9612254.

[76] B. Zwiebach. *A First Course in String Theory*. Cambridge University Press, 2009.

[77] M. Ammon and J. Erdmenger. *Gauge/Gravity Duality*. Cambridge University Press, 2015.

[78] T.W. Gamelin. *Complex Analysis*. Undergraduate Texts in Mathematics. Springer, 2001.

[79] Michael E Peskin and Daniel V Schroeder. *An introduction to quantum field theory*. Westview, 1995.

[80] L Clavelli. Particle production in the double dual pomeron region. *Nuclear Physics B*, 154(1):47–61, 1979.

[81] K Bardakci and Henri Ruegg. Reggeized resonance model for the production amplitude. *Physics Letters B*, 28(5):342–347, 1968.

[82] Richard C. Brower, Horatiu Nastase, Howard J. Schnitzer, and Chung-I Tan. Analyticity for Multi-Regge Limits of the Bern-Dixon-Smirnov Amplitudes. *Nucl.Phys.*, B822:301–347, 2009, 0809.1632.

[83] S.S. Gubser, Igor R. Klebanov, and Alexander M. Polyakov. Gauge theory correlators from noncritical string theory. *Phys.Lett.*, B428:105–114, 1998, hep-th/9802109.

[84] Eric D'Hoker and Daniel Z. Freedman. Supersymmetric gauge theories and the AdS / CFT correspondence. pages 3–158, 2002, hep-th/0201253.

[85] A.A. Bylinkin and A.A. Rostovtsev. Parametrization of the shape of hadron-production spectra in high-energy pARTICLE interactions. *Phys.Atom.Nucl.*, 75:999–1005, 2012.

Acknowledgements